A PIECEWISE COMPUTATIONAL SCHEME FOR THE VIBRO-ACOUSTIC MODELING IN MID-TO-HIGH FREQUENCY RANGE

ZHONGYU HU

PhD

The Hong Kong Polytechnic University

2019

The Hong Kong Polytechnic University

Department of Mechanical Engineering

A Piecewise Computational Scheme for the Vibro-acoustic Modeling in Mid-to-high Frequency Range

Zhongyu HU

A thesis submitted in partial fulfilment of the requirements for the degree of Doctor of Philosophy

February 2019

CERTIFICATE OF ORIGINALITY

I hereby declare that this thesis is my own work and that, to the best of my knowledge and belief, it reproduces no material previously published or written, nor material that has been accepted for the award of any other degree or diploma, except where due acknowledgment has been made in the text.

_____ (Signed)

ZHONGYU HU
February, 2019

Abstract

This thesis presents a computational method for the mid-to-high frequency vibro-acoustic system modeling. The Vibro-acoustic analysis in the mid-to-high frequency range is technically challenging due to the complex wavelength composition and the large numbers of the degrees of freedom involved. Conventional low-frequency methods like Finite Element Method (FEM) require enormous computational time and calculation capability while high-frequency methods like Statistical Energy Analysis (SEA) are not always suitable, because of the difficulty in meeting the basic assumptions in some long wavelength sub-systems, or the little information provided. Therefore, this thesis is aiming at establishing a simulation methodology that can balance the efficiency and the richness of the information obtained. The structure of the thesis is as follows.

Preliminary investigations are first conducted on the modeling of a typical plate-cavity system, which is widely used as a simplified benchmark model for the sound insulation problems in building/structural acoustics. Through the exploration of the modal method and the wave method, the well-recognized existing convergence difficulties of the former at the vicinity of the vibro-acoustic interface are investigated. A criterion to accelerate the convergence speed of the modal method close to the cavity-plate interface is proposed. By improving the reliability of the modal method, this part paves the way forward by providing a reference solution to the mid-to-high frequency modeling analysis.

Then, a so-called Condensed Transfer Function (CTF) method is proposed, in which the uncoupled sub-systems are modeled individually by decomposing the force and velocity over the interface into a set of functions, namely the Condensation Functions (CFs). Then the subsets obtained from each sub-system are assembled

following the velocity continuity and force equilibrium conditions. The focus is fixed on how to increase the calculation efficiency of the CTF method by properly selecting the Condensation Functions (CFs). Owing to the spatial wavy features, the complex exponential functions are expected to better match the structural wavelength variations in a given frequency band. It is shown that the complex exponential functions outperform the previously developed Patch Transfer Function (PTF) methods using gate functions. Numerical analyses reveal a piecewise convergence behavior of the calculation in different frequency bands. This property is further exploited in a plate-cavity system for establishing a criterion for further truncation of the CFs, referred to as the piecewise scheme.

The piecewise scheme is then extended to systems with an increasing coupling strength. To this end, a coupling strength factor (CSP) is defined to quantify the coupling strength between two sub-systems. Parameters that determine the coupling strength between the sub-systems are then discussed. Using the defined CSP, the previously established piecewise scheme is re-examined and validated using an acoustic system comprising two mutually connected sub-cavities. The effect of the coupling strength on the computational error of the piecewise scheme is systematically quantified. The piecewise scheme, alongside the CTF approach itself, is then experimentally validated.

Finally, the piecewise scheme is applied to a simplified Double Skin Façade system (DSF). It is shown that the proposed modeling methodology allows a fine and detailed description of this complex vibro-acoustic system with a relatively complex and large dimension in the entire frequency range including the mid-to-high one.

Publications

Journal Papers:

1. Z. Y. Hu, L. Maxit, and L. Cheng, "Convergence criteria on the acoustic velocity continuity in a panel-cavity system". *The Journal of the Acoustical Society of America*. 2017 Mar 27; 141(3):2137-42.

2. Z. Y. Hu, C. Yang, and L. Cheng, "Acoustic resonator tuning strategies for the narrowband noise control in an enclosure". *Applied Acoustics*. 2018 May 1; 134:88-96

3. Z. Y. Hu, L. Maxit, and L. Cheng, "Piecewise convergence behavior of the condensed transfer function approach for mid-to-high frequency modeling of a panel-cavity system". *Journal of Sound and Vibration*. 2018 Nov 24; 435:119-34.

Conference Papers:

1. Z. Y. Hu, L. Maxit, and L. Cheng, "On the Choice of condensation functions for mid-to-high frequency vibroacoustic modeling". *ICSV 2017*.

2. Z. Y. Hu, L. Maxit, and L. Cheng, "A Criterion for Piece-wise Mid-Frequency Vibro-acoustic Modeling Using the Condensed Transfer Function Approach". *Internoise 2017*.

3. Z. Y. Hu, L. Maxit, and L. Cheng, "A Piece-wise Calculation Scheme for the Mid-to-high Frequency Vibro-acoustic Simulations". *NOVEM 2018*

4. Z. Y. Hu, L. Maxit, and L. Cheng, "A Piecewise Calculation Scheme for the Mid-to-high Frequency Strong Coupling Modeling". *ICSV 2019*.

Acknowledgements

First of all, I would like to express my deepest thanks of gratitude to my supervisor, Professor Li CHENG. For the last five years, he is not only an academic advisor but also a life mentor in many aspects, in terms of how to be an eligible researcher and be a man of integrity.

I also wish to say Merci to Dr. Laurent MAXIT, INSA de Lyon, for his patient guiding since the very fundamental part of this subject. I have learned lots of things, academical or cultural, during my three months in Lyon.

Special thanks to my parents, girlfriend Wen ZHONG, and other family members, for their unconditional support, understanding, and love for me. They are the ultimate driving of my progress.

I would like to thank all the colleges in my group and department technicians. Many works will be impossible without their help. Special thanks are given to Dr. Cheng YANG, who leads me into the acoustic area at the very beginning stage of the study.

At last, thanks to my friends who have been together since the Master period, classmates in Harbin Institute of Technology, and those of more than ten years, for your encouragement at difficult times.

Table of Contents

List of Figures

List of Tables

List of Abbreviations

FEM	Finite Element Method
SEA	Statistical Energy Analysis
WBM	Wave Based Method
PTF	Patch Transfer Function
CTF	Condensed Transfer function
CF	Condensation Function
MPP	Micro-Perforated Panel
MPPA	Micro-Perforated Absorber
DSF	Double Skin Facade
CSF	Coupling Strength Factor
MOP	Modal Overlap Factor
DoF	Degrees of Freedom
SRI	Sound Reduction Index

CHAPTER 1 Introduction

1.1 Research Background and Motivations

The modeling of vibro-acoustic systems has always been an important topic, attracting persistent attention in the acoustic community. The issue impacts on various applications involving structures and systems such as buildings and vehicles, etc. Among existing problems, mid-to-high frequency vibro-acoustic system modeling is particularly challenging due to the complex deformation wavelength composition among different sub-systems and the large number of degrees of freedom (DoF) involved, which make the modeling computational costly. Main challenges root in filling the gap left over by the low-frequency methods like modal-based methods [1] or the finite element method (FEM) [2-4] and the high-frequency statistical energy analyses (SEA) [5-7]. Assumptions and approximations adopted in these methods are well established, which define and limit their respective application ranges at the same time. In the mid-to-high frequency range, the presence of the short-wavelength components challenges the conventional deterministic modeling methods by the exorbitant computational cost incurred. The long wavelength ones, however, fail to meet the SEA assumptions, due to the insufficient modal overlap and the unavailability of the rigorous coupling loss factors [8]. The purpose of this thesis is therefore to develop a simulation tool that can balance the calculation efficiency and the quantity of information obtained for the mid-to-high frequency system modeling.

A typical example is a Double Skin Façade (DSF) system, widely adopted in modern buildings as shown in Figure 1.1. DSF is a system of building serving for

reducing the overall energy consumption. It consists of two skins arranged in such a way that the air can flow within the intermediate cavity or corridor.

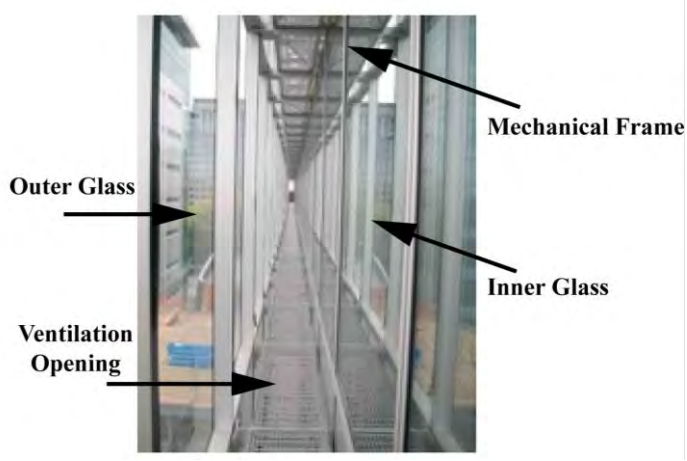

Figure 1.1 A typical DSF system.

However, one of the main problems of the DSF system is that it may introduce more outside noise into the building. Most existing evaluations on the acoustic performances of façades and windows are based on simple empirical formulas. These formulas, however, are too rough when compared with the actual experimental data and can hardly address the need for allowing parameter variations and system optimization at the design stage. On the other hand, the noise insulation performance of the DSF is highly dependent on the design parameters (materials of the skins, dimensions of the cavities, size of the apertures, possible uses of acoustic control devices, etc.). Due to the large size of the system and the need to go higher in frequencies, a proper numerical tool is needed to assess the acoustic performance of the DSF system. Accuracy, flexibility, and computational efficiency are just a few important attributes of such a tool in order to fully address the need for design and optimization. Thus, the presented modeling method will be applied to DSF modeling as an example.

1.2 Literature Review

The literature review mainly contains three parts. The first part focuses on the mid-to-high frequency method itself. The second one concerns the modeling of a plate-cavity system, which is a classical benchmark problem in vibro-acoustic analyses. The last part addresses the modeling methods in building acoustics.

1.2.1 Mid-to-high Frequency Methods

Mid-to-high frequency vibro-acoustic modeling methods have been extensively investigated during the last few decades. To define the boundary lines of the so-called mid-frequency range, it is widely accepted that it starts when the wavelength difference between sub-systems is large [9, 10]. Based on that, various methods were developed. Although these methods vary in terms of application backgrounds and detailed modeling theory, they can be divided into three different categories based on the basic idea adopted. The first one is to extend the effective working frequency range of the traditional low-frequency methods to mid-frequency range, noted as “enhanced deterministic methods”. The second one is to revamp the SEA method by introducing new assumptions and improvements so as to warrant its applicability in a relatively lower frequency range, noted as “enhanced statistical methods”. The last one was developed based on the sub-structure theory. These methods partition the whole system into several sub-systems and use proper methods for each sub-system based on their dynamic properties, noted as “hybrid methods”. The three kinds of methods will be separately reviewed in what follows.

1.2.1.1 Enhanced Deterministic Methods

One type of the enhanced deterministic methods aims at improving the efficiency of the FEM. As an example, the Component Modal Synthesis (CMS) models [11-15] were developed to speed up finite element computations and to increase the frequency range of applicability of this method. Each component is separately treated in terms of its uncoupled modes. All components are then assembled using basis functions defined on the interface. There is a large amount of literature devoted to CMS models. Only a few representative works are reviewed here. For example, Craig [16] compares the efficiency of using different component modes and concludes that the models based on the interface constraint modes together with fixed-interface normal modes are the most effective. In the early form of the CMS method, the number of the constraint modes is equal to the number of degrees of freedom at the sub-system interface. For sub-systems coupled continuously along a line or a surface, the number of interface modes becomes prohibitive. To reduce the degrees of freedom along the interface, a large amount of works is done [17-23]. For instance, Balmes introduces continuous polynomials that satisfy the continuity conditions at selected "nodes" on the interface, leading to an overall reduction of the interface DoFs [18]. However, the incompatible models problem in FEM [24, 25] cannot be avoided so that the approximation from the selected polynomials might be poor. Based on Balmes's method, a modal-based approach [26] was proposed to describe the mid-frequency vibration transmission from a long-wavelength source and a short-wavelength receiver using the uncoupled free-interface modes, which allows further simplification of the short-wavelength sub-systems. Uncertainty considerations are also taken into account in some low-frequency methods. Mace and Shorter [27] proposed a local modal-

perturbational method that takes the uncertain properties of the system into account for the mid-to-high frequency analyses. Uncertainty is introduced at the subsystem level. A perturbation technique relates small changes in the local modal properties to those in the global modal properties. A Monte Carlo simulation is then used to estimate the variability of the frequency response function statistics. This approach was applied to coupled rods. Other efforts on improving the efficiency of the FEM are also made such as Efficient Solver Method [28], Adaptive Mesh Techniques [29].

Another direction is element free methods developed based on the Trefftz methods, such as the Wave-Based Method (WBM) [30, 31] and the Variational Theory of Complex Rays (VTCR) [32, 33]. In these methods, approximate solutions of the global response are developed by using the exact solutions of sub-system motion as the shape functions and by respecting all the boundary conditions through a weak formulation. In general, the size of the resultant model is much smaller than that of the equivalent FE model, to reach the mid-frequency range. Various versions of such methods exist depending on the choice of the shape functions and the way the boundary conditions and the coupling between subsystems are handled.

In this thesis, main attentions are paid to one of the sub-structure methods, the Patch Transfer Function (PTF) method [34], which was developed for partitioning acoustic [22] or vibro-acoustic [23, 24] problems for enlarging the frequency range of the vibro-acoustic simulation. The PTF method divides the interface into patches using a wavelength-based criterion. For each subsystem, the uncoupled transfer functions between each pair of patches need to be calculated, *a priori*, before being assembled in the final stage. PTF can be seen as an extension of the well-known approach which is commonly used in dynamic analyses for assembling point-coupled mechanical structures. The PTFs can be calculated by different means. For instance, for subsystems of finite sizes, they can be calculated from the subsystem modes for simple

geometry or from the finite element method for complex geometry. For infinitely large acoustic subsystems, they can be estimated from boundary element method or the Rayleigh integral as in [22, 25], or be measured as in [35] for characterizing pore-elastic materials used in automotive.

Though intuitive, question still remains on whether discretization by patches is the best way in terms of calculation efficiency. In fact, for the modeling of large systems, such as the noise transmission through a building of practical size, the number of patches (i.e. the degree of freedom in the discretized system) may be very large when reaching the mid-to-high frequency range. This makes the direct application of the PTF method difficult, if not impossible. To tackle this issue, attempts were made to extend the PTF approach to further explore other types of discretization schemes, aiming at reducing the number of degree of freedoms and increasing the computation efficiency. As a typical example, the CTF approach generalizes the patches, i.e. the basis functions, of the PTF approach to any function sets over the coupling junction such as the complex exponential functions and the Chebyshev polynomials. The sub-system motions, which will be referred to as condensed velocities, are decomposed in terms of the CFs and assembled together along the interface based on continuity conditions. Up to now, the CTF approach has only been applied to the modeling of the interaction between two line-coupled vibrating mechanical systems, exemplified by the coupling between two panels [36] and a naval application involving a cylindrical shell coupled with non-axisymmetric internal frames [37]. Its application to the surface coupled vibro-acoustic system, with the inherently more complex wavelength mixing, has not been dealt with yet.

1.2.1.2 Enhanced Statistical Methods

Compared to the low-frequency methods such as FEM, SEA involves much fewer DoFs of the system so that the computational time can be significantly reduced. Owing to the frequency average and spatial average properties, SEA is more feasible when dealing with uncertainties. However, due to the essential assumptions such as high modal density, etc. SEA is difficult, or even impossible to be applied in long-wavelength sub-systems. One of the attempts is to reexamine the effectiveness of the assumptions behind the SEA to reduce its frequency limit. Some works pay attention to the effect of the coupling strength between sub-systems on the reliability of SEA, including internal damping, Modal Overlap Factor (MOF), modal density within the frequency band of interest, etc. These works aim at quantitatively clarifying the validity of the SEA in terms coupling strengths [38-45] or defining the lower bound of the effective frequency range [8, 46], with no obvious improvement on the effectiveness of the SEA itself.

Another parallel effort is adding more information about modal energy distribution to improve the reliability of the SEA in the low-frequency range, exemplified by the Statistical modal Energy distribution Analysis (SmEdA) [47]. The method consists in relaxing the modal energy equipartition assumption used in the traditional SEA. Instead of using the power balance between subsystems used in the SEA, the power balance equations between the resonant modes of different subsystems are established. Circumventing modal energy equipartition allows the handling of subsystems with a relatively low modal overlap, as well as the evaluation of the spatial distribution of the energy density within subsystems [48]. Similar attempts include energy finite element analysis (EFEA) [49], which improves the SEA by allowing the damping and the

excitation to be spatially distributed over a system. However, similar to other methods based on SEA, the EFEA is limited by the requirement of high modal density, thus hampering its use in the mid-frequency range. Different ideas also focus on the power flow between sub-systems by Mace [50-52]. It is found that the modal coupling between sub-systems can be analytically determined when the coupling strength is weak. The dynamic interactions between modes can be quantitatively described as equivalent modal damping effect, which facilitates the application of the SEA in the mid-frequency range. However, the power flow theory cannot cover all the mid-frequency range and avoid the limitations of the SEA method.

One of the main problems in using the SEA is the weak coupling assumption. It is well accepted that the energy flow between a weakly coupled system is substantially less than the energy dissipated within each subsystem [19, 20], so that some assumptions and simplifications made under the weak coupling conditions might become invalid in the strong coupling cases. For example, the plate-cavity system is considered as a typical weak coupling case [12]. The so-called weak coupling assumption applies to either a structural-acoustic system or a pure acoustic system composed of multiple sub-cavities. For the former, the fluid-loading effect on a mechanically excited structure is considered to be weak and negligible; for the latter, the acoustic response of an acoustically excited sub-cavity remains essentially the same no matter whether the connecting interface with its adjacent acoustic neighbor is open or closed as a rigid wall. Therefore, examining the applicability of the proposed method in this thesis in a context of increasing coupling strength is required. This, however, brings up two challenging issues that the present work attempts to address and to contribute to the existing knowledge. The first one, which is of general relevance, is to establish a metric to quantify the coupling strength level in a coupled

system. Along the same line of thinking, a very useful coupling strength quantification method was proposed [12], which applies to two coupled single DoF sub-systems. Therefore, a more general assessment method is needed, especially in the mid-to-high frequency context. The second one, more specific to the method itself, concerns the assessment of its applicability and the accuracy in dealing with cases when the coupling becomes stronger.

1.2.1.3 Hybrid Deterministic-Statistical Methods

The hybrid deterministic-statistical approaches, which combine the low-frequency methods and the SEA by capitalizing on their respective advantages, originate from the structural fuzzy theory [10]. The target complex system is divided into a master structure and several fuzzy attachments, which can be modeled by different methods. These hybrid methods allow adding more details to the classical SEA model whilst avoiding the handling of the entire system by the low-frequency methods like FEM. Typical procedures to implement a hybrid analysis is:

1) Divide the whole system into long-wavelength deterministic sub-systems and short-wavelength statistical sub-systems.
2) Model the long-wavelength sub-system with the low-frequency methods and model the short-wavelength sub-system with the SEA method.
3) Determine the boundary conditions at interfaces between sub-systems.
4) Assemble the hybrid model.

Basically, all hybrid methods follow the above procedures and can be divided into two main types, depending on the low-frequency methods used. One possibility is to use the FEM to model the long-wavelength sub-systems [9, 53-61]. Other options

require analytical solutions such as WBM rather than FEM as the low-frequency method [62-64]. Nevertheless, they have similar performance in terms of the final outcomes: detailed predictions for the long-wavelength sub-systems and statistical predictions on the averaged energy response for the short wavelength sub-systems. With the assistance of the SEA, the uncertainties within the short-wavelength sub-systems can be better considered [65-67]. The difference is the FEM is more feasible but less efficient while the WBM is more efficient but has difficulties at the model building stage. However, no matter which low-frequency method is used, detailed predictions for the short wavelength sub-systems are unavailable.

1.2.2 Methods for Classical Plate-Cavity Systems

The panel-cavity system, comprising a parallelepiped acoustic cavity with a rectangular flexible panel subjected to external excitations, has been used as a benchmark problem for studying the fundamental problems in a vibro-acoustic system for more than half a century. The issue of the pressure and velocity continuity at the structure-cavity interface using modal-based method has been arousing persistent interest and long-lasting debate among researchers. This thesis intends to clarify this issue of fundamental importance.

The vibration response of a cavity-backed rectangular panel was first investigated by Dowell and Voss [68]. Since then, there has been a continuous effort in improving the modeling of such system as well as its physical understanding, exemplified by the work of Pretlove [69-71] and Guy [72-76], mainly focusing on quantities like the panel vibration, acoustic pressure, acoustic velocity and the reverberant time inside the cavity etc. Without any doubt, the most convenient and presumably the most

commonly used method is the modal-based approach using acoustic pressure (or potential) decomposition over acoustic modes of the rigid-walled cavity. Its general framework, also referred to as the acoustoelasticity theory, was elegantly summarized by Dowell [1] and Fahy [77]. This approach, however, suffers from the seemingly "flaw" in that the velocity continuity over the panel cannot be mathematically satisfied due to the use of the rigid-walled acoustic modes, expressed in Cosine functions in the case of parallelepiped cavity [78]. This problem arouses continuous interest and endless debate in the vibro-acoustic community, even up to now. The advocators of the method argue that the method allows accurate acoustic pressure and reasonable acoustic velocity prediction if a sufficient number of acoustic modes are used. Nevertheless, there are no ruling conclusions due to the lack of quantified assessment and criteria. Various techniques were also developed in an attempt to increase the calculation accuracy such as the use of extended mode shape functions for a single cavity or the coupling between two overlapped adjacent sub-cavities [79]. Meanwhile, the skepticism on the modal-based method has always been persistent as evidenced by some recent papers. For example, the deficiencies of the method based on rigid-walled modes were reiterated by Ginsberg [80], who employed an extension of Ritz series method to the problem, and the modified formulation is found to be accurate above the fundamental rigid-cavity resonance frequency for light fluid loading. More recently, various series expressions with added terms were also proposed to accommodate the velocity continuity [81, 82].

1.2.3 Modeling Methods in Building Acoustics

The history of building acoustics begins with the famous reverberation formula proposed by Sabine in 1990. Since then, many works were conducted based on Sabine's formula [83-85]. However, as the development of analyzing tools and computational resources, people becomes unsatisfied with the few information provided by a single formula. Although the formula is proved to be very effective as a reference, more details of the building system are required to design and optimize the acoustic performance. Therefore, many branches of building acoustics arise such as room acoustics [86-96], structure-borne noise [97-108], air-borne noise [109-125], noise reduction techniques [126-141], etc. This thesis mainly focuses on air-borne prediction and noise absorption problem.

1.2.3.1 Prediction Methods in Building Acoustics

The airborne noise is generated acoustically and transferred either structurally or acoustically to rooms or between floors through different paths such as walls, glasses, floors, or other connections. The sound energy reduced when transmitted via these paths is often noted as sound insulation, which can be approximated predicted based on the mass law. Many optimized tools are developed based on the mass law [109-111], to take more system parameters into account. However, to achieve better design and optimization, researchers also opt for traditional calculation methods in building acoustics. Discretization methods and sub-structuring methods have been widely applied to predict the insulation performance of building elements [123-125]. Most of them are focused on the prediction of sound transmission through double-partition

structures. Based on the virtual work principle, Wang *et al*. proposed a fully coupled model for a double-leaf partition structure, which is connected together through periodically mounted studs [125]. However, to obtain the analytical solution, many assumptions are made such as the infinite size of the partition. Arjunan *et al*. [113] develop a 2D FEM to predict the Sound Reduction Index (SRI) of a stud based double-leaf wall of finite size. However, it is difficult to extend the method for 3D analyses due to a large number of meshes. It is shown that at least 8 elements per wavelength are needed to obtain a reliable result [114]. The Finite Layer Method (FLM) [123] makes an improvement upon the computational efficiency. The FLM uses the modal decomposition technique to model the two in-plane directions of the partition and the FEM to model the perpendicular direction. The FLM significantly improves the calculation efficiency. However, it fails in dealing with the opening ventilation in a DSF system because the opening usually appears in the same plane with a partition. To take the ventilation structure into account, Urban *et al*. established a simple model that could predict the naturally ventilated DSF structure with openings [124]. The predictions are roughly based on the sub-system resonance frequencies, dimensions, and material properties. The model is experimentally validated.

1.2.3.2 Noise Absorption

In building acoustics, the room itself is of importance to the sound absorption, of which the loss mechanisms include energy reduction when sound waves are reflected from walls and propagate in the air [142]. Early studies show that the propagation losses of sound can be described by the decrease of the sound intensity, as $I(x) = I_0 \exp(-rx)$, where r depends on the temperature, relative humidity, frequency, etc.

Wall absorption is also unavoidable in practice. It can be very small but still not zero even if the walls are designed to be acoustically rigid. The two effects are usually evaluated altogether by measuring the reverberation time. They can be neglected in the design stage if real absorption devices are added.

Porous materials are popular as a means to provide sound absorption. The major concern in terms of the applications of porous materials is how to predict the acoustic impedance. Various tools are developed, based on the accuracy required and experimental facilities available. The simplest and probably the most famous one should be the empirical formula of the acoustic impedance prediction presented by Delany and Bazley [143], resulting from a large number of experiments conducted to measure the impedance and specific flow resistivity of porous materials. Following their work, sustained improvements are achieved in terms of the measurement and prediction techniques to obtain a more accurate sound absorption coefficient [144-146]. Recently, researchers focus more on the acoustic performance of the porous materials with embedded spring-mass structures [133-137]. Many prediction methods are proposed.

While porous materials are applied to high frequencies and wide bandwidths, Helmholtz Resonators (HRs) are used to tackle the low-frequency tonal noise. As an efficient noise control device, HR has been extensively used in various systems such as double panels [147-149], small enclosures [150-154] and cylindrical shells [155]. In such applications, HRs are mainly used to suppress the lower-order system resonances which are difficult to deal with using classical sound absorption materials. The control performance of the HR, when deployed in an acoustic system, depends not only on the characteristics of the HR itself but also on its coupling with the acoustic modes of the system. Basically, the backing volume of a resonator is large at low-

frequency range. Li and Vipperman proposed a T-shaped resonator to reduce the occupied volume, which allows the embedding of resonators within the wall. An example is shown in Figure 1.2

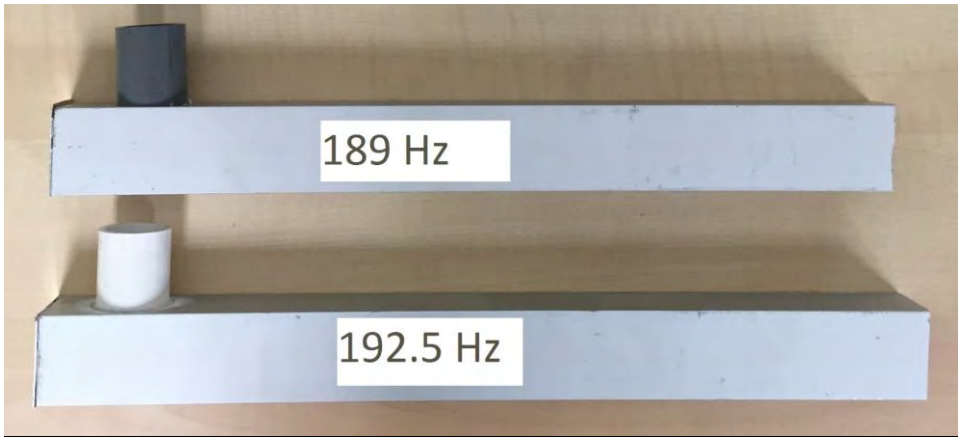

Figure 1.2 T-shaped acoustic resonators.

In this thesis, the main attention will be paid to the Micro-Perforated Panel (MPP) as first introduced by Maa [156]. Later on, Maa proposed the use of cavity backed MPP as absorbers (MPPA). Examples are shown in Figure 1.3.

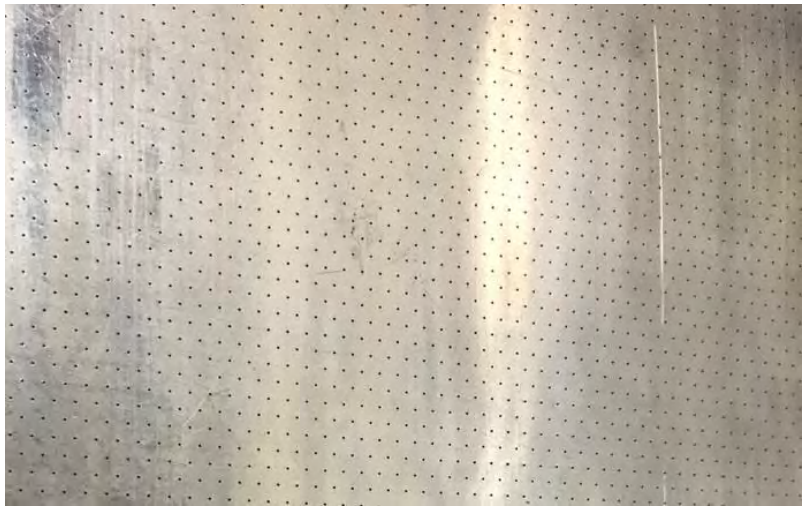

(a)

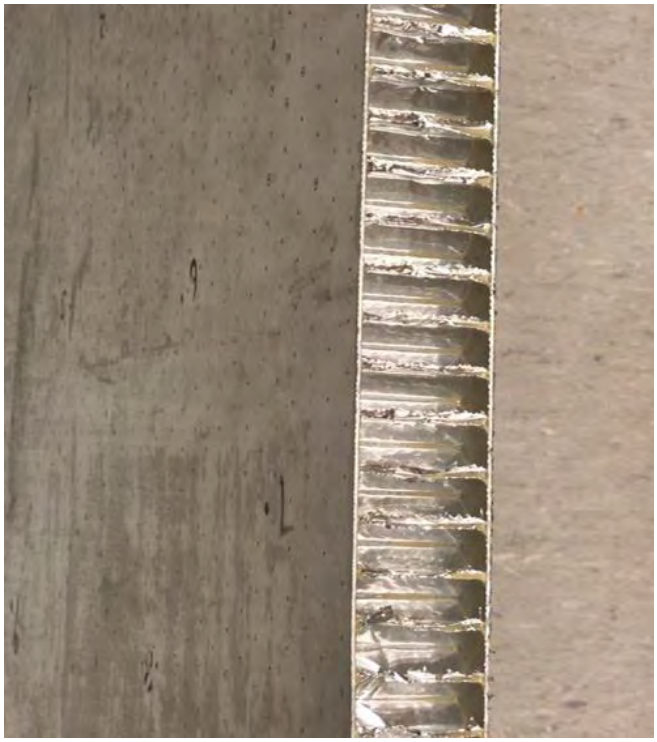

(b)

Figure 1.3 (a) Sample of a micro-perforated panel; (b) Sample of a micro-perforated panel absorber.

Since then, a large number of applications of MPP can be found in various applications such as ducts, mufflers, and buildings, etc. It is also found that the MPP may be used without a backing cavity [157]. The sound absorption process occurs as long as the acoustic pressure difference exists on the two sides of the hole. This conclusion implies that the MPP cannot be only considered as a locally reacting element in a complex acoustic environment. A similar conclusion is also drawn by removing the internal partition of the backing cavity of the MPP which allows the interaction between different holes [158]. Recent progress shows that the interaction between holes can be utilized to improve the performance of a traditional MPPA, by optimizing the acoustic field within the backing cavity to match the acoustic field outside [159].

1.3 Research Scope and Thesis Outline

This thesis aims at providing a simulation tool that can balance the calculation efficiency and the quantity of information obtained in the mid-to-high frequency range. Development is made under the sub-structuring framework, based on the previously mentioned PTF method.

The targeted objectives of the thesis are listed as follows:

1) To find a benchmark solution for the validations of the mid-to-high frequency modeling method.
2) To extend the CTF method from line-coupled systems to surface-coupled systems.
3) To establish a mid-to-high frequency method based on the CTF approach, which can balance its performance and computational efficiency.
4) To define a coupling strength quantification method, which should well reflect the interaction between two coupled sub-systems.
5) To validate the proposed mid-to-high frequency method in systems of various coupling strength.
6) To apply the proposed method to a typical building acoustic problem to assess its capability through parametric study and system analyses.

The outline of the thesis is as follows.

In Chapter 2, some preparation works are conducted. Solutions for a vibrating plate coupled to an acoustic cavity, which is usually used as the benchmark representing a simplified system in vibro-acoustic problems, are presented. Through the exploration

of the two popular methods, e.g. the modal method and the wave method, the well-recognized existing convergence difficulties of the latter at the vicinity of the vibro-acoustic interface are investigated. A criterion to accelerate the convergence speed of the modal method close to the cavity-plate interface is proposed. Through numerical analyses and comparisons with the wave method, an oscillating convergence pattern is revealed. Normalization of the results leads to a unified series truncation criterion, which ensures a minimal error in the prediction of the acoustic particle velocity. While improving the reliability of the classical modal method, this part of the work paves the way forward by providing a reference solution for the mid-to-high frequency modeling analysis.

Then, a so-called Condensed Transfer Function (CTF) method is proposed in Chapter 3, which can be classified into the broad category of sub-system methods. In the proposed method, the uncoupled sub-systems are modeled individually by decomposing the force and velocity over the coupling interface into a set of orthogonal functions, namely the Condensation Functions (CFs). Then the subsets obtained from each sub-system are assembled following the velocity continuity and force equilibrium conditions over the interface.

In Chapter 4, focuses are put on how to increase the calculation efficiency of the CTF method by properly selecting the Condensation Functions and exploiting their physical characteristics. In particular, owing to the spatial wavy features, the complex exponential functions are expected to better match the structural wavelength variations in a given frequency band, so as the velocity on the interface can be described by a much-reduced subset of the condensation function as compared with spatially discrete functions or other continuous functions. It is shown that the complex exponential functions outperform the previously developed Patch Transfer Function methods

using gate functions. Meanwhile, it can avoid the boundary convergence difficulties encountered when using only trigonometrical functions. Numerical analyses reveal a piecewise convergence behavior of the calculation in different frequency bands. This property is further exploited in a plate-cavity system for establishing a criterion for the truncation of the CFs, referred to as the piecewise scheme. The proposed criterion allows the determination of a subset of the CFs for any prescribed frequency band for the calculation of the system response in a progressive and piecewise manner, resulting in a great increase in the computational efficiency. The proposed method is assessed from different angles using a plate-cavity system, which is conventionally acknowledged as a weak coupling system.

As stated in the literature review, the capability of the modeling of strongly coupled systems should be one of the main requirements for the piecewise scheme. Therefore, in Chapter 5, piecewise scheme is validated under strong coupling cases. To this end, the quantification of the coupling strength between any two sub-systems is first investigated, leading to the establishment of a coupling strength factor (CSP). Parameters that determine the coupling strength between the sub-systems are then discussed. Using the defined CSP, the previously established piecewise scheme is re-examined and validated using an acoustic system comprising two mutually connected sub-cavities. The coupling strength is tuned through tactically changing system parameters. The effect of the coupling strength on the computational error of the piecewise scheme is systematically quantified. The piecewise scheme, alongside the CTF approach itself, is then experimentally validated.

Finally, the piecewise scheme is applied to a simplified DSF system, consisted of two glass panes, two full/partial cavities and integrated sound absorbing devices using micro-perforated panels. The system is thoroughly studied using the proposed

simulation method in terms of frequency responses, sound insulation performance, energy transmission path, as well as the physical mechanism of the sound absorption devices. It is shown that the proposed modeling methodology allows a fine and detailed description of this complex vibro-acoustic system with a relatively complex and large dimension in the entire frequency range including the mid-to-high one.

CHAPTER 2 Benchmark Solutions

A benchmark solution is necessary for the validation of the proposed mid-to-high frequency method in this thesis. As mentioned in the last chapter, the plate-cavity system is a typical benchmark problem, widely used in the vibro-acoustic community. After giving the analytical model for a vibrating plate and an acoustic cavity, this chapter presents the commonly used reference solutions to a plate-cavity coupled system. Meanwhile, the study will clarify the existing controversies over the two methods, the wave method and the modal method, in terms of velocity convergence, which represents a scientific contribution by itself. Usually, the wave method is considered to be more reliable than the modal method, because the basis function in the wave method can better match the boundary condition over the coupling interface while the acoustic modal functions fail to do so in the modal method. Aiming at clarifying this problem, the two methods are systematically compared. A fast convergence criterion is proposed by utilizing the mode characteristics used in the modal method. Finally, reliable results can be obtained from both the wave method and the modal method.

2.1 Analytical Solutions for a Single System

Since this part of the work is tidily related to the bending plate and acoustic cavity, analytical solutions of a rectangular plate and a rectangular acoustic cavity are first presented.

2.1.1 Vibrating Plates

The bending vibrations of a flexible thin plate as shown in Figure 2.1 are governed by

$$D\nabla^4 w + \rho_s h \frac{\partial^2 w}{\partial t^2} = 0, \tag{2.1}$$

where w is the transverse displacement, ρ_s is the plate density, h is the plate thickness, and $D = \frac{Eh^3}{12(1-\nu^2)}$ is the bending stiffness of the plate in which E and ν are the Young's modulus and the Poisson's ratio of the plate, respectively. When w is two-dimensional, 2.1 can be further written, by neglecting the shear deformation and the rotary inertia, as:

$$D\left(\frac{\partial^4 w}{\partial x^4} + 2\frac{\partial^4 w}{\partial x^2 \partial y^2} + \frac{\partial^4 w}{\partial y^4}\right) + \rho_s h \frac{\partial^2 w}{\partial t^2} = 0, \tag{2.2}$$

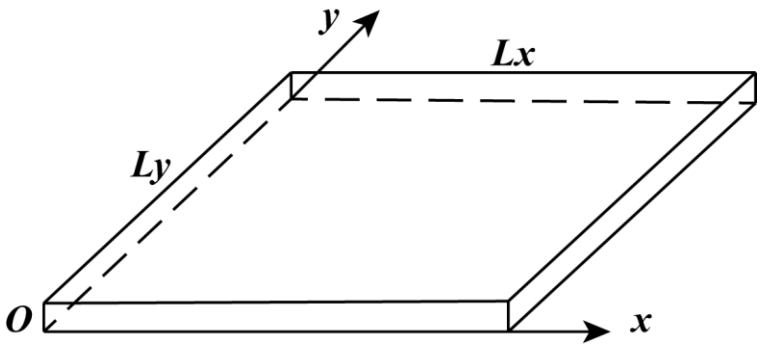

Figure 2.1 Configuration of the vibrating plate.

Consider a harmonic plane wave $w(x,y,t) = \tilde{w}e^{j(\omega t - k_x x - k_y y)}$ and substitute into Eq. 2.2, yields:

$$[D\left(k_x^4 + 2k_x^2 k_y^2 + k_y^4\right) - \rho_s h\omega^2]\tilde{w} = 0. \tag{2.3}$$

Substitute $k_b^2 = k_x^2 + k_y^2$ into Eq. 2.3, one obtains:

$$Dk_b^4 - \rho_s h\omega^2 = 0. \tag{2.4}$$

Equation 2.4 is the bending wave equation for a wave which travels in a direction at angle $\theta = \arctan k_y/k_x$ to the x axis and possesses a wavenumber $k_b = (\omega^2\rho_s h/D)^{1/4}$.

Assuming the plate is subject to a harmonic pressure excitation $P_e(x,y)$, the displacement w can be solved as modal superposition with mode shape $\phi_m(x,y)$ where m = 1, 2, …, as:

$$\tilde{w}(x,y) = \sum_{m=1}^{\infty} \frac{\phi_m(x,y)\tilde{p}_{e_m}}{M_m(\omega_m^2 - \omega^2)}, \tag{2.5}$$

where η_m is considered constant in this thesis as $E^* = E(1 + j\eta_s)$, $\tilde{p}_m$ and M_m are the modal force and the modal mass which are written as:

$$\tilde{p}_{e_m} = \int_0^{L_y}\int_0^{L_x} p_e(x,y)\,\phi_m(x,y)\,dxdy,$$
$$M_m = \rho_s h L_x L_y \int_0^{L_y}\int_0^{L_x} \phi_m^2(x,y)\,dxdy, \tag{2.6}$$

respectively, and ω_m is the mth natural frequency depending on the boundary conditions of the four edges of the plate. The natural frequencies for a rectangular plate with any boundary condition combinations among simply supported, clamped, and free can be found in [160]. The present work mainly focuses are on the simply

supported plates and clamped plates. For the former, the natural frequency and the mode shape can be expressed as:

$$\omega_m = \sqrt{\frac{D}{\rho_s h}}\left[\left(\frac{m_x \pi}{L_x}\right)^2 + \left(\frac{m_y \pi}{L_y}\right)^2\right], \tag{2.7}$$

$$\phi_m = \sin\left(\frac{m_x \pi}{L_x}\right)\sin\left(\frac{m_y \pi}{L_y}\right)$$

For the later, analytical solution is unavailable. Numerical solutions can be found in various references or obtained from numerical methods. In this thesis, the natural frequencies and the mode shapes of the clamped plate are obtained from COMSOL software.

2.1.2 Acoustic Cavity

Consider an acoustic cavity as shown in Figure 2.2. The acoustic pressure $p(x, y, z, t)$ within the cavity is governed by:

$$\nabla^2 p - \frac{1}{c^2}\frac{\partial^2 p}{\partial t^2} = 0, \tag{2.8}$$

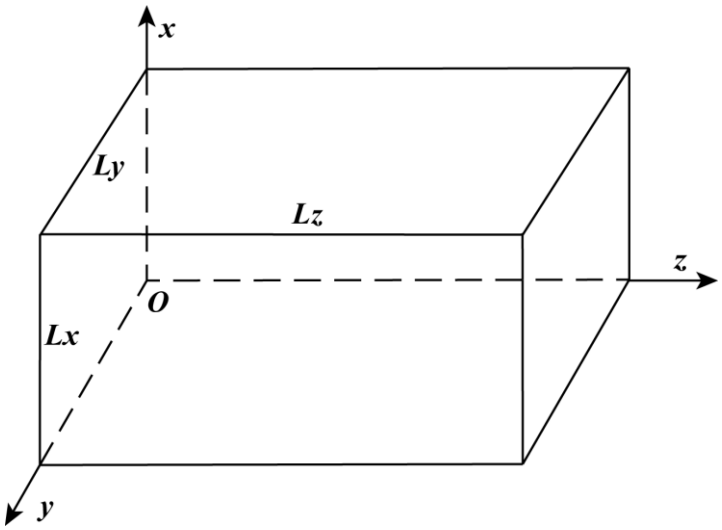

Figure 2.2 Configuration of the acoustic cavity.

Assuming all surfaces of the cavity are acoustically rigid, the normal component of the acoustical particle velocity becomes zero at all boundaries:

$$\left.\frac{\partial p}{\partial x}\right|_{x=0} = 0, \left.\frac{\partial p}{\partial x}\right|_{x=L_x} = 0$$

$$\left.\frac{\partial p}{\partial y}\right|_{y=0} = 0, \left.\frac{\partial p}{\partial y}\right|_{y=L_y} = 0 \qquad 2.9$$

$$\left.\frac{\partial p}{\partial z}\right|_{z=0} = 0, \left.\frac{\partial p}{\partial z}\right|_{z=L_z} = 0$$

Write $p(x, y, z, t)$ in the following form:

$$p(x, y, z, t) = \boldsymbol{X}(k_x x)\boldsymbol{Y}(k_y y)\boldsymbol{Z}(k_z z)e^{j\omega t}. \qquad 2.10$$

Substitution of Eq. 2.10 into Eq. 2.8 and separation of variables result in the following set of equations

$$\left(\frac{d^2}{dx^2} + k_x^2\right)\boldsymbol{X} = 0,$$

$$\left(\frac{d^2}{dy^2} + k_y^2\right)\boldsymbol{Y} = 0, \qquad 2.11$$

$$\left(\frac{d^2}{dx^2} + k_z^2\right)\boldsymbol{Z} = 0,$$

where the angular frequency is given by:

$$\left(\frac{\omega}{c}\right)^2 = k^2 = k_x^2 + k_y^2 + k_z^2. \qquad 2.12$$

On the other hand, the boundary conditions in Eq. 2.9 imply that the cosine functions are the required modal solutions. Equation 2.10 becomes the summation of:

$$p_n = \tilde{p}_n \cos k_{n_x} x \cos k_{n_y} y \cos k_{n_z} z \, e^{j\omega_n t} \qquad 2.13$$

where n = 0, 1, 2… and

$$k_{n_x} = \frac{n_x \pi}{L_x}, n_x = 0, 1, 2, \ldots$$

$$k_{n_y} = \frac{n_y \pi}{L_y}, n_y = 0, 1, 2, \ldots \quad 2.14$$

$$k_{n_z} = \frac{n_z \pi}{L_z}, n_z = 0, 1, 2, \ldots$$

Thus, the natural frequencies and the mode shapes of the cavity can be obtained by substituting Eq. 2.14 into Eqs. 2.12 and 2.13 as:

$$\omega_n = c\sqrt{(\frac{n_x \pi}{L_x})^2 + (\frac{n_y \pi}{L_y})^2 + (\frac{n_z \pi}{L_z})^2}, \quad 2.15$$

$$\phi_n(x, y, z) = \cos\left(\frac{n_x \pi x}{L_x}\right)\cos\left(\frac{n_y \pi y}{L_y}\right)\cos\left(\frac{n_z \pi z}{L_z}\right).$$

Assuming a harmonic sound source with volume velocity strength Q_s is located at the point $\boldsymbol{r}_s = (x_s, y_s, z_s)$, the acoustic field within the cavity can be described by the acoustic velocity potential ψ, which has the same modal shapes as the acoustic pressure p:

$$p = -\rho_0 \dot{\psi}. \quad 2.16$$

Then, the acoustic velocity potential within the cavity is governed by:

$$\nabla^2 \psi(\boldsymbol{r}, t) - \frac{1}{c^2}\frac{\partial^2 \psi(\boldsymbol{r}, t)}{\partial t^2} = Q_s(t)\delta(\boldsymbol{r} - \boldsymbol{r}_s). \quad 2.17$$

Applying the orthogonal properties of the eigenfunctions and substituting Eq. 2.16 into Eq. 2.17, one obtains the pressure field distribution within the cavity:

$$p(x, y, z) = -i\omega Q \rho_0 c^2 \sum_n \frac{\phi_n(x, y, z)\phi_n(x_s, y_s, z_s)}{\Lambda_n(\omega_n^2 - \omega^2)}, \quad 2.18$$

where η_n is modal damping factor, expressed as $c^* = c(1 + j\eta_a)$ and Λ_n is nth acoustic modal mass written as:

$$\Lambda_n = \int_0^{L_z} \int_0^{L_y} \int_0^{L_x} \phi_n^2(x, y, z)\, dxdydz. \tag{2.19}$$

2.2 Analytical Solutions for the Plate-cavity System

In this section, two representative analytical solutions of the plate-cavity system are presented, which are the wave method and the modal method. The wave method begins from establishing an exact wave basis that satisfies all system boundary conditions. However, in the modal method, as implied by its name, solves the coupled system with uncoupled modes of each sub-system. In the following parts, the implementations of the two methods, as well as their advantages and disadvantages, will be systematically discussed based on the configuration shown in Figure 2.3.

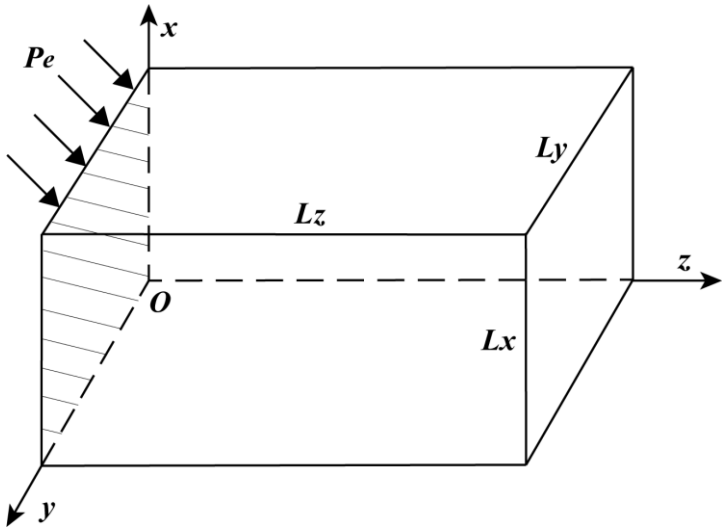

Figure 2.3 Configuration of the plate-cavity system.

2.2.1 The Wave Based Method

2.2.1.1 Theoretical analyses

Consider the system configuration as shown in Figure 2.3. Apparently owing to the existence of the vibrating plate, the mode shapes of the acoustic pressure within the cavity, as well as those of the velocity potential, are different from those in Eq. 2.15 in the *z*-direction. The boundary conditions at *z*=0 have to be changed to:

$$\left.\frac{\partial p}{\partial z}\right|_{z=0} = v, \left.\frac{\partial p}{\partial z}\right|_{z=L_z} = 0. \tag{2.20}$$

To find a solution that satisfies the boundary conditions in Eq. 2.20, we write the wave pattern in the *z*-direction in the following form:

$$\phi_z(z) = Acosh(kz) + Bsinh(kz). \tag{2.21}$$

Equation 2.21 could describe any propagating wave along the *z*-axis. Taking *x* and *y* directions into account, the new mode shapes of the cavity, as well as their modal amplitudes, can be written as:

$$\phi_n(x,y,z) = \cos(\frac{n_x \pi x}{L_x})\cos(\frac{n_y \pi y}{L_y})[Acosh\left(k_{n_x n_y} z\right) + Bsinh\left(k_{n_x n_y} z\right)]. \tag{2.22}$$

where

$$k_{n_x n_y} = \sqrt{(\frac{n_x \pi}{L_x})^2 + (\frac{n_y \pi}{L_y})^2 - \frac{\omega^2}{c^2}}. \tag{2.23}$$

Substitution of the boundary conditions in Eq. 2.20 into Eq. 2.21, one obtains:

$$\phi_z(z) = -v\frac{\cosh[k(L_z - z)]}{ksinh(kL_z)}. \tag{2.24}$$

Because *v* is the velocity of the vibrating plate, it is not a single number but a function *v*(*x, y*). Decomposing *v*(*x, y*) into the cavity modal basis as:

$$\tilde{v}_{n_x n_y} = \int_0^{L_x} \int_0^{L_y} v(x,y) \cos\left(\frac{n_x \pi x}{L_x}\right) \cos\left(\frac{n_y \pi y}{L_y}\right) dxdy, \tag{2.25}$$

Equation 2.22 can be rewritten as:

$$\phi_n(x,y,z) = -\cos(\frac{n_x \pi x}{L_x})\cos(\frac{n_y \pi y}{L_y}) \frac{\tilde{v}_{n_x n_y} \cosh[k_{n_x n_y}(L_z - z)]}{k_{n_x n_y} sinh(kL_z)}. \tag{2.26}$$

The next target is to find the plate velocity *v*(*x, y*) when the plate is backed by the acoustic cavity, which can be solved by adding force equilibrium terms on the right-hand side of Eq. 2.1:

$$D\nabla^4 w + \rho_s h \frac{\partial^2 w}{\partial t^2} = P_e - p, \tag{2.27}$$

where P_e and p are the external excitation pressure and the acoustic pressure within the cavity induced by the plate vibration, respectively. *p* can be obtained from the Euler's equation together with the acoustic velocity potential as:

$$p = -\rho_0 \frac{\partial \phi}{\partial t}, \tag{2.28}$$

Substituting Eq. 2.26 into Eq. 2.28, we obtain *p* in Eq. 2.27 as

$$p(x,y) = \sum_{n_x, n_y} \frac{j\omega\rho_0 \tilde{v}_{n_x n_y}}{k_{n_x n_y}} \cos\left(\frac{n_x \pi x}{L_x}\right) \cos\left(\frac{n_y \pi y}{L_y}\right) \coth\left(k_{n_x n_y} L_z\right) \tag{2.29}$$

When the velocity is set to unity, we can write the cavity impedance Z_{n_x,n_y} at the plate surface for mode (n_x, n_y) as:

$$Z_{n_x,n_y} = \frac{j\omega\rho_0}{k_{n_x n_y}} \coth\left(k_{n_x n_y} L_z\right). \tag{2.30}$$

To achieve the summation calculation between P_e and P_a, P_e is also decomposed into the cavity modal coordinate as

$$\tilde{p}_{e_{n_x n_y}} = \int_0^{L_x} \int_0^{L_y} P_e(x,y) \cos\left(\frac{n_x \pi x}{L_x}\right) \cos\left(\frac{n_y \pi y}{L_y}\right) dxdy. \tag{2.31}$$

Then, summation calculation can be conducted between each pair of P_e and P_a with the same (n_x, n_y). On the other hand, because the plate is assumed to be simply supported at all four boundaries, $v(x, y)$ can be written as:

$$v(x,y) = \sum_{m_x, m_y} \tilde{v}_{m_x m_y} \sin\left(\frac{m_x \pi}{L_x}\right) \sin\left(\frac{m_y \pi}{L_y}\right). \tag{2.32}$$

Obviously, Eq. 2.32 is not in the same function basis as the excitations in Eq. 2.29 and 2.31. To solve Eq. 2.27 with the modal decomposition approach, the function basis of the plate and the excitations must be generalized along x and y directions. Thus, define the modal transformation coefficient as

$$\mathrm{B}_{m,n} = \int_0^{L_x} \int_0^{L_y} \sin\left(\frac{m_x \pi}{L_x}\right) \sin\left(\frac{m_y \pi}{L_y}\right) \cos\left(\frac{n_x \pi x}{L_x}\right) \cos\left(\frac{n_y \pi y}{L_y}\right) dxdy. \tag{2.33}$$

By calculating the integral in 2.33, $\mathrm{B}_{m,n}$ can be written as:

$$\mathrm{B}_{m,n} = \begin{cases} \dfrac{L_x L_y}{\pi^2} \dfrac{m_x m_y [(-1)^{n_x + m_x} - 1][(-1)^{n_y + m_y} - 1]}{(n_x{}^2 - m_x{}^2)(n_y{}^2 - m_y{}^2)} \\ 0, \qquad\qquad n_x = m_x \; or \; n_y = m_y \end{cases}. \tag{2.34}$$

$\mathrm{B}_{m,n}$quantifies the coupling strength between plate mode (m_x, m_y) and cavity mode (n_x, n_y, n_z). Obviously, the coupling is determined by the parity of the modes in x and y directions and independent of n_z for a given vibrating surface. The coupling relationship is summarized in Table 2.1. As shown in the literature, the coupling between the modes of the plate and the cavity occurs in a very selective manner.

Table 2.1 The relationship between the mode number parity and the modal coupling: (o: odd number; e: even number)

Plate modes (m_x, m_y)	Cavity modes (n_x, n_y, n_z)			
	(o, o, -)	(o, e, -)	(e, e, -)	(e, o, -)
(o, o)	0	0	Non-zero	0
(o, e)	0	0	0	Non-zero
(e, e)	Non-zero	0	0	0
(e, o)	0	Non-zero	0	0

Then, the plate velocity can be obtained from Eq. 2.5, by substitution of Eqs. 2.29, 2.31, and 2.33 and taking the derivative with respect to time, as:

$$v(x,y) = j\omega \sum_{m,n}^{\infty} \frac{\phi_m(x,y)(\tilde{p}_{e_m} - \tilde{p}_m)}{M_m(\omega_m^2 - \omega^2)}. \tag{2.35}$$

From Eq. 2.35, we can extract the plate mobility and expanding the index *m* as:

$$Y_{m_x,m_y} = \frac{j\omega}{M_{m_x,m_y}(\omega_{m_x,m_y}^2 - \omega^2)}. \tag{2.36}$$

In the above deduction, we write the pressure under the cavity modal basis. Therefore, firstly we write the relationship between $\tilde{p}_{e_n}$ and $\tilde{p}_n$ for a given "*n*", by substituting 2.30, 2.35, and 2.36 into Eq. 2.29, as:

$$\sum_m B_{m,n}\tilde{p}_{e_n} Z_n Y_m = \sum_m B_{m,n}\tilde{p}_n(1 + Z_n Y_m). \tag{2.37}$$

Because $\sum_m B_{m,n}\tilde{p}_{e_n}$ is equivalent to $\tilde{p}_{e_m}$, we can rearrange Eq. 2.37 into a function of $(\tilde{p}_{e_n} - \tilde{p}_n)$ and obtain *m* linear functions as:

$$\sum_m B_{m,n}(\tilde{p}_{e_n} - \tilde{p}_n)(1 + Z_n Y_m) = \tilde{p}_{e_m}. \tag{2.38}$$

Then, $p_{t_m} = \tilde{p}_{e_m} - \tilde{p}_m$ can be resolved into matrix form as:

$$\begin{bmatrix} \tilde{p}_{t_{11}} \\ \vdots \\ \vdots \\ \tilde{p}_{t_{m_x m_y}} \end{bmatrix} =$$

$$\begin{bmatrix} B_{\substack{11\\00}}(1+Z_{00}Y_{11}) & \dots & B_{\substack{11\\n_x n_y}}(1+Z_{n_x n_y}Y_{11}) \\ \vdots & \ddots & \vdots \\ \vdots & \ddots & \vdots \\ B_{\substack{11\\00}}(1+Z_{00}Y_{m_x m_y}) & \dots & B_{\substack{m_x m_y\\n_x n_y}}(1+Z_{n_x n_y}Y_{m_x m_y}) \end{bmatrix}^{-1} \begin{bmatrix} \tilde{p}_{e_{11}} \\ \vdots \\ \vdots \\ \tilde{p}_{e_{n_x n_y}} \end{bmatrix}. \quad 2.39$$

Substitution of Eq. 2.39 into Eq. 2.35, the coupled plate velocity can be obtained. The acoustic pressure within the cavity can be solved by substituting Eq. 2.35 into Eq. 2.29.

2.2.1.2 Incident angle discussions

Before closing the discussions on the wave method, the incident angle of P_e will be discussed as shown in Figure 2.4. Theoretically, three parts constitute the total pressure field at the external side of the plate, which are the incident pressure, reflected pressure, and radiated pressure. Basically, the radiated pressure field is insignificant compared to the other two parts and therefore it is assumed to be neglectable in this thesis. In the normal incident case, the amplitude of the total pressure can be considered to be doubled that of the incident pressure (incident plus reflected), referred to as the blocked pressure. While in the grazing incident cases the total pressure equals to the incident pressure along (no reflected). In other cases, the total pressure amplitude is between the two extreme cases. Detailed discussions are beyond the scope of this thesis. In this thesis, P_e is assumed to represent the total pressure field.

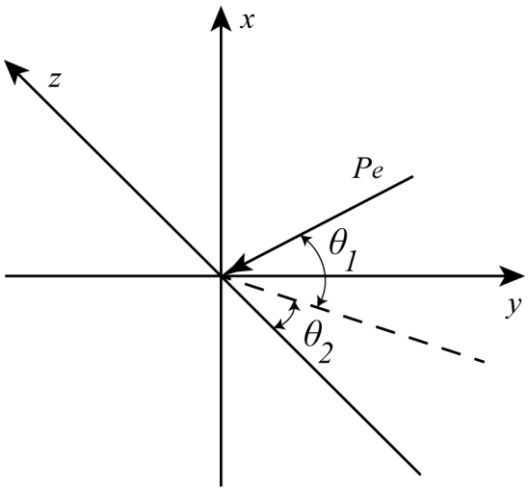

Figure 2.4 The incident angle configuration in the given coordinate.

In the following discussions, the incident angle will be categorized into three scenarios:

1) Normal Incident

The incident pressure is perpendicular to the vibrating plate when both θ_1 and θ_2 are zero. Therefore, $P_e(x, y)$ in Eq. 2.31 is a constant P_e and we can obtain the result of the integral for a given (m_x, m_y) as

$$P_{e_{m_x,m_y}} = \begin{cases} P_e L_x L_y, & n_x = n_y = 0 \\ 0, & else \end{cases}. \quad 2.40$$

Remind the coupling relationship shown in Table 2.1, only "double-odd" plates modes can be excited, which means only one-quarter modes of the system are involved.

2) Grazing Incident

The glazing incident happens when the wavefront of P_e is parallel to the plate and the amplitude of P_e is constant in either *x* or *y* direction. Here we take an example to show the value of $P_{e_{m_x,m_y}}$ when θ_1=90° (θ_2 is null accordingly). P_e is constant in the y direction and $\cos(kx)$ in the x direction. Substitution of $P_e = P_e \cos(kx)$ into Eq. 2.31, we obtain:

$$P_{e_{n_x,n_y}} = P_e \frac{(-1)^{n_x} k L_y \sin(kL_x)}{k^2 - (\frac{n_x \pi}{L_x})^2}. \quad 2.41$$

3) Oblique Incident

For other incident angles, the incident pressure field can be written as $P_e = P_e \cos(k_x x)\cos(k_y y)\cos(k_z z)$ in which

$$k_x = k \sin(\theta_1),$$

$$k_y = k \cos(\theta_1) \sin(\theta_2), \quad 2.42$$

$$\text{and } k_z = k \cos(\theta_1) \cos(\theta_2).$$

Substitution of Eq. 2.42 into Eq. 2.31, we can obtain the modal pressure with the incident angle (θ_1, θ_2) as:

$$P_{e_{n_x,n_y}} = P_e \frac{(-1)^{n_x} k_x \sin(k_x L_x)}{k_x^2 - (\frac{n_x \pi}{L_x})^2} \frac{(-1)^{n_y} k_y \sin(k_y L_y)}{k_y^2 - (\frac{n_y \pi}{L_y})^2}. \quad 2.43$$

If $k_x = n_x \pi / L_x$, the term with respect to *x* direction becomes

$$P_{e_{n_x}} = P_e \frac{(-1)^{n_x} L_x}{2}. \quad 2.44$$

Equation 2.44 can be applied to *y*-direction as well. One may notice that in most cases the oblique incident pressure ($0° < \theta_1, \theta_2 < 90°$) activates more system modes than the other two. Therefore, to better understand and analyze the interaction between the two systems, an oblique incident is assumed on the plate in this thesis except where otherwise provided.

2.2.2 The Modal Method

The modal method solves the cavity with its rigid acoustic modes, which is governed by Eq. 2.8. The rigid acoustic modes are shown in Eq. 2.15 and satisfy the Helmholtz Equation as:

$$\nabla^2\phi_n + (\frac{\omega_n}{c})^2\phi_n = 0. \tag{2.45}$$

The vibrating plate is considered as a Neumann boundary condition as in Eq. 2.20. Then the acoustic field within the cavity can be obtained by substituting Eqs. 2.8, 2.16, and 2.45 into Green's function

$$\int_V (p\nabla^2\phi_n - \phi_n\nabla^2 p)dV = \int_S (p\nabla\phi_n - \phi_n\nabla p)dS, \tag{2.46}$$

where *S* is the surface of the plate. Then, we obtain the function for acoustic mode *n* as:

$$\ddot{p}_n + \omega_n^2 p_n = \frac{\rho_0 c^2}{\Lambda_n}\dot{v}_n, \tag{2.47}$$

where v_n is obtained from Eq. 2.25. Notice the sound velocity *c* is complex to describe the damping effect.

The plate is modeled from Eq. 2.27 as:

$$\ddot{w}_m + \omega_m^2 w_m = \tilde{p}_{e\,m} - \tilde{p}_m, \tag{2.48}$$

In the modal method, we simultaneously solve Eqs. 2.47 and 2.48. Because the boundary velocity in Eq. 2.47 and the cavity acoustic pressure in Eq. 2.48 are decomposed in plate modes and cavity modes respectively, the two sets of equations are coupled through the modal coupling coefficient $B_{m,n}$. Therefore, the final equations are written as:

$$\ddot{p}_n + \omega_n^2 p_n - \frac{\rho_0 c^2}{\Lambda_n}\sum_m B_{m,n}\dot{v}_m = 0, \tag{2.49}$$

$$\ddot{w}_m + \omega_m^2 w_m - \sum_n B_{m,n}\tilde{p}_n = \tilde{p}_{e_m}.$$

The acoustic modal pressure amplitude p_n and the structural modal displacement w_m can be solved accordingly.

Apart from the decomposition of the acoustic field within the cavity, the two methods seem to be mathematically equivalent. However, the philosophy behind the two methods is different. In the wave method, the cavity is considered as an attachment of the plate while in the modal method the plate and the cavity have the same weight and position in the solving procedures. Although the modal method was proved to be inaccurate in various aspects compared to the so-called exact solutions such as wave method, it significantly affects the mid-and-high frequency modeling method afterward. As accepted by most researchers in this area, one of the major disadvantages of the wave method is the difficulty in finding the "wave solution" of a structure, owing to its boundary condition changes and geometry complexity. Therefore, allowing the prediction of a coupled system from the uncoupled modes of each sub-system considerably increase the modeling efficiency.

2.3 Convergence Criteria for the Velocity Continuity of a Plate-cavity System

As shown in the last section, modal-based acoustoelastic formulation allows elegant and clear physical representation and, to the eye of many, is the cornerstone of the vibro-acoustics in dealing with structure-cavity coupling problems. However, the issue of the pressure and velocity continuity at the structure-cavity interface using the modal-based method has been arousing persistent interest and long-lasting debate

among researchers. The controversy and the skepticism surrounding the velocity continuity call for a systematic investigation and clarification, which constitutes the main motivation of the present section. This issue is addressed by investigating both acoustic pressure and particle velocity predictions through comparisons between the modal-based approach and the exact solutions using a system of simple rectangular geometry. For the particle velocity prediction in the vicinity of the plate, an oscillating convergence pattern is observed when the number of acoustic modes increases. Normalization of the results leads to a unified criterion allowing minimization of the prediction error, which is then verified in three-dimensional cases.

In the following numerical investigations, the dimension of the cavity in Figure 2.3 is set to be 0.2m×0.2m×0.5m. A simply supported brass plate is 1.5 mm thick, located at $z = 0$. The air density is 1.29 kg/m^3; the sound speed is 340 m/s; the Young's modulus of the plate is 110×10^9 Pa; the plate's Poisson's ratio is 0.357; the plate density is 8.9×10^3 kg/m^3; η_a and η_p are set to 0.001 and 0.01, respectively. A harmonic acoustic excitation is uniformly impinging on the flexible plate along z direction as in Eq. 2.40. The purpose of using normal incident excitation is to simplify the modal response within the plate-cavity system while retaining its internal physical characteristics.

2.3.1 Pressure Analyses

The sound pressure level (SPL) at a receiving point inside the cavity is calculated as,

$$P = 10\log_{10}\left(\frac{p}{2\times10^{-5}}\right)^2 dB, \tag{2.50}$$

with the external excitation pressure p_i fixed to 1 Pa. To ensure a fair comparison between the modal approach and the wave approach, the number of modes used in the transverse directions *x* and *y* are kept identical. The frequency band of interest is [0, 1000] Hz. It is well accepted that in order to ensure the correct sound pressure calculation, the truncated modal series should contain all these modes, for both the cavity and the plate, with their natural frequencies below αf_{max}, where $\alpha > 1$ is a margin coefficient (typically, α=1.5 or α=2) where f_{max} is the highest frequency under investigation (1000 Hz in the present case). This rule, in which α is equal to two, is referred to as the pressure criterion in this paper. It should be pointed out that this pressure convergence criterion (even by including all lower-order modes) is not a universally accepted robust one. In some cases, especially at frequencies where the system is not very dynamic, like the anti-resonance regions between two well-separated modes, more terms may be needed. In the modal-based and wave methods used in the analyses here, the mode indices are chosen up to $n_x = n_y = n_z = 8$ and $m_x = m_y = 8$, which satisfy the pressure criterion. The first few lower order modes of the uncoupled cavity and the plate are tabulated in Table 2.2. A receiving point is randomly chosen at (0.04, 0.17, 0.01)m. The SPL results are given in Figure 2.5a, in which the exact solution (named wave method in this paper) and the one from the modal method are compared. It can be seen that, upon using the pressure criterion, the pressure predictions by the two methods agree well, although slight differences are observable at some anti-resonance frequencies. Should the SPL be averaged within the entire cavity as

$$\langle \hat{p} \rangle = 10 \log_{10} \int_V p^2 dV, \tag{2.51}$$

these differences should disappear (shown in Figure 2.5b). Similar observations were observed at other points inside the cavity, including those close to the vibrating plate (not shown here). Therefore, it is verified that the modal method can provide sufficient accuracy for acoustic pressure predictions everywhere throughout the cavity by using the well-established pressure criterion.

Table 2.2 Uncoupled resonance frequency of the system

Plate *in-vacuo* Resonance			Cavity Resonance			
m_x	m_y	f_m(Hz)	n_x	n_y	n_z	f_n(Hz)
1	1	128			-	
1	2	319.9	0	0	1	340
2	2	512	0	0	2	680
1	3	640	1	0	0	850
2	3	832	2	0	0	915.5

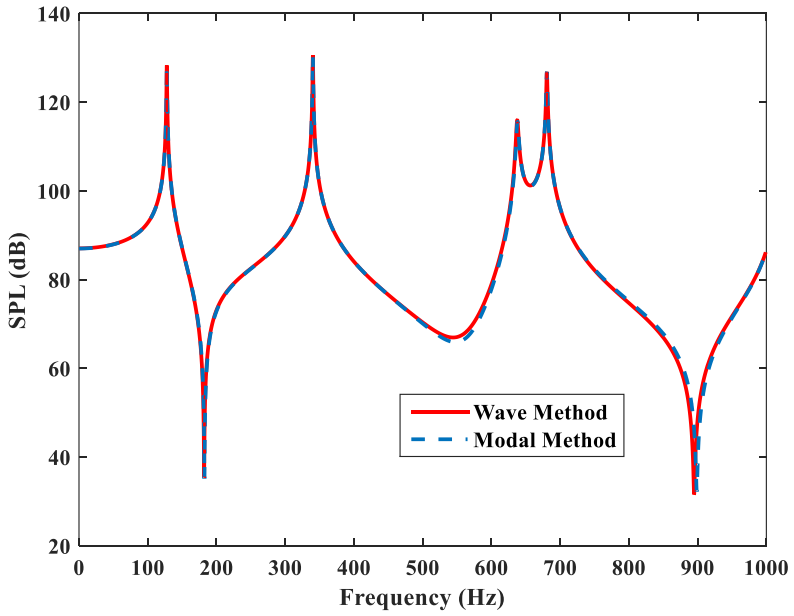

(a)

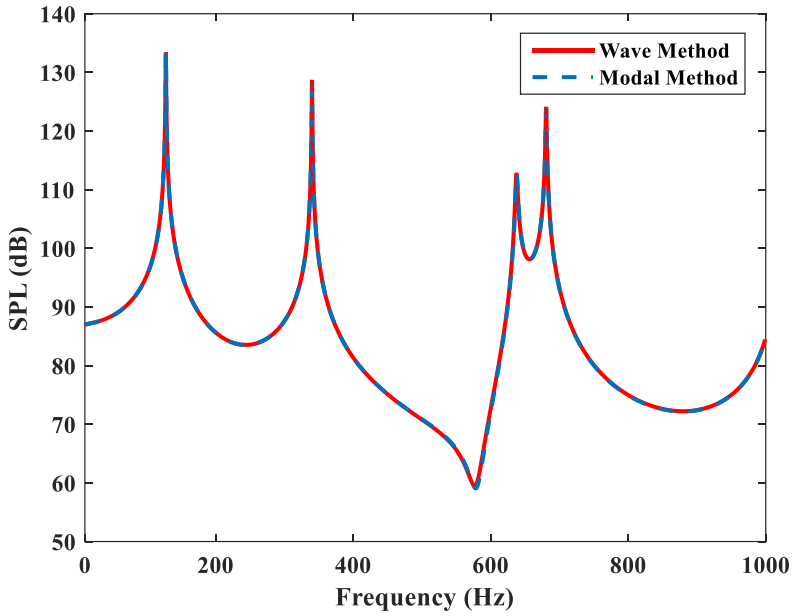

(b)

Figure 2.5 (a) SPL predictions at point (0.04, 0.17, 0.01) m; (b) SPL averaged within the cavity.

2.3.2 Velocity Analyses

As the main focus of this part of the analysis, the prediction accuracy of the particle velocity using modal method is investigated. The receiving point and all other physical parameters are kept the same as in the previous pressure calculation. Since more expansion terms would be needed in the velocity calculation [161], the number of modes used in the modal method is varied. Note that the mode variation only applies to the cavity depth direction, z, whilst the mode terms used in x and y directions are kept the same. Three modal-based calculations use n_z up to 10, 20 and 40, respectively. Acoustic velocity v in the normal direction is obtained from $-j\omega\rho_0 v = \frac{\partial p}{\partial z}$ and the results are shown in Figure 2.6, in comparison with the reference result obtained from

the wave method. Compared with the reference result, it can be seen that the accuracy of the velocity prediction of the modal-based method improves as the number of modes in z direction increases. It is not surprising that at cavity resonance frequencies, 340 Hz and 680 Hz, the convergence is quickly achieved due to the dominating role of the corresponding rigid cavity mode at these frequencies. For the other frequencies, however, the convergence speed is slower than the case of pressure prediction (see Figure 2.5 where only 8 z-direction terms were used). Nevertheless, upon increasing the decomposition terms, sufficient accuracy can still be achieved.

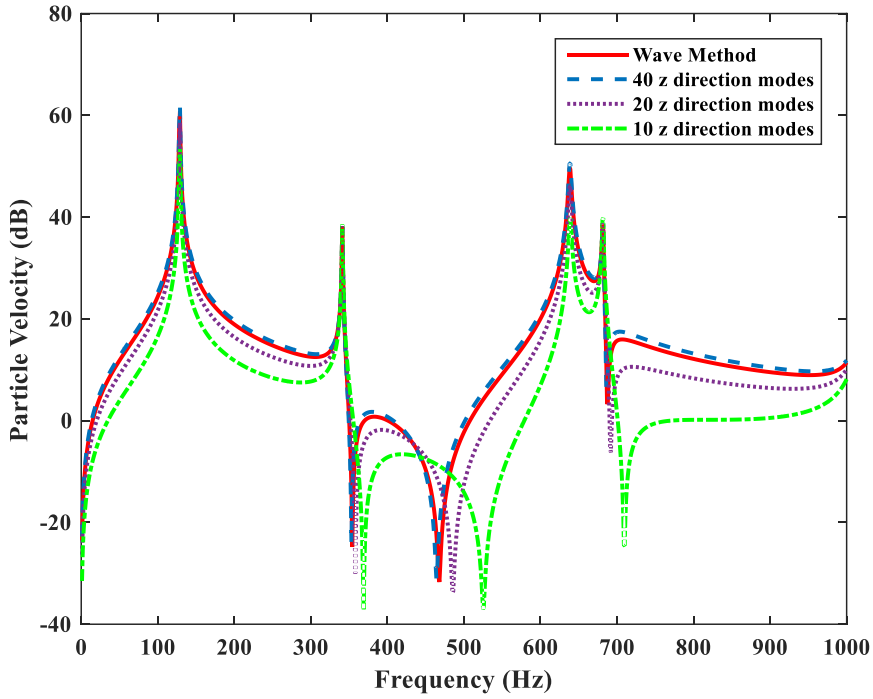

Figure 2.6 Particle velocity predictions by wave method and modal based method: Different z-direction terms are used in the modal method.

To further quantify this observation, a term describing the velocity prediction error is defined as $\Delta V = V_{modal} - V_{wave}$ in dB, calculated and shown in Figure 2.7, in terms of different truncated series in the z direction at an arbitrarily chosen frequency of 210 Hz. It can be observed that the modal-based method quickly approaches the exact

result with a relatively small but increasing number of terms, overshoots and then converges to the exact solution. The convergence, however, is not monotonous with the number of terms used, but in an oscillating manner.

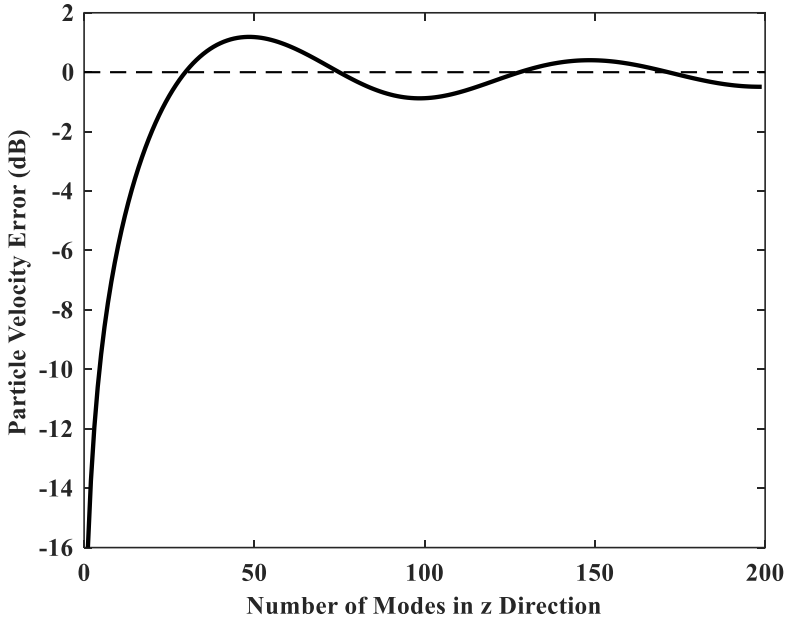

Figure 2.7 Velocity prediction error at point (0.04, 0.17, 0.01) m with respect to the number of modes in the *z*-direction

A close examination of the modal expansion expression of the particle velocity allows to better understand this and eventually to establish a convergence criterion. Derived from Eq. 2.28 and the acoustic pressure solution obtained from Eq. 2.49, the acoustic particle velocity component perpendicular to the plate can be expressed as:

$$v(x,y,z) = \frac{\pi}{\rho_0 L_z} \sum_n \frac{n_z U_{n_x,n_y}(x,y)}{M_n(\omega_n^2 - \omega^2)} \sin\left(\frac{n_z \pi z}{L_z}\right) \qquad 2.52$$

Since only *z*-direction is our focus, upon fixing n_x and n_y, the above expression can then be simplified to a 1-D case as:

$$v(z) = \sum_{n_z} \gamma_{n_z}(\omega) \sin\left(\frac{n_z \pi z}{L_z}\right), \qquad 2.53$$

with

$$\gamma_{n_z}(\omega) = \frac{1}{\rho_0}\frac{U_{n_x,n_y}(x,y)}{M_n(\omega_n^2-\omega^2)}\frac{n_z\pi}{L_z}, \quad 2.54$$

For a given frequency of interest, ω is a constant. In order to ensure a reasonable calculation accuracy, it is well accepted that the modes which need to be included in the calculation should be such that $\omega_n \gg \omega$. Therefore, γ_{n_z} can be approximated by

$$\gamma_{n_z}(\omega) \underset{n_z\to\infty}{\sim} \frac{1}{\rho_0}\frac{U_{n_x,n_y}(x,y)}{M_n\omega_n^2}\frac{n_z\pi}{L_z}. \quad 2.55$$

Moreover, when n_z is large (i.e. $n_z \gg \max[n_x, n_y]$) as in this paper, the modal frequency can be approximated by: $\omega_n \sim c_0\frac{n_z\pi}{L_z}$. Under these conditions, one has:

$$\gamma_{n_z}(\omega) \underset{n_z\to\infty}{\sim} \frac{1}{\rho_0}\frac{U_{n_x,n_y}(x,y)L_z}{M_n c^2\pi}\frac{1}{n_z}. \quad 2.56$$

Since M_n is independent of n_z for $n_z > 0$, $\gamma_{n_z}(\omega)$ is a decreasing function of n_z and satisfies $\lim_{n_z\to\infty}\gamma_{n_z} = 0$. Therefore, according to Abel's theorem, the series $v(z)$ should converge. Meanwhile, an oscillation behavior is expected due to the term $\sin\left(\frac{n_z\pi z}{L_z}\right)$. Therefore, the modal method should guaranty the required calculation accuracy of the particle velocity prediction, at the expense of increasing the decomposition terms up to a sufficient level, in an oscillating but converging manner.

From the above analyses, it can be surmised that a larger number of modes may improve the accuracy for particle velocity, but not necessarily in a monotonous manner. Owing to the oscillating feature of the convergence curve shown above, it is desirable then to find the suitable number of modes to be used, with which the prediction error can be locally minimal. On the other hand, it goes without saying that the so-called criterion shall also depend on the distance of the observation point from the vibrating plate. To further investigate this, ΔV is calculated for different z

coordinates, with results shown in Fig. 2.8. One can observe that, for all z values, all ΔV curves exhibit similar variation trend with respect to z, as described above. However, the convergence becomes increasingly slower as the observation point gets closer to the vibrating plate (when z gets smaller), along with a larger oscillation period. For the smallest z analyzed (z = 0.00625 m), for example, it requires 80 z-direction modes for ΔV to approach zero.

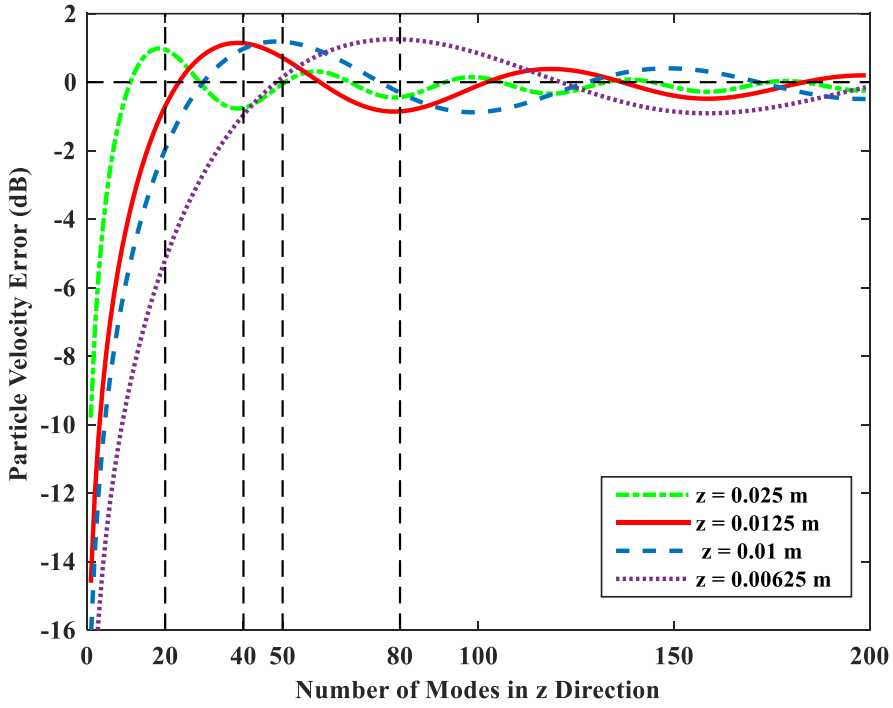

Figure 2.8 Velocity prediction error with respect to the number of modes in the z-direction

The oscillating nature of the convergence curves suggest that, for a given distance from the plate z, it should be possible to employ a small number of n_z terms to get the local minimum ΔV. The so-called truncation criterion, if exists, should depend on the relationship between the number of modes in the z-direction n_z and the coordinate z. To establish this relationship, a generalized mode number G is defined to connect the wavelength of the mode n_z, $\lambda_z = \frac{2L_z}{n_z}$, and the coordinate z of the observing point, as:

$$G = \frac{z}{\lambda_z/_2} = \frac{n_z z}{L_z} \tag{2.57}$$

Using this definition, different curves shown in Fig. 2.8 are normalized with respect to *G* and the results are shown in Fig. 2.9a. It is clear that the normalized curves show a highly consistent trend for all z values considered. One can observe that ΔV approaches local maximum values at every integer of *G* (1, 2, 3…). The first oscillation point starts at *G* = 1. Deriving from Eq. 10, this corresponds to z =1/2 λ_p, which is the half acoustic wavelength. The local minima of ΔV are obtained roughly at the middle of two extreme values, starting from *G* = 1.5, followed by 2.5, 3.5, etc. Taken the first minima as an example, *G* = 1.5 corresponds to z = 3/4 λ_z. Note that p is the highest mode index that is included in the calculation. Therefore, to minimize the accurate acoustic velocity prediction error, a rule of thumb would be to increase the number of acoustic modes in the z direction, until reaching the one with its 3/4 wavelength falling into z. In another word, for a given the distance from the vibrating plate, all the lower-order modes in the cavity depth direction whose 3/4 wavelength is larger than that distance should be used in the series decomposition to ensure a good prediction accuracy for the particle velocity.

Mindful of the possible dependence of the aforementioned on the frequency, the above proposed truncation criterion is checked for one of the plate resonances frequencies at 128 Hz, with results shown in Fig. 2.9b. Once again, the normalized ΔV curves show an identical variation trend as the previous non-resonance cases, which lead to exactly the same conclusions in terms of velocity convergence criterion. Nevertheless, it is found that the oscillation amplitude of the ΔV curves at the resonance frequency is somehow smaller than that of the non-resonance one. On all

accounts, the proposed criterion on oscillating convergence seems to apply to all frequencies.

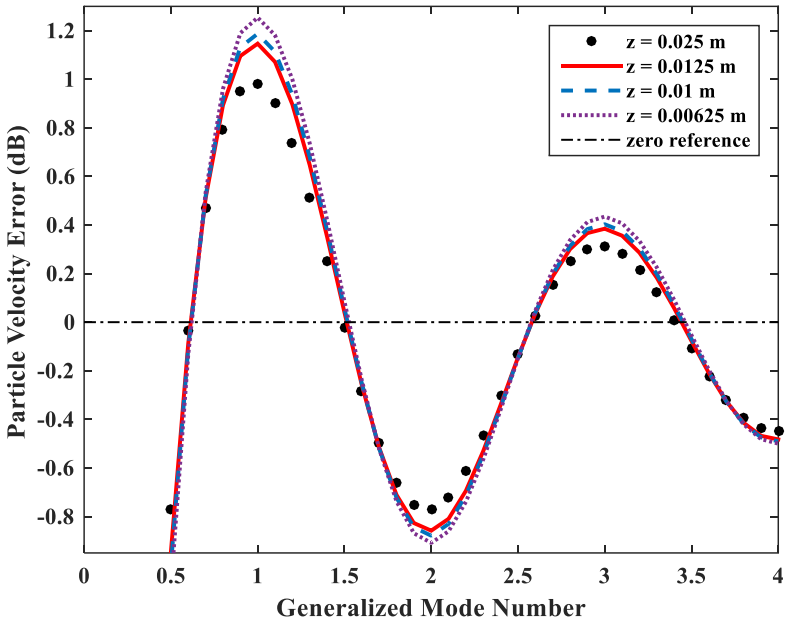

(a)

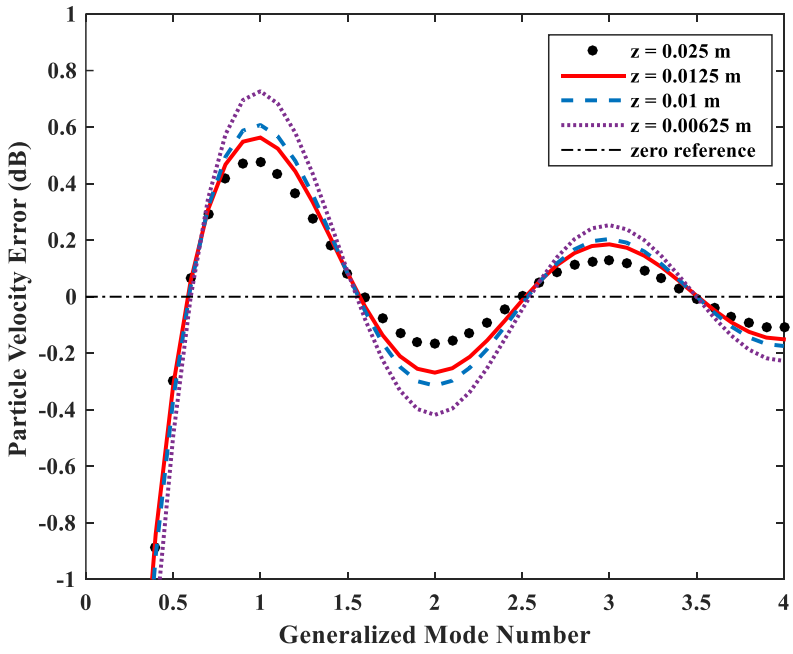

(b)

Figure 2.9 Velocity prediction error with respect to the generalized mode number G: (a) Uncoupled non-resonance frequency at 210 Hz; (b) Uncoupled resonance frequency at 128 Hz.

As a final check, Figure 2.10 compares the velocity prediction results using the proposed truncation criterion with G = 1.5 and the wave method in the 3-D configuration. According to Eq. 2.57, G = 1.5 results in 120 z-direction modes for z = 0.00625m in Figure 2.10a and 30 z-direction modes for z = 0.025m in Figure 2.10b. While according to the pressure criterion, the number of z-direction modes is 8 for both cases. The result obtained with the pressure criterion is also added for reference. It is worth recalling that, the use of only pressure criterion would not be enough to guaranty the velocity calculation, although the use of a larger number of modes is definitely helpful. The proposed velocity convergence criterion, however, results in significant improvement to the particle velocity prediction. Additionally, comparisons between Figure 2.10a and b also show that the proposed criterion holds well for different calculation point positions with different z coordinates.

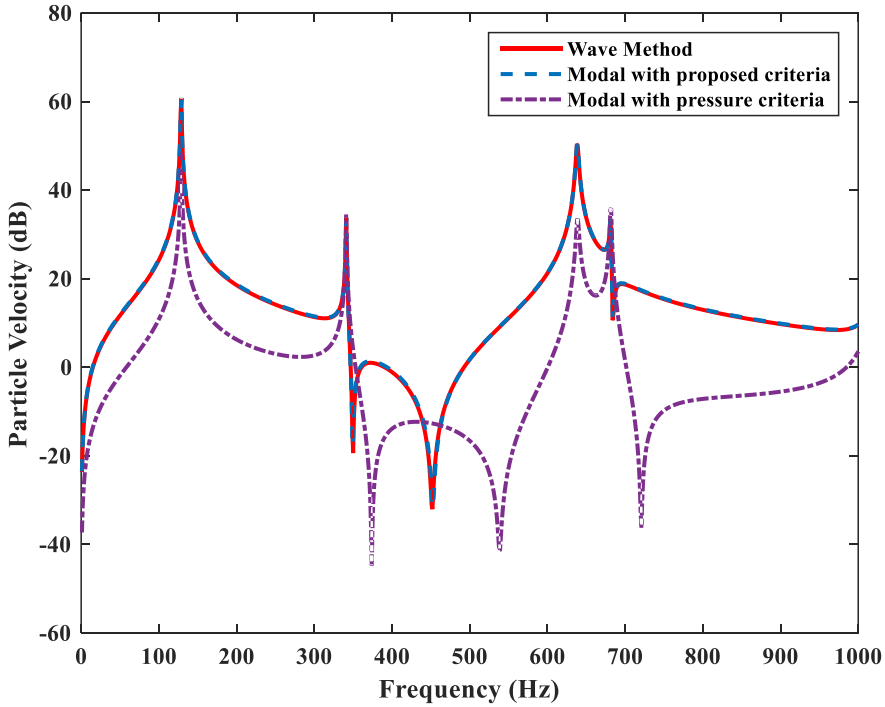

(a)

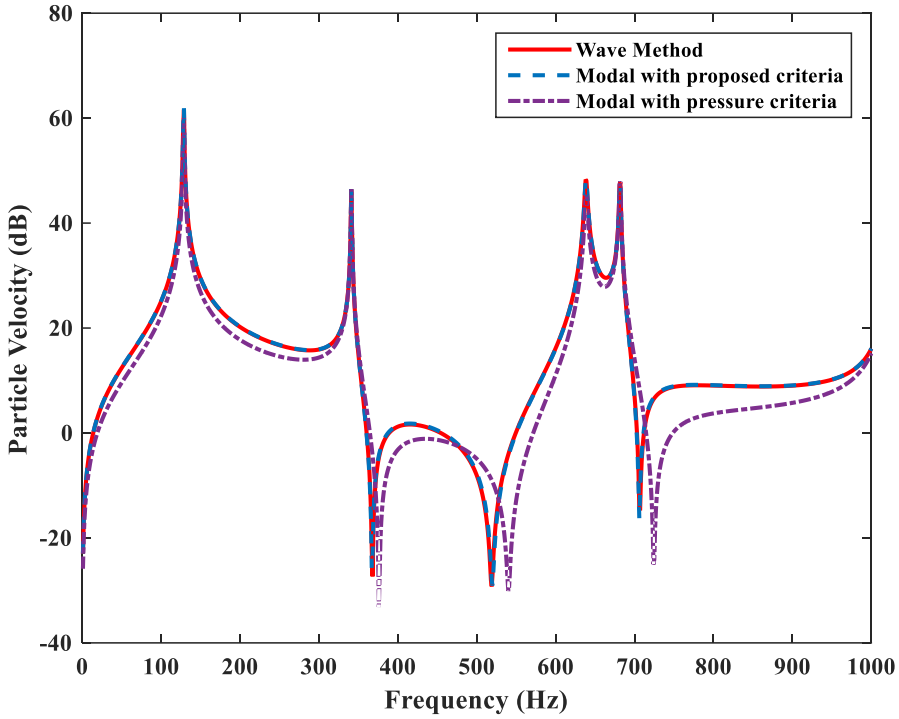

(b)

Figure 2.10 Particle velocity predictions: (a) z = 0.00625m; (b) z = 0.025m.

2.3 Summary

This Chapter firstly presents the theoretical models for a vibrating plate and an acoustic cavity with rigid walls. These two basic models will be used throughout the whole thesis as a benchmark. Then, two popular methods, the wave method, and the modal method, in plate-cavity system modeling are revisited. Differences between the two models are discussed. The wave method solves the problem by introducing new functions which can simultaneously describe the modal properties of the cavity and satisfy the boundary conditions over the plate-cavity interface, while the modal method solves the problem by using the uncoupled modal functions of each sub-system. Obviously, the wave method has a better performance but difficult to establish

the model while the modal method is easier to implement but encounters difficulties in dealing with the boundary convergence problems. Additionally, the selective modal matching pattern between the plate and the cavity is also analyzed and reviewed.

The existing controversy on the accuracy of the modal method has been clarified. It is found that the acoustic pressure prediction using modal method can be sufficiently accurate, throughout the cavity including vibrating interface as long as a sufficient number of cavity modes (approximately satisfied the double frequency principle) are used, in agreement with the common understanding reported in the literature. The pressure criterion, however, cannot guaranty the velocity prediction accuracy at the vicinity of the plate-cavity interface, due to the inherent weakness of the modal shape functions. Nevertheless, numerical studies reveal an oscillating convergence pattern of the particle velocity when the decomposition terms in the cavity depth direction increase. More specifically, for a given calculation point, the calculated particle velocity using modal approach first monotonously approaches to the exact value with a relatively small but increasing number of terms, overshoots and then converges to the exact solution in an oscillating manner, starting roughly from the generalized mode number $G = 1$. For a given distance from the vibrating plate, the modal series in the cavity depth direction should be truncated up to $G = 1.5, 2.5, 3.5\ldots$ etc. Explained using the series decomposition theories and verified in both 1D and 3D configurations, this so-called velocity truncation criterion suggests using all these lower-order modes in the cavity depth direction, whose 3/4 wavelengths are larger than the distance between the calculation point and the vibrating plate, to ensure a good prediction accuracy for the particle velocity. Therefore, when both the pressure criterion and the proposed velocity convergence rule are satisfied, a fast convergence of the particle velocity can be achieved.

CHAPTER 3 Condensed Transfer Function (CTF) Approach and Validations

In this chapter, the main CTF theory is presented. It shows how this method generalizes the previously proposed PTF approach into a more general framework. Examples are given to show that CTF allows obtaining the same results as PTF approach without dividing the coupling interface into patches or grids. The theory presented is then applied to a plate-cavity system, followed by validations using the reference solutions established in Chapter 2. The system configuration is chosen to be larger than that in the previous analyses due to the need of studying the convergence speed and modeling performance of different condensation functions at mid-to-high frequency range. This provides a fundamental basis to propose a mid-to-high frequency modeling method. By the same token, the larger configuration will also serve as a preparation for the DSF model to be studied in the later chapters.

3.1 CTF Approach

This section presents the basic theory of the CTF approach. After that, an application example based on the plate-cavity system is given to show how to build and assemble the matrices in the method. Then, three examples are presented that can be used as the condensation functions in the method.

3.1.1 Basic Theory

Consider a system composed of two sub-systems, of which the left one is either structural or acoustical, being excited and noted as the main sub-system (sub-system 1), and the right one is acoustical, noted as the attached sub-system (sub-system 2), coupled over an interface Γ as shown in Figure 3.1. In this Section, only the structural-acoustic interaction is focused. As for the coupling between two pure acoustic systems, it will be discussed in the next Chapter.

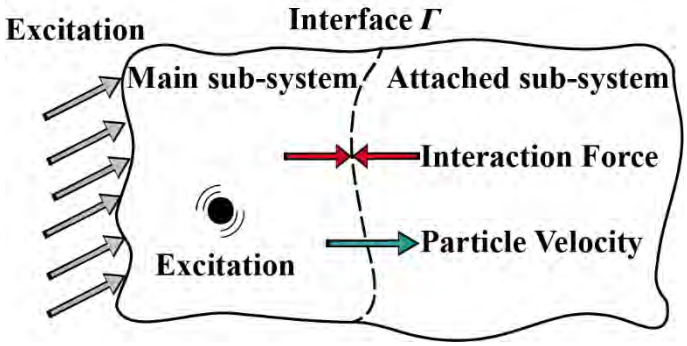

Figure 3.1 2D illustration of a system composed of two sub-systems that are coupled through an interface.

To simplify the analyses process, the whole system is assumed to be coordinate separable so that the physical quantities, such as velocities or forces, on Γ can be

described as $f(x,y)$. Therefore, the configuration shown in Figure 2.3 is modeled here to illustrate the CTF method. A set of $N_x \times N_y$ orthonormal functions $\{\varphi_{rs}\}_{1\le r\le N_x, 1\le s\le N_y}$, referred to as *Condensation Functions* (CF), is employed to approximate the velocities and the forces on the coupling interface Γ. Then the normal velocity and the normal force distribution on Γ for each subsystem can be decomposed as:

$$\begin{cases} U^{\alpha}(x,y) = \sum_{r,s} u_{rs}^{\alpha}\varphi_r(x)\varphi_s(y) \\ P^{\alpha}(x,y) = \sum_{r,s} p_{rs}^{\alpha}\varphi_r(x)\varphi_s(y) \end{cases} \quad 3.1$$

where $\alpha = 1$ or $\alpha = 2$ represents the sub-system number. Also, the external excitation P^e can be decomposed in the same way, as

$$P^e = \sum_{r,s} \tilde{p}_{rs}^{e}\varphi_r(x)\varphi_s(y) \quad 3.2$$

For the structural sub-system, the condensed mobility $Y_{rs,kl}$ between CFs φ_{rs} and φ_{kl} is defined and calculated as:

$$Y_{rs,kl} = \frac{<\bar{U}_{rs}, \varphi_{kl}>}{<P, \varphi_{rs}>} = <\bar{U}_{rs}, \varphi_{kl}>, \quad 3.3$$

in which $<f, g>$ is a scalar product defined as $\int_{\Omega} f(x,y)g^*(x,y)dS$ with g^* being the complex conjugate of g, and $\bar{U}_{rs}$ is the uncoupled normal velocity on Γ when the structural subsystem is subject to an external excitation $P = \varphi_{rs}$. Additionally, the uncoupled condensed free velocity $\tilde{u}_{rs}$ of the structural subsystem is defined by

$$\tilde{u}_{rs} = <\tilde{U}^1, \varphi_{rs}>, \quad 3.4$$

where $\widetilde{U}^1$ is the uncoupled velocity of the structural subsystem over Ω when only an external excitation exists. For the acoustic sub-system, the acoustic impedance is usually more preferred because the response is acoustic pressure rather than velocity. Thus, the condensed impedance is defined by imposing a prescribed velocity $U = \varphi_{rs}$ over Γ, as

$$Z_{kl,rs} = \frac{< \bar{P}_{kl}, \varphi_{rs} >}{< U, \varphi_{kl} >} =< \bar{P}_{kl}, \varphi_{rs} >, \tag{3.5}$$

where $\bar{P}_{kl}$ is the acoustic pressure response on Γ when the acoustical sub-system subjects to an excitation φ_{kl}. Notice the order of the subscript changes from (*rs*, *kl*) to (*kl*, *rs*) in Eq. 3.5.

On the other hand, the velocity continuity and force equilibrium over Γ between the two sub-systems gives

$$\begin{cases} U^1 = -U^2 \\ P^1 = P^2 \end{cases}. \tag{3.6}$$

Substitution of Eq. 3.1 into Eq. 3.6 gives

$$\begin{cases} \sum_{r,s} u_{rs}^1 \varphi_r(x)\varphi_s(y) = -\sum_{r,s} u_{rs}^2 \varphi_r(x)\varphi_s(y) \\ \sum_{r,s} p_{rs}^1 \varphi_r(x)\varphi_s(y) = \sum_{r,s} p_{rs}^2 \varphi_r(x)\varphi_s(y) \end{cases}. \tag{3.7}$$

Multiplying φ_{rs} to both sides of Eq. 3.7 and integrating over Γ, all non-*rs* terms turn out to be zero thanks to the orthogonal property of the selected function series. Then, the following relationship can be obtained:

$$\begin{cases} u_{rs}^1 = -u_{rs}^2 \\ p_{rs}^1 = p_{rs}^2 \end{cases}. \tag{3.8}$$

Then, the coupling equations between the two sub-systems can be written as:

$$\begin{cases} U^1 = \widetilde{U}^1 + YP^1 \\ U^2 = Z^{-1}P^2 \end{cases}. \tag{3.9}$$

Substituting of Eq. 3.6 into Eq. 3.9 and considering the superposition relationship

$$u_{rs}^1 = \tilde{u}_{rs}^1 + \sum_{k,l} Y_{rs,kl}\tilde{p}_{rs}^1, \tag{3.10}$$

the equations can be written into matrix form, the condensed velocity $U^C = U^1 = -U^2$ can be solved as

$$\mathbf{U}^C = [\mathbf{Y}^{-1} + \mathbf{Z}]^{-1}\mathbf{P}^e, \tag{3.11}$$

in which $\mathbf{U}^C$ is the condensed velocity vector, $\mathbf{Y}$ is the condensed mobility matrix of the vibrating plate, $\mathbf{Z}$ is the condensed impedance matrix of the acoustic cavity, and $\mathbf{P}^e$ is the external excitation vector written in the CF coordinate. It should be reiterated that the orthogonality property of the CFs is not necessary from a theoretical point of view. However, using the property leads to Eq. 3.8 and then to an equation system which can be written in a very succinct form. Moreover, it is not a restriction to consider this property as it is easy to orthogonalize a set of non-orthogonal functions with the well-known Gram-Schmidt procedure.

In the current plate-cavity configuration, $\mathbf{Y}$ and $\mathbf{Z}$ can be obtained using the modal expansion method and the analytical expression of the mode shapes of the plate (when simply-supported) and the cavity, respectively. Since these two quantities are both frequency independent, a database can be established beforehand for each sub-system. For more complex cases when the analytical mode shapes are unavailable, numerical tools like FEM can be employed. For the considered case, the condensed mobility of the plate is given by substitution of Eq. 3.3 into Eq. 2.5, as:

$$Y_{rs,kl}^{s} = i\omega \sum_{m} \frac{C_{rs,m} C_{kl,m}^{*}}{\mathrm{M}_m(\omega_m^2 - \omega^2)}, \tag{3.12}$$

where $C_{rs,m} = \int \varphi_{rs} \phi_m dS$ is the modal matching coefficient between the CF φ_{rs} and the *m*th plate mode shape. For the condensed impedance, it can be obtained by substituting Eq. 3.5 into Eq. 2.18 as

$$Z_{kl,rs}^{s} = -i\omega\rho_0 c^2 \sum_{n} \frac{C_{kl,\mathrm{n}} C_{rs,\mathrm{n}}^{*}}{\Lambda_n(\omega_n^2 - \omega^2)}, \tag{3.13}$$

where $C_{rs,m} = \int \varphi_{rs} \phi_n dS$ is the modal matching coefficient between the CF φ_{rs} and the *n*th cavity mode shape.

3.1.2 Choice of the condensation functions and convergence rules

This section presents three examples of the choice of condensation functions and their convergence rules. Obviously, the higher the frequency band to model, the more the functions needed. Basically, we truncate the function series in terms of the wavelength composition over the coupling interface. At least two functions are needed for the shortest wavelength.

1) Gate functions

The gate functions are defined as:

$$\varphi_{rs}(x,y) = \begin{cases} \frac{1}{\sqrt{L_{gx} L_{gy}}} & (r-1)L_{gx} \le x \le rL_{gx}, (s-1)L_{gy} \le y \le sL_{gy} \\ 0 & \text{elsewhere} \end{cases}, \tag{3.14}$$

where L_{gx} and L_{gy} are the lengths of the gate function and *r* and *s* are the gate indices in *x* and *y* directions, respectively. As illustrated in Figure 3.2, each

condensed mobility term $Y_{pq,rs}$ physically corresponds to the velocity response U_{pq} when a unit excitation P_{rs} is applied. When the gate functions are employed, the CTF method retreats to the PTF method as a special case. Owing to the intuitive and explicit physical meaning of the gate functions, the corresponding condensed mobility and impedance can be obtained using various calculation schemes, or even from experimental measurements.

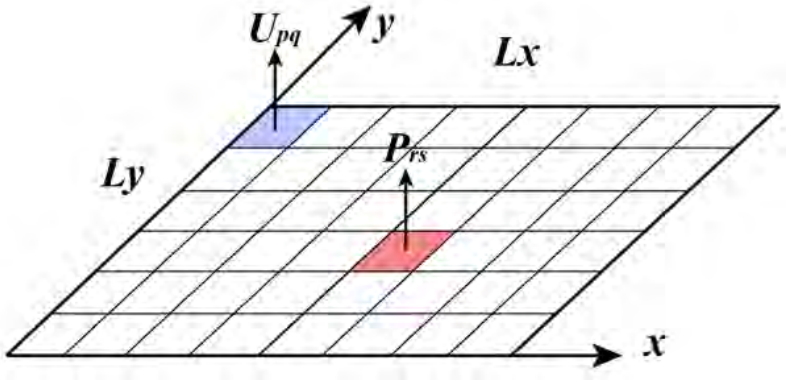

Figure 3.2 The working principle of gate functions

The convergence criterion for the PTF is well established [34], stipulating that at least two gate functions are needed to describe a wavelength, analogous to the spatial Shannon criterion used in signal processing. Therefore, for a given structural or acoustical wavelength λ, the length of the gate functions L_{gx} and L_{gy} should satisfy:

$$L_{gx} \leq \frac{\lambda}{2}, L_{gy} \leq \frac{\lambda}{2}. \tag{3.15}$$

2) The complex exponential functions

The complex exponential functions are given by

$$\varphi_{rs}(x,y) = \frac{1}{\sqrt{L_x L_y}} \exp(j\frac{2r\pi x}{L_x}) \exp(j\frac{2s\pi y}{L_y}). \tag{3.16}$$

in which $r \in [0, \pm1, \pm2, \ldots, \pm I_{max}^x]$ and $s \in [0, \pm1, \pm2, \ldots, \pm I_{max}^y]$ are the function indices in x and y directions, respectively. The plot of a 1-D complex exponential

function is shown in Figure 3.3. Different from the case of the gate functions in which the coupling interface is divided into more intuitive 'patches', the use of the exponential functions spatially decomposes the velocity and the force over the entire coupling interface. Similarly, we can write the convergence rule for the complex exponential functions as for gate functions, as

$$I_{max}^{x} \geq \frac{L_x}{\lambda} - \frac{1}{2}, I_{max}^{y} \geq \frac{L_y}{\lambda} - \frac{1}{2}. \tag{3.17}$$

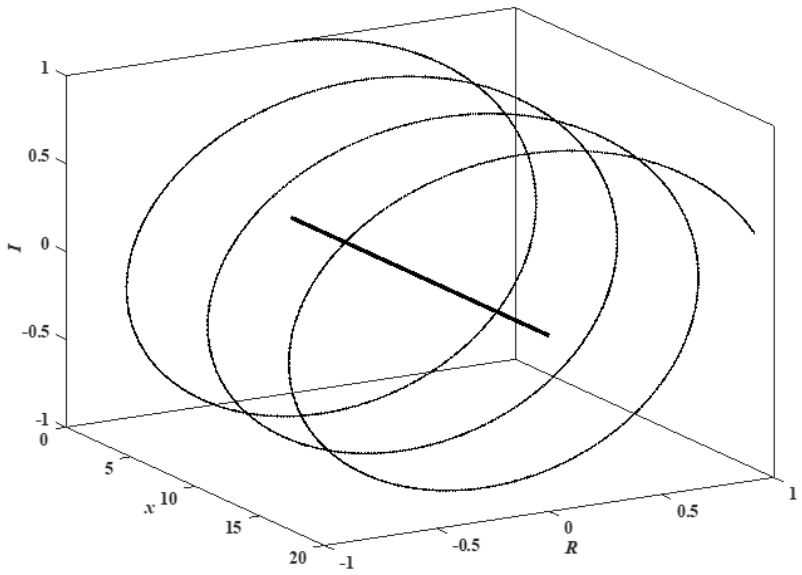

Figure 3.3 Plot of 1-D complex exponential function on the *x*-axis.

In the following chapters, people will find that the complex exponential functions play a very important role in this thesis. The wavy feature of the complex exponential functions could considerably increase the modeling efficiency within the mid-to-high frequency range.

3) The Chebyshev polynomials

As an intermediate choice between the discrete gate functions and the continuous complex exponential functions which well match the sine and cosine modal shapes, an orthogonal set of polynomials can satisfy the requirement of the condensation

functions as well. As has been used in literature, the Chebyshev polynomial is a representative one as tabulated in Table 3.1.

Table 3.1 The expressions of the Chebyshev polynomials

Terms	Expression
$Ch_0(s)$	1
$Ch_1(s)$	s
$Ch_{n+2}(s)$	$2sCh_{n+1}(s) - Ch_n(s)$

The plot of the first four orders is shown in Figure 3.4 for reference. Meyer [36] proposed that adding a weight function could reduce the numerical errors at the boundary and promise the orthonormal property as:

$$< f, g >= \frac{L}{\pi}\int_0^{L_x} f(s)g^*(s)\frac{1}{\sqrt{s(L-s)}}ds. \quad 3.18$$

Equation 3.18 is an equation for one direction. The equation for the two-dimensional interface can be obtained by assembling the two sets of functions. Similarly, the convergence rule for the Chebyshev polynomials are

$$n \geq \frac{2L_x}{\lambda} - 1, I_{max}^y \geq \frac{2L_y}{\lambda} - 1. \quad 3.19$$

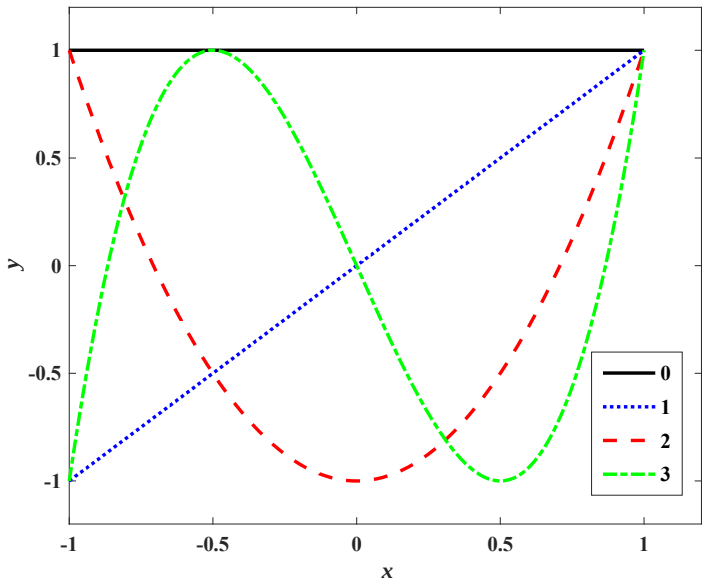

Figure 3.4 Plot of the Chebyshev Polynomials: The first four orders.

3.2 Numerical Validations of the CTF Approach in a Plate-Cavity System

3.2.1 Configurations and Preliminary Analyses

In the following numerical analyses, the dimension of the cavity is set to be 2.5m×2m×3m (x×y×z) to represent a small room. The plate is assumed to be simply-supported to facilitate model validation. The plate thickness is 18mm. The plate is made of glass and it has a Young's modulus 7.2×10^{10}Pa with a Poisson's ratio 0.2 and mass density 2.53×10^{3}kg/m^3. An oblique acoustic excitation with an amplitude of 20Pa impinges on the plate, with both the dihedral angle and the intersection angle with the x-axis being 45° (i.e. $\theta_1 = \theta_2 = 45°$ in Figure 2.4). The use of the oblique incident excitation ensures the excitation of more plate modes to get the complexity needed for the analyses. The frequency band of interest is [1, 1000] Hz. Additionally, the number of condensation functions should be determined by the shorter wavelength

among the subsystems. Because the number used for the two subsystems needs to be equal to be assembled together in Eq. 3.11, the number of functions to be used is then selected according to the subsystem whose wavelength at 1000Hz is shorter. In the present case, the shorter wavelength comes from the acoustic system with the smallest wavelength of 0.17m. This results in a minimum of 174 condensation functions. In the present case, 180 gate functions will be used (15 for x direction and 12 for y direction) in the calculation. For the complex exponential functions, the convergence rules impose $I_{max}^{x} = I_{max}^{y}$ =6, giving a total of 169 terms in the calculation. The maximum order used for the Chebyshev polynomials is 13 so that the total function number is also 169.

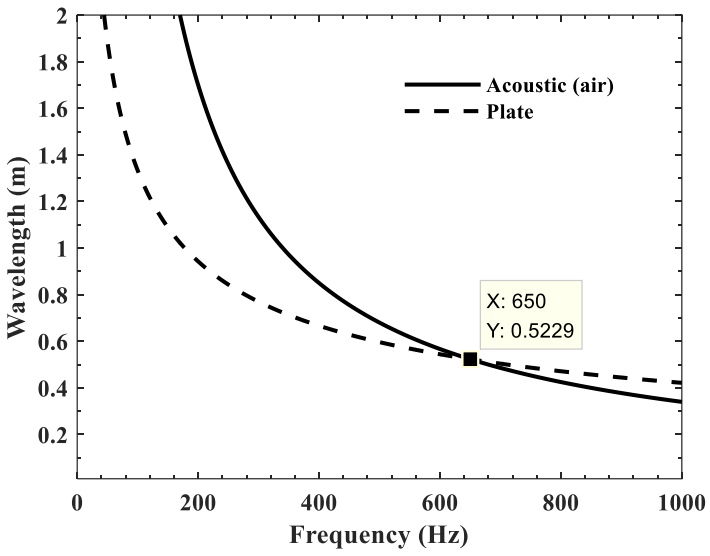

(a)

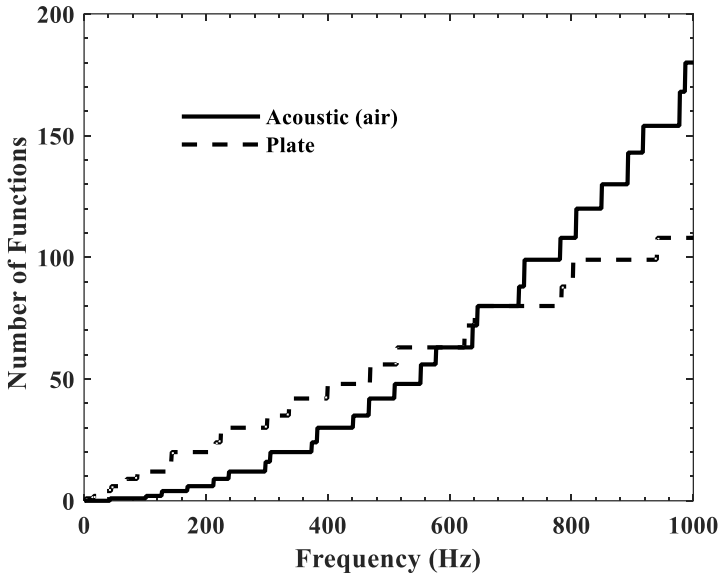

(b)

Figure 3.5 (a) Wavelength variation of the subsystems with respect to frequency and the system critical frequency; (b) The function number of the truncated series with respect to the maximum frequency

To better quantify the frequency range, we define the start of the so-called mid-frequency range when the modal overlap factor of either subsystem is close to one. To obtain the modal overlap factor, firstly we need to calculate the modal density of the subsystem. For a rectangular plate, the modal density $n_p(\omega)$of the bending wave is a constant, which is

$$n_p = \frac{L_x L_y}{4\pi} \sqrt[4]{\frac{\rho_p h}{D}} \tag{3.20}$$

As for the rectangular cavity, the acoustic modal density $n_c(\omega)$ can be written as

$$n_c(\omega) = \frac{V}{2\pi^2 c^3}\omega^2 + \frac{A}{8\pi^2 c^2}\omega + \frac{L}{16\pi c}, \tag{3.21}$$

where V is the volume of the cavity, A is the surface area of the cavity, and L is the summation of the edge length of the cavity. Apparently, the acoustic modal density is

highly dependent on frequency. At high frequencies, we can use the quadratic frequency term to approximate the acoustic modal density in most cavities. The total mode numbers can be obtained by integrating $n(\omega)$ within the given frequency bands, which is calculated for the present configuration and shown in Figure 3.6 for reference.

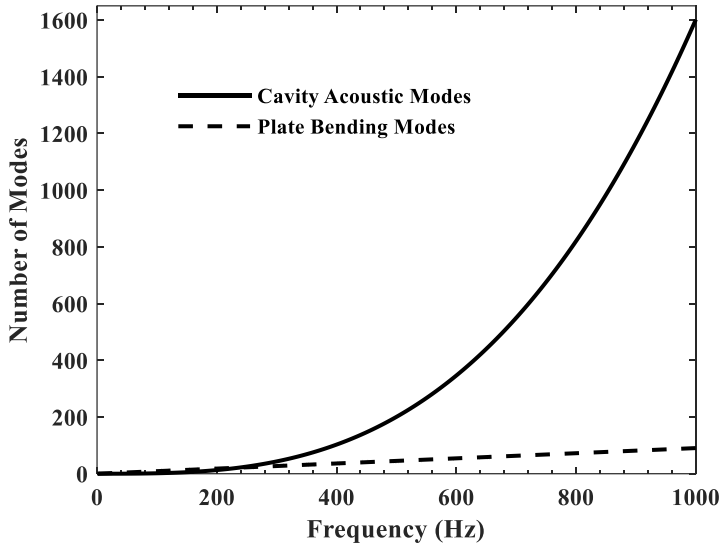

Figure 3.6 Mode number of the two sub-systems with respect to frequency.

Table 3.2 tabulates the number of modes and modal overlap factor in the one-third octave frequency bands. In the present case, the so-called mid-frequency domain begins at the one-third octave band with a center frequency of 500 Hz.

Table 3.2 Number of modes and modal overlap factor of the plate and the cavity in different one-third octave frequency bands

Center frequency of the 1/3 octave band (Hz)	Number of modes		Modal overlap factor	
	Plate	Cavity	Plate	Cavity
250	3	26	0.21	0.07
315	5	49	0.26	0.21
400	8	94	0.33	0.43

500	10	167	0.41	0.84
630	11	334	0.52	1.69
800	17	634	0.74	3.38
1000	19	1247	0.83	6.77

3.2.2 Theoretical Validations

Generally, the model validation can be made by considering a sound insulation problem shown in Figure 3.7 and comparing the SPL prediction results with the analytical solutions. Therefore, the sound pressure is calculated at an arbitrarily selected point within the enclosure (0.5, 1.3, 2)m. The calculated SPL is shown in Figure 3.7, where the results by three different CFs are compared with that by the wave method. It can be seen that the pressure predictions by all the three types of CFs agree well with the reference result in the low-frequency range. However, the performance in the higher frequency range varies in Figure 3.7, especially at the valleys of the curves where the system becomes less dynamic. The convergence value at the high-frequency peaks is also different for the three CFs. The complex exponential functions have the best performance out of the three. Anyway, it is not a big problem in terms of mid-to-high frequency modeling. Generally, the convergence rules in Eqs. 3.17, 3.18, and 3.19 ensure acceptable calculation accuracy for all the three types of CFs.

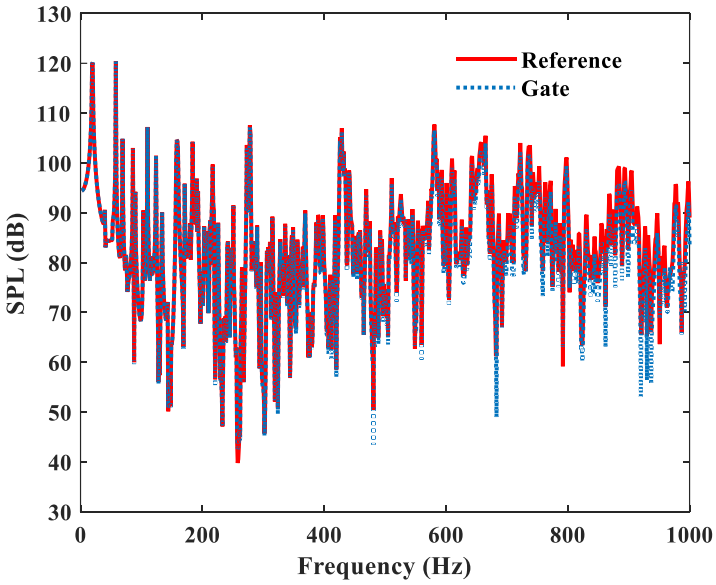
Reference
Gate
SPL (dB)
Frequency (Hz)
130
120
110
100
90
80
70
60
50
40
30
0
200
400
600
800
1000

(a)

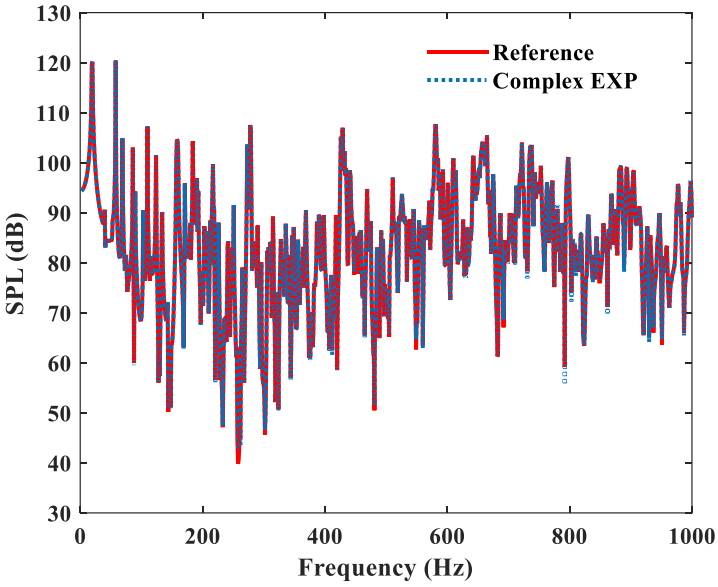
Reference
Complex EXP
SPL (dB)
Frequency (Hz)
130
120
110
100
90
80
70
60
50
40
30
0
200
400
600
800
1000

(b)

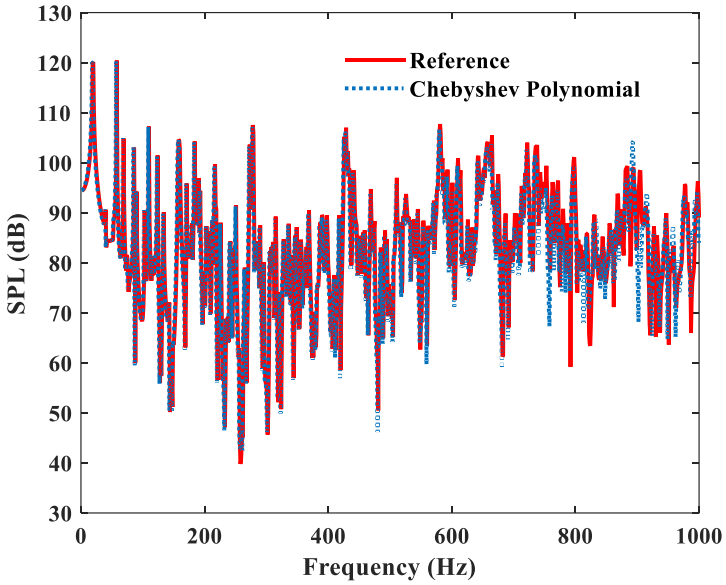

(c)

Figure 3.7 SPL predictions at a point (0.5, 1.3, 2)m: (a) Gate functions; (b) Complex exponential functions; (c) Chebyshev polynomials.

Figure 3.8 shows the volume averaged SPL results obtained from the three types of CFs. The same conclusions can be drawn as those for point prediction results. We can conclude that the general performance of the three types of CFs is ranked as complex exponential functions, Chebyshev polynomials, and gate functions.

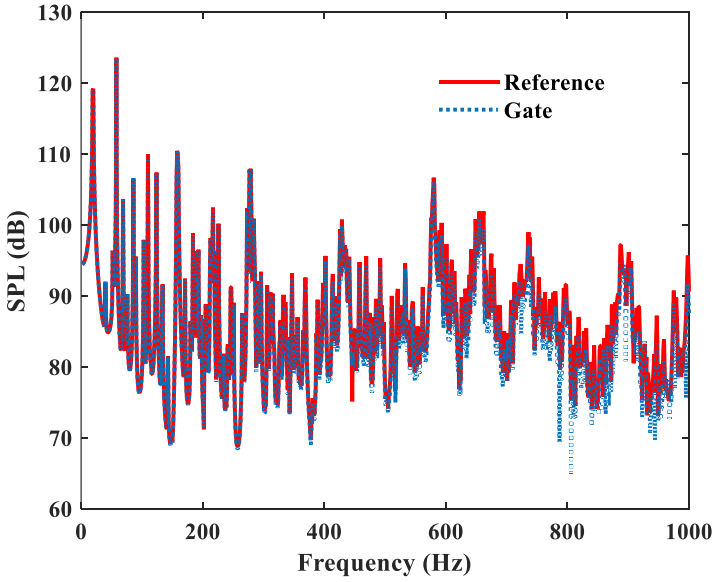

(a)

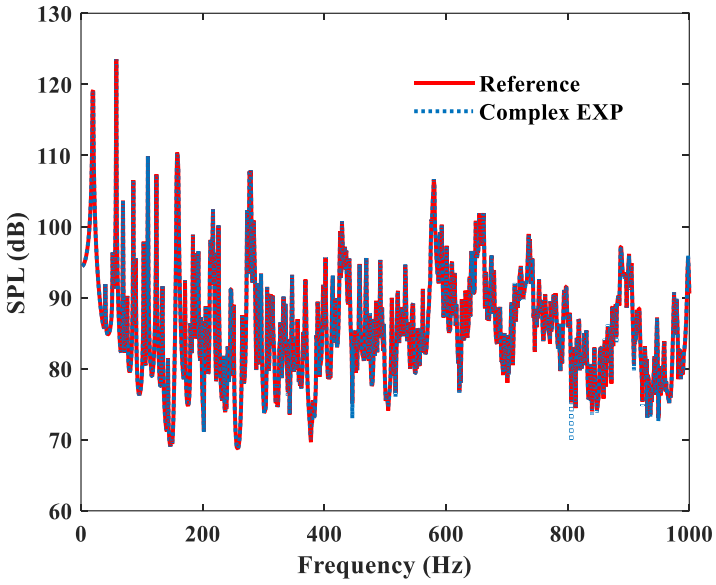

(b)

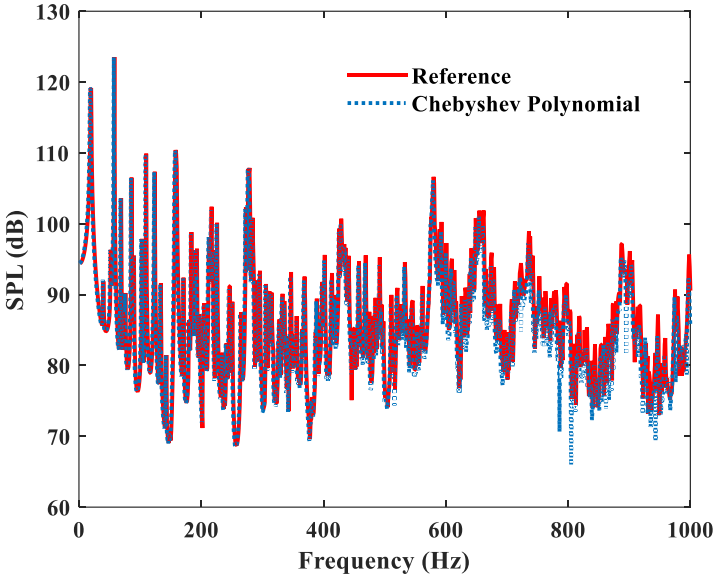

(c)

Figure 3.8 Volume averaged SPL predictions: (a) Gate functions; (b) Complex exponential functions; (c) Chebyshev polynomials.

One of the main advantages of the CTF method, which is also that of most deterministic methods, is the more detailed descriptions over the short-wavelength sub-system. For the present system, it is the vibrating plate below the critical frequency and the acoustic cavity above the critical frequency. Since more DoFs are

usually involved above the critical frequency, validations for detailed response prediction are made for the acoustic cavity above the critical frequency. The acoustic pressure field mappings at 800 Hz with the gate functions, complex exponential functions, and Chebyshev polynomials are shown in Figure 3.9a, b, and c, respectively. It can be observed that all the three function types can well predict the acoustic response of the cavity even if the target frequency is high. This validates the capability of the CTF method in terms of detailed response predictions.

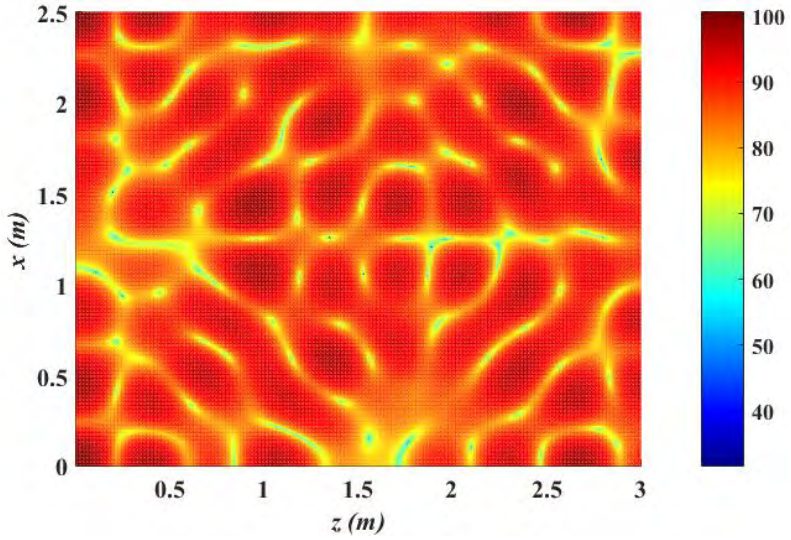

(a)

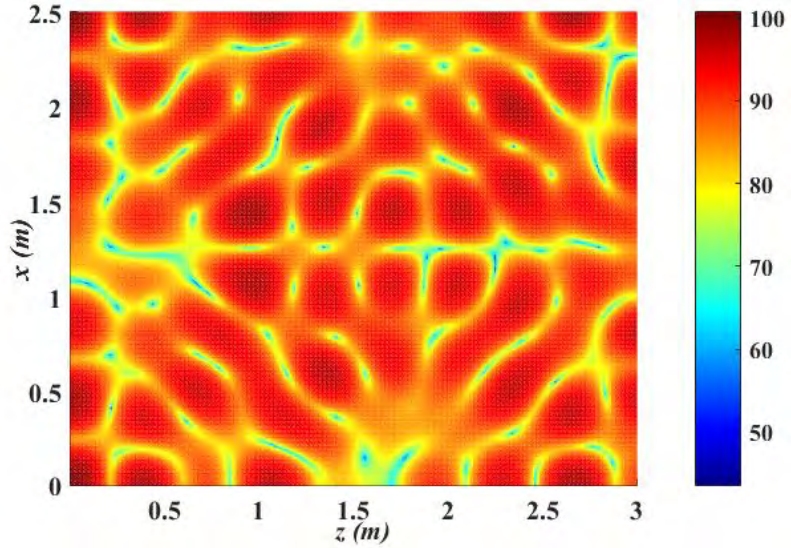

(b)

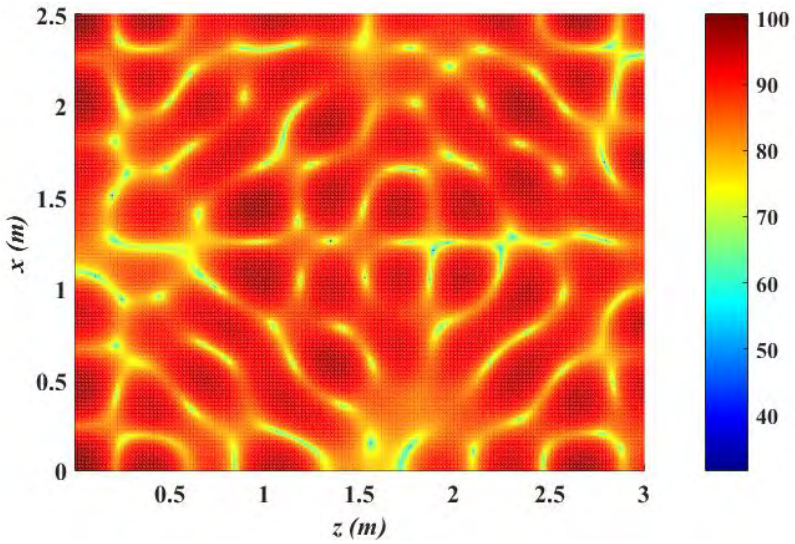

(c)

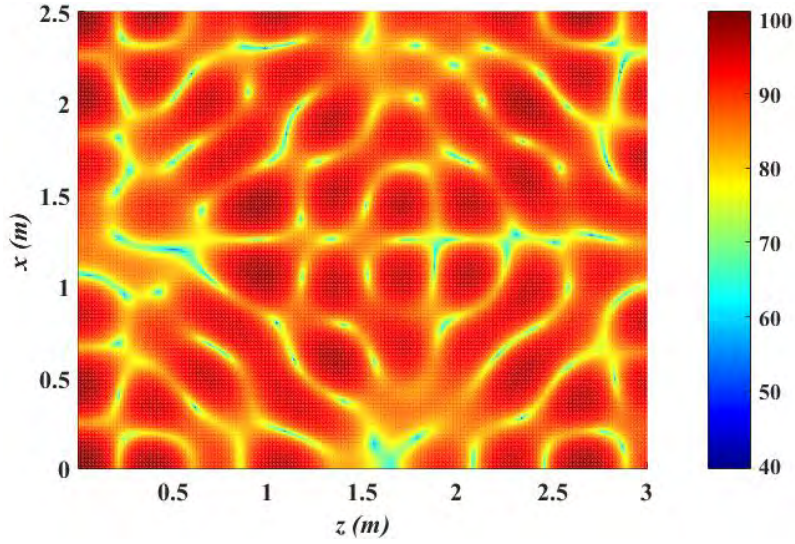

(d)

Figure 3.9 SPL field map: (a) Gate function; (b) Complex exponential function; (c) Chebyshev polynomial; (d) Modal method.

3.3 Conclusions

The basic theory of the CTF method is established in this chapter. The originally established line-coupled CTF method is extended and applied to the modeling of a surface-coupled benchmark vibro-acoustic system, comprising a panel and a cavity. Also, to serve as a tool in building acoustics, the model is also established when the cavity is partially covered by the vibrating plate. A full set of example is presented including how to assemble the coupling matrices and truncate the CF series in a surface coupling problem. Full validations are made on the CTF method by comparing with the reference solutions, when the gate functions, complex exponential functions, or Chebyshev polynomials are used. Calculation results are found to be similar, albeit small differences, between the three types of the CFs.

CHAPTER 4 Selection of the Condensation Functions and the Piecewise Computational Scheme

Based on the theoretical framework presented in the last Chapter, further simplification has to be made to increase the calculation efficiency of the method and to cope with the need of reaching a higher frequency range. This chapter aims at revealing the relationship between the function shapes of the CFs and the convergence speed in a given problem. It is found that the convergence speed can be significantly increased by matching the wavy feature of the CFs and that at the coupling interface. In light of this observation, a piecewise computational scheme is proposed to improve the calculation efficiency at a given frequency band. Numerical validations are made to verify the piecewise scheme.

4.1 The Influence of the CFs Types

In this section, we will analyze the three main variables, namely the condensed mobility, the condensed impedance, and the condensed velocity of the system, so as to reveal the underlying mechanisms and find a rule to simplify the mid-and-high frequency modeling. We concluded in the last section that the performance of the three types of CFs is ranked as complex exponential functions, Chebyshev polynomials. Meanwhile, the performance differences between the Chebyshev polynomials. and the gate functions are not significant. Therefore, only the complex exponential functions and the gate functions will be focused on in this section. In the following analyses, we will use the CF serial number *rs* on one or two axes in the figure. The *rs* are sorted as : $[\varphi_{11}, \varphi_{12}, \ldots\varphi_{1q}, \varphi_{21}, \varphi_{22},\ldots\varphi_{rs}]$, in which *r*, *s* = [1, 2,…] for the gate functions and *r*, *s* = [0, -1, 1, -2, 2…] for the exponential functions.

4.1.1 Condensed Mobility

Figure 4.1a shows the condensed mobility matrix obtained from the gate functions at 500 Hz. Because the gate functions are directly defined based on a small area on the interface, the values in Figure 4.1a can be considered as an approximation of the point mobility between each pair of "patches". The diagonal terms are the drive point mobility and the off-diagonal terms are the cross point mobility. Therefore, the pattern in Figure 4.1a is closely related to the modal properties at 500 Hz. It has little space for model simplification because we know that the modal properties are too complex to deal with at mid-to-high frequencies. One can verify in Figure 4.1b that more terms are involved at 800 Hz.

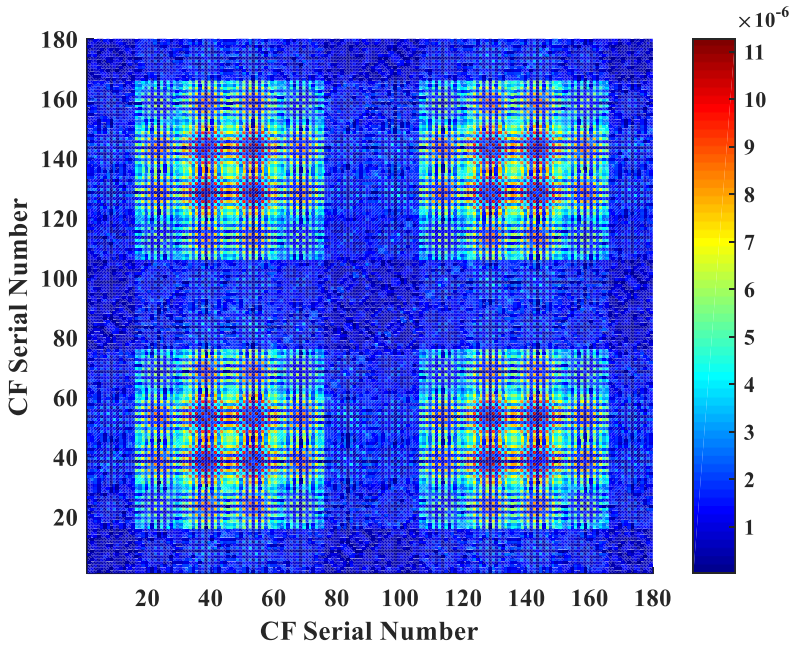

(a)

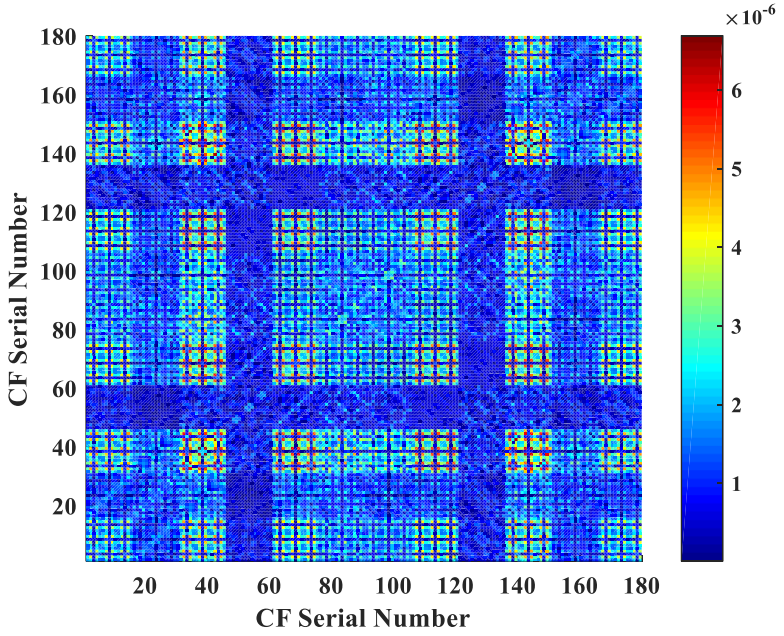

(b)

Figure 4.1 Condensed mobility obtained from the gate functions at: (a) 500 Hz; (b) 800 Hz. (Unit: $^{m^3}/_{N \cdot s}$)

Figure 4.2a shows the condensed mobility matrix obtained from the complex exponential functions at 500 Hz. It can be observed in that the condensed mobility terms of the exponential functions are much larger on the diagonal area than that on

the off-diagonal area. This phenomenon indicates that the condensed impedance terms of exponential functions are strongly coupled only with themselves and their conjugate functions. Other combinations (in the non-diagonal area) generate small values so that they can be removed in the calculations, which leave rooms for reducing the computation cost and getting approximations. One can verify this point by comparing the maximum value in Figure 4.2 to that in Figure 4.1. Notice that the results are obtained under the same configuration and frequencies. Figure 4.2b shows a similar diagonal dominated phenomenon for the condensed mobility matrix at 800 Hz. Additionally, we can find that more terms are involved at a higher frequency. Another point worth noticing is the color of the figure. If we observe the color of those bright "dots" in Figure 4.2, we can find $(\varphi_{\pm r\pm s}, \varphi_{\pm r\pm s})$ always have the same color. This implies that the dominated effect is closely related to the coefficient *rs*. Further analyses towards this point will be presented in later sections.

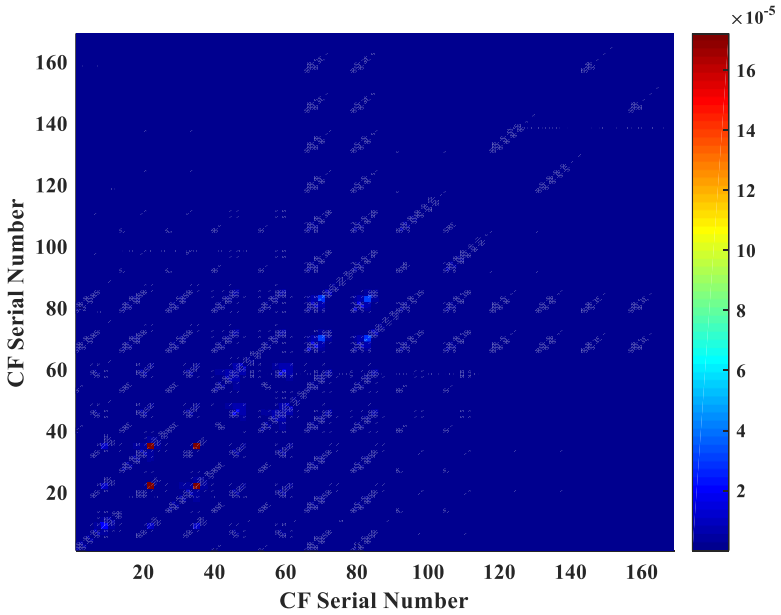

(a)

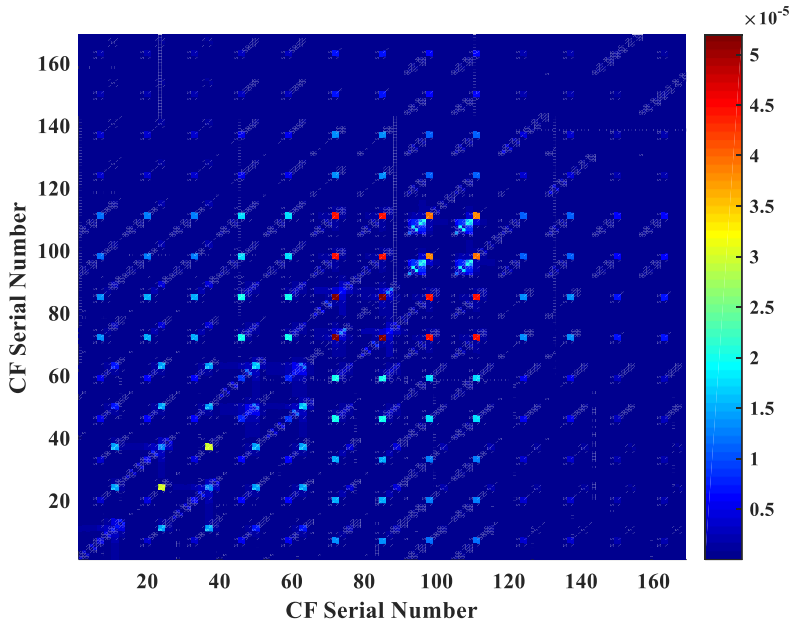

(b)

Figure 4.2 Condensed mobility obtained from the complex exponential functions at: (a) 500 Hz; (b) 800 Hz. (Unit: $^{m^3}/_{N \cdot s}$)

4.1.2 Condensed Impedance

Similarly, the condensed impedance for the acoustic cavity is analyzed for both the gate functions and the complex exponential functions. Figure 4.3 shows the condensed impedance matrix obtained from the complex exponential functions at 500 Hz and 800 Hz. The same conclusion can be drawn as those for Figure 4.1, the condensed mobility matrix obtained from the gate functions. One different point is, if we compare the influence of frequency on gate functions, it can be found the condensed cavity impedance varies more as the frequency increases. The spatial distribution in Figure 4.3b is hardly distinguishable while it is still clear in Figure 4.2b. This can be explained by the number of modes involved increases much faster for the cavity than that for the plate, as shown in Figure 3.6.

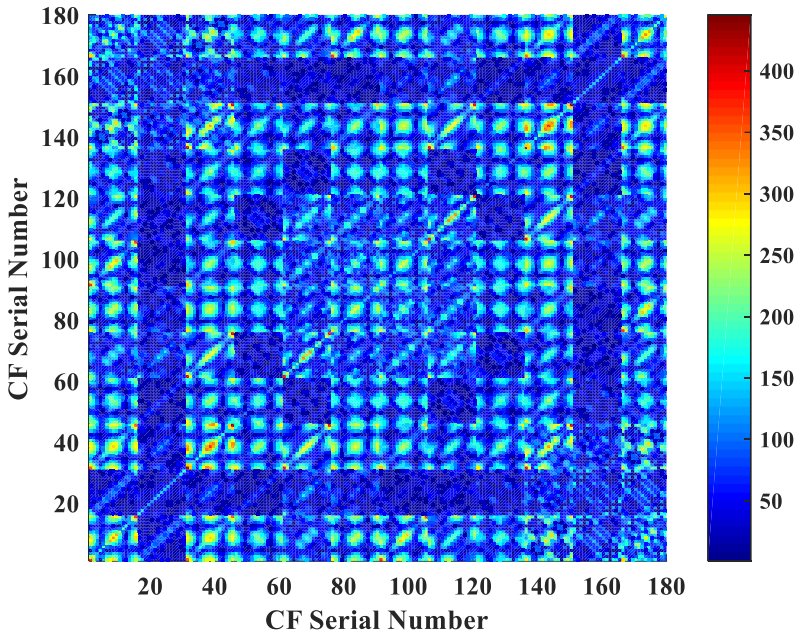

(a)

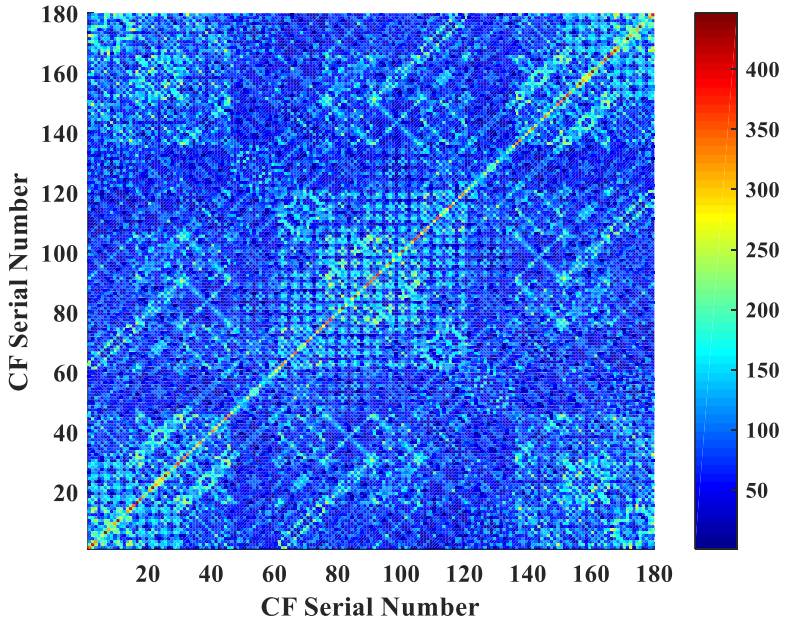

(b)

Figure 4.3 Condensed impedance obtained from the gate functions at: (a) 500 Hz; (b) 800 Hz. (Unit: $^{N \cdot s}/_{m^3}$)

For the condensed impedance matrix obtained from the complex exponential functions, we observe the same phenomena as in the condensed mobility matrix. Only a few dominated terms are existed closed to the diagonal region. It can be observed in

Figure 4.4a that most values in the matrix are less than 200 while the largest value is nearly 4000. However, for the gate function impedance matrix, these two values are 100 and 450. Another interesting point is the result in Figure 4.4b is not that obscure as in Figure 4.3b for the large number of acoustic modes involved.

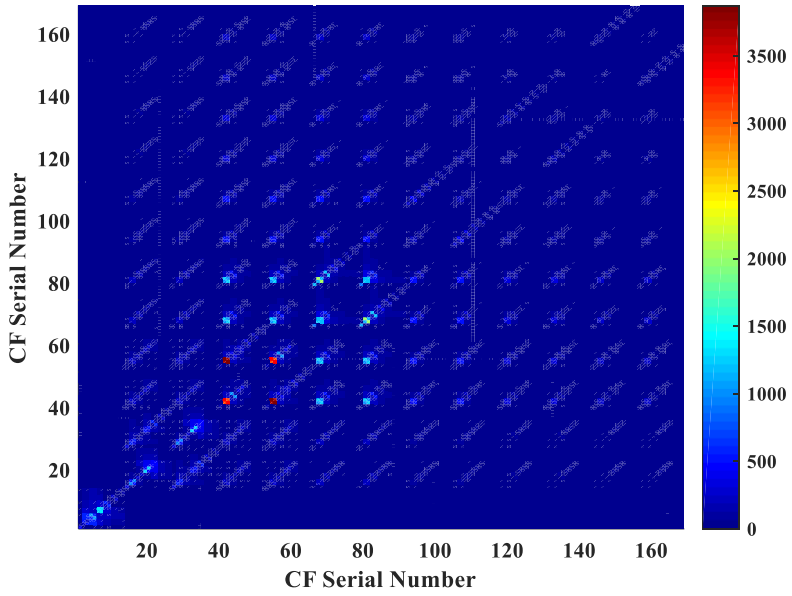

(a)

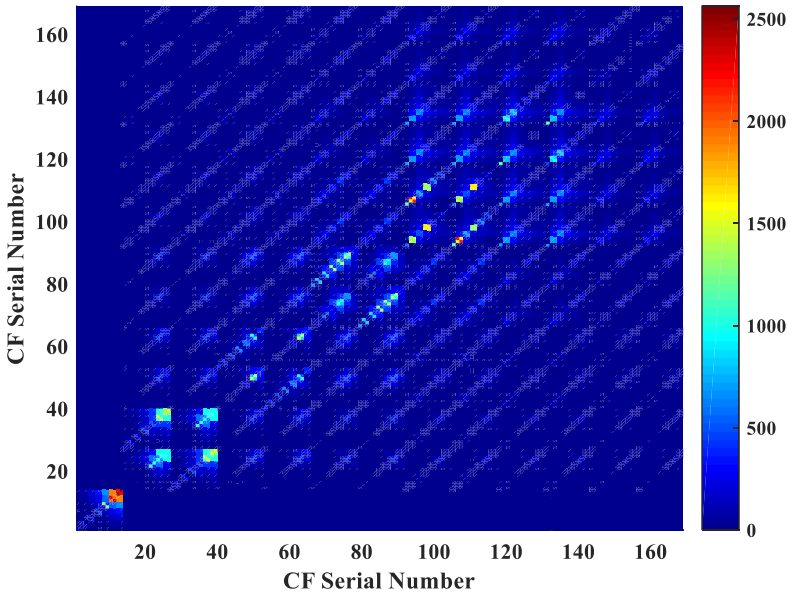

(b)

Figure 4.4 Condensed impedance obtained from the complex exponential functions at: (a) 500Hz; (b) 800Hz. (Unit: $N \cdot s/m^3$)

4.1.3 Condensed Velocity

The coupled velocity $U(x, y) = \sum_{r,s} u_{rs}\varphi_{rs}(x, y)$ on the interface is analyzed in this section. u_{rs} represents the contribution from the particular CF term φ_{rs} to the coupled interface velocity and they are shown in Figure 4.5 for the complex exponential functions and the gate functions, respectively. u_{rs} is plotted in log scale as $\log_{10}|u_{rs}|$.

It can be seen from Figure 4.5a that, for the complex exponential functions and for each frequency, there always exist some dominant terms holding a higher weight than the others, which are consistent with the behavior of the condensed impedance and the condensed mobility. It can then be surmised that the coupling velocity, which is the key parameter connecting the coupled subsystems, might be estimated by using a small number of CF terms if one knows how to choose them. Additionally, these dominant terms change as the frequency varies. As to the gate functions in Figure 4.5b, at any given frequency, the contributions from different terms are rather uniform, showing no particular dominant pattern. This can be explained by the mathematical properties of the gate functions. Indeed, as opposed to the continuous and wavy feature of the complex exponential functions, gate functions show discontinuities in their spatial distribution. As a result, it is naturally more difficult to map the waveform of the velocity over the interface, unless an increasing number of terms are used. For the complex exponential functions, however, the calculation efficiency could be greatly

increased if only dominating terms can be extracted within a frequency band. This will be further exploited hereafter.

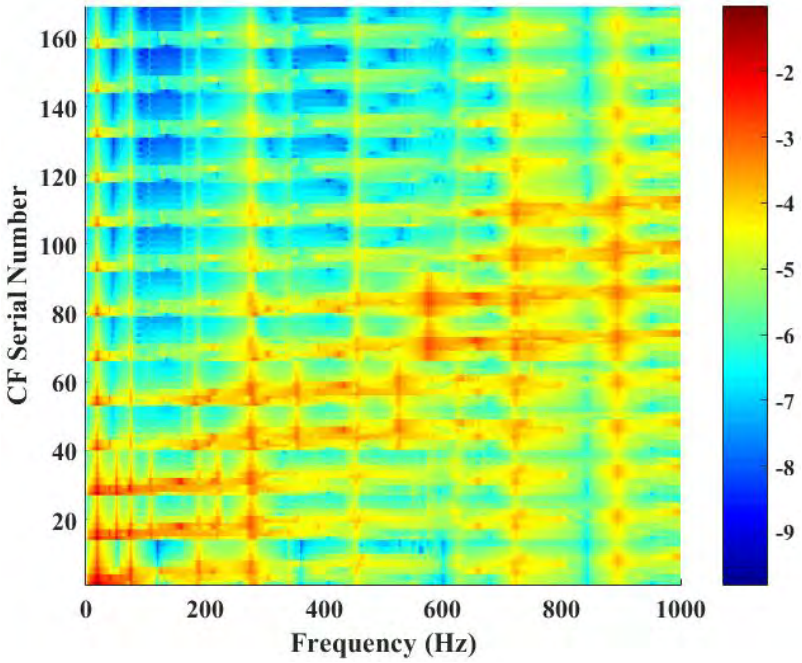

(a)

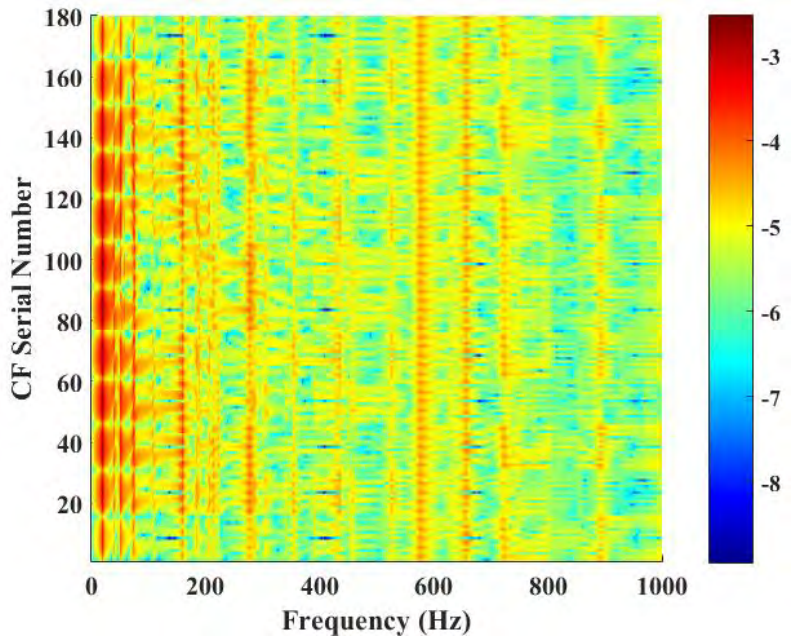

(b)

Figure 4.5 Condensed velocity contribution within the frequency band [1, 1000]Hz: (a) Gate functions; (b) Complex exponential functions.

4.2 The Piecewise Computational Scheme

This section presents the piecewise computational scheme. Based on the previous analyses, it is found that the complex exponential functions have more dominated terms in mid-to-high frequencies while the gate functions are more distributed. This section aims at extracting those dominated terms in the complex exponential function series so as to achieve similar performance with only a few terms.

4.2.1 Preliminary Analyses

To find the distribution rules of those dominated terms with respect to the complex exponential functions, firstly we define its function wavelength as:

$$\lambda_{c,rs} = \frac{2\pi}{\sqrt{\left(\frac{2r\pi}{L_x}\right)^2 + \left(\frac{2s\pi}{L_y}\right)^2}}. \tag{4.1}$$

Based on Eq. 4.1, we can rearrange the *y*-axis in Figure 4.5a with respect to the wavelength of each function, from short to long, as shown in Figure 4.6a. It can be found in Figure 4.6a that the dominated terms become more concentrated.

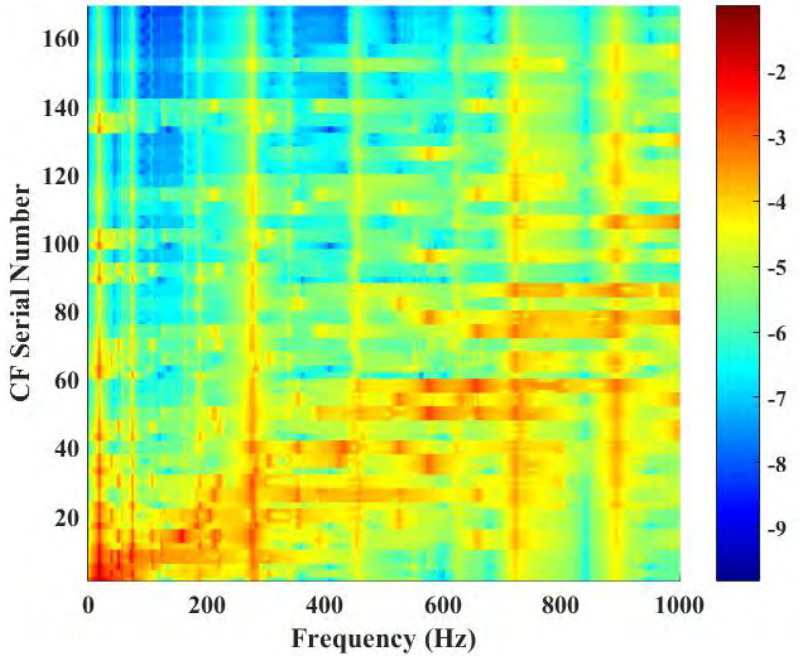

(a)

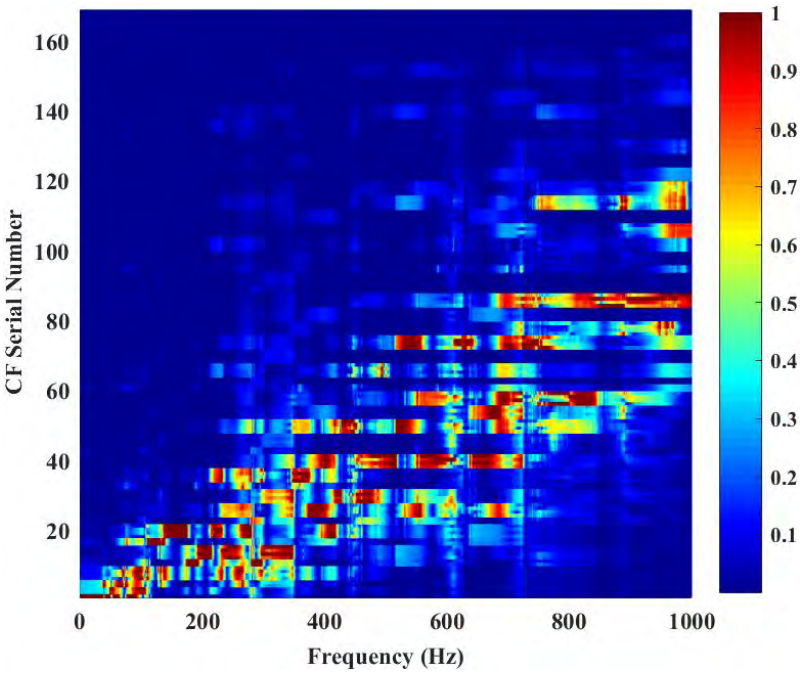

(b)

Figure 4.6 Condensed velocity contribution within the frequency band [1, 1000]Hz, the serial of the complex exponential functions on the *y*-axis are sorted by the function wavelength: (a) log scale plot; (b) For each frequency, normalized with respect to the maximum value in normal scale.

Two generalized wavelengths λ_{ca} and λ_{cs} are defined to connect the condensation functions with the acoustic cavity and vibrating structural, respectively, as:

$$\lambda_{ca} = \frac{\lambda_{c,rs}}{\lambda_a}, \qquad \lambda_{cs} = \frac{\lambda_{c,rs}}{\lambda_s}, \tag{4.2}$$

where λ_a and λ_s are the acoustic wavelength and structural wavelength, respectively, which are frequency dependent. They can be solved as a function of frequency *f* as:

$$\lambda_a = \frac{c}{f}, \qquad \lambda_s = \frac{\sqrt{2}\pi}{(f^2\rho_s h/D)^{1/4}}, \tag{4.3}$$

For convenience, those acoustic modes with λ_{ca} smaller than one are referred to as the inertia dominated modes, otherwise, they are called stiffness dominated modes [9]. The same rule also applies to structural modes characterized by λ_{cs}. Using the definition, λ_{ca} and λ_{cs} at 250Hz, 650Hz, and 800Hz are calculated for the complex exponential functions used in the last section and shown in Figure 4.7a, b, and c, respectively. Note that 650Hz is the critical frequency of the panel. In these figures, the *y*-axis is the $|u_{rs}|$ from each condensation function normalized with respect to the largest value of $|u_{rs}|$. Figure 4.7b and c have two *x*-axes, with λ_{cs} on the bottom and λ_{ca} on the top, both being arranged in an increasing order. The sequence of the condensation functions remains the same for the two *x*-axes, because $\lambda_{c,pq}$ is frequency independent and both λ_a and λ_s are fixed numbers for any given frequency. Figure 4.7b has only one *x*-axis since $\lambda_{ca} = \lambda_{cs}$ at the critical frequency.

In Figure 4.7a, two reference dash lines are plotted at λ_{ca}=1 and λ_{cs}=1 for the ease of analyses. It can be seen that most of the dominating terms are located around the two reference lines and more on their right side than the left side, which means a

more predominant contribution from the inertia modes than the stiffness modes. Comparing the three sub-figures in Figure 4.7, it can be seen that this phenomenon occurs at all the three frequencies being analyzed. In Figure 4.7c, more inertia terms are involved when the frequency increases, while the stiffness terms still have little contribution. Particularly in Figure 4.7b, the coupling is strongly dominated by the four terms close to $\lambda_{ca} = \lambda_{cs} = 1$, *i.e.* $\varphi_{\pm 3,\pm 3}(x, y)$ with a function wavelength of 0.521m, as compared with the critical wavelength of the system of 0.523m. This shows that the two subsystems strongly interact at the critical frequency and this strong coupling can be characterized by a very small number of condensation functions with close wavelengths.

Another noteworthy phenomenon is the location of the term which has the largest contribution. It is closer to λ_{ca}=1 at the lower frequency (Figure 4.7a) but much closer to λ_{cs}=1 at the higher frequency (Figure 4.7c). This is because 250Hz (Figure 4.7a) is before the critical frequency in which the acoustic wavelength is larger than that of the panel. Therefore, the acoustic cavity is a large wavelength subsystem, contrary to the supersonic case of 800Hz (Figure 4.7c).

Generally speaking, it can be concluded that, at any prescribed frequency and within a band, those CF terms which feature a better spatial wavelength match with the system would dominate the system responses. This explains why complex exponential functions outperform the gate functions in terms of both accuracy and efficiency. It can be surmised that there could be other function sets which are more efficient to model a system if the function wave of which match the structure wave characteristics. For example in an acoustic-black-hole structure, one may use wavelet to achieve a better modeling efficiency [162]. However, it is beyond the scope of this paper and will be explored in future works.

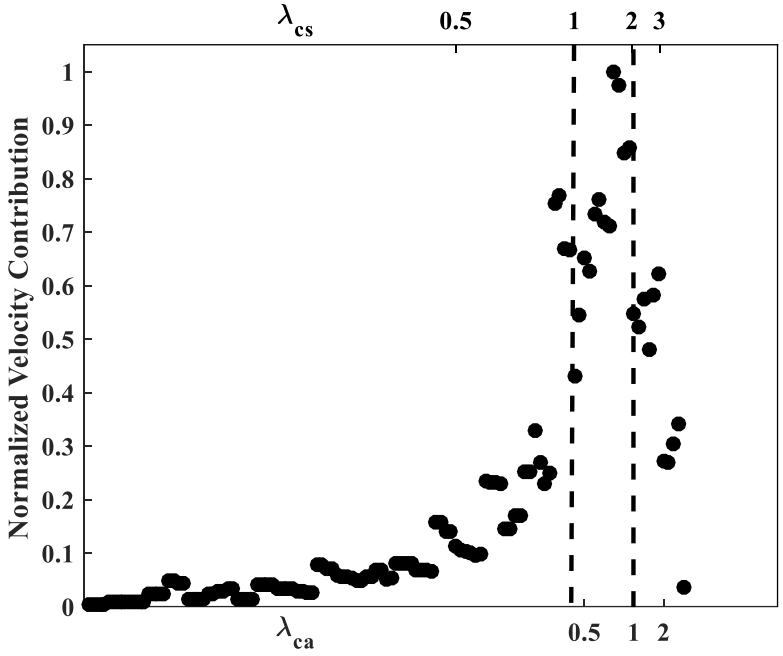
λ_{cs}
0.5
1
2
3
Normalized Velocity Contribution
0
0.1
0.2
0.3
0.4
0.5
0.6
0.7
0.8
0.9
1
λ_{ca}
0.5
1
2

(a)

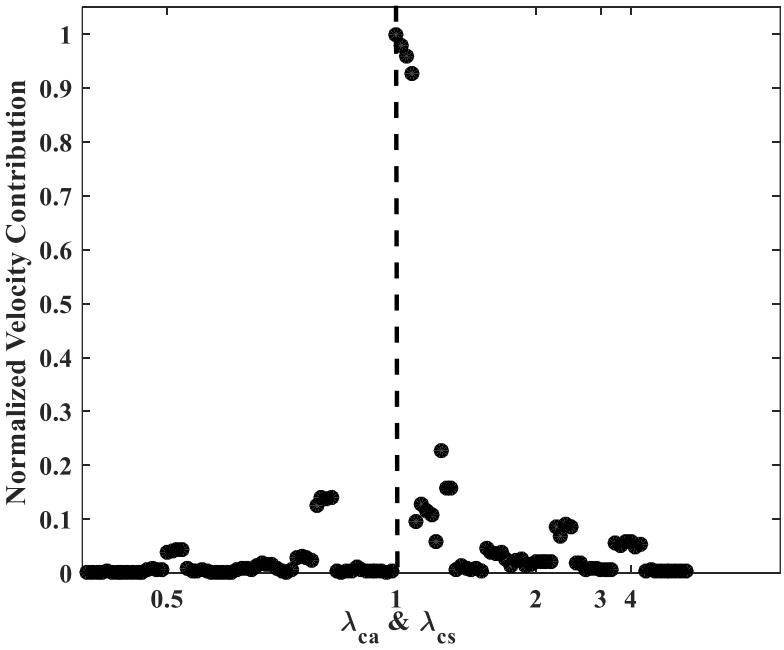
Normalized Velocity Contribution
0
0.1
0.2
0.3
0.4
0.5
0.6
0.7
0.8
0.9
1
0.5
1
2
3
4
λ_{ca} & λ_{cs}

(b)

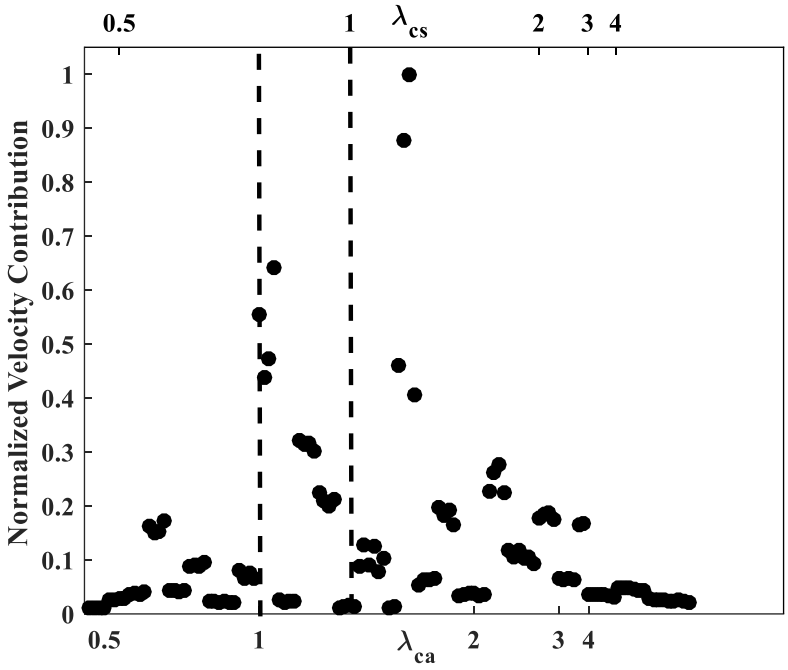

Figure 4.7 Normalized velocity contribution from each complex exponential function, arranged as a function of λ_{ca} and λ_{cs}: (a) 250Hz; (b) 650Hz (critical frequency) (c) 800Hz.

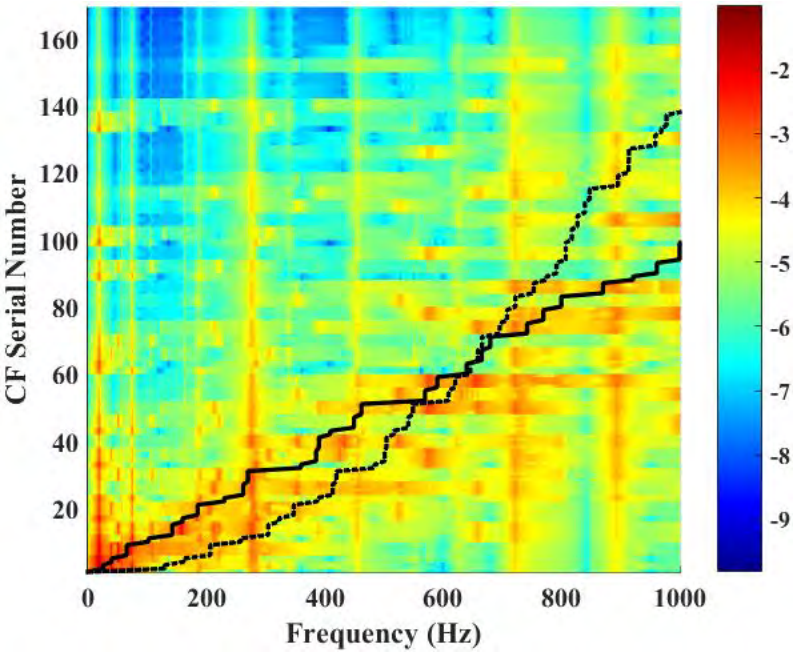

Figure 4.8 Condensed velocity contribution from each CF. The real line and the dotted line are corresponding to $\lambda_{cs} = 1$ and $\lambda_{ca} = 1$, respectively.

4.2.2 The Piecewise Computational Scheme

Before moving forward to the detailed selection criterion, an error quantification can be introduced to evaluate the ability of the CFs to map the velocity field on the coupling surface. An error index is defined for the frequency band $[\omega_1, \omega_2]$ as $20\log_{10} E_{rs}$ where

$$E_{rs} = \frac{1}{L_x L_y \Delta\omega} \int\int\int \left[u_c(x,y,\omega) - \sum_{r,s} u_{rs}(\omega)\varphi_{rs}(x,y) \right]^2 dxdyd\omega, \qquad 4.4$$

in which u_c is the plate velocity obtained from the reference method, i.e. wave approach [163]. Generally, larger *r* and *s* could lead to a smaller error but a reduced calculation efficiency.

For a frequency band $[f_l, f_h]$, the corresponding wavelength range of the coupled system is denoted by $[\lambda_h, \lambda_l]$. Three representative scenarios, corresponding to before critical, critical and after critical bands, are listed in Table 4.1 and analyzed.

Table 4.1 System critical frequency and the wavelength selection

Frequency band property	Frequency band	Wavelength selection
below critical	$f_l < f_c$ Hz, $f_h < f_c$ Hz	$\lambda_l = \lambda_a, \lambda_h = \lambda_s$
critical	$f_l < f_c$ Hz, $f_h > f_c$ Hz	$\lambda_l = \lambda_a, \lambda_h = \lambda_a$
above critical	$f_l > f_c$ Hz, $f_h > f_c$ Hz	$\lambda_l = \lambda_s, \lambda_h = \lambda_a$

Firstly, the selection criterion should include all dominating terms close to $\lambda_{ca} = 1$ and $\lambda_{cs} = 1$ for all frequencies within the band. That is to say, the wavelengths of the selected exponential functions should cover all the existing wavelengths of the

coupled system within the frequency band. Furthermore, as indicated in the previous sub-section, the inertia modes impose a larger weight on the response than the short-wavelength terms do. Therefore, more long-wavelength terms should be preserved in the calculation.

Assuming all the condensation functions that should be kept in the calculation have a function wavelength $\lambda_{c,rs}$ to satisfy $\alpha\lambda_h < \lambda_{c,rs} < \beta\lambda_l$, then the coefficient α and β is delimited by $0 \leq \alpha \leq 1$ and $\beta \geq 1$, respectively. Apparently, a smaller α or a larger β increases the size of the series sub-set, thus providing a better calculation accuracy but a reduced efficiency. In particular, when α=1 and $\beta \to \infty$, the criterion coincides with the traditional convergence rule. Therefore, the dominating terms should be extracted by properly selecting β. Figure 7 shows the calculation errors, which are obtained from Eq. 4.4, for three different one-third octave frequency bands with the center frequencies of 630Hz, 800Hz, and 1000Hz, respectively. It can be found that the error drops as the value of β increases and the drop speed slows down from β =1.5 onwards. Particularly, the error for the 630Hz band is small even for the low value of β. The reason is that the 630Hz band contains the critical frequency and its wavelength variation is relatively not significant so that the response expression is dominated by on a few terms, which is consistence with the result shown in Fig. 6b. Generally speaking, β =1.5 seems to be a good compromise between the accuracy and the calculation efficiency.

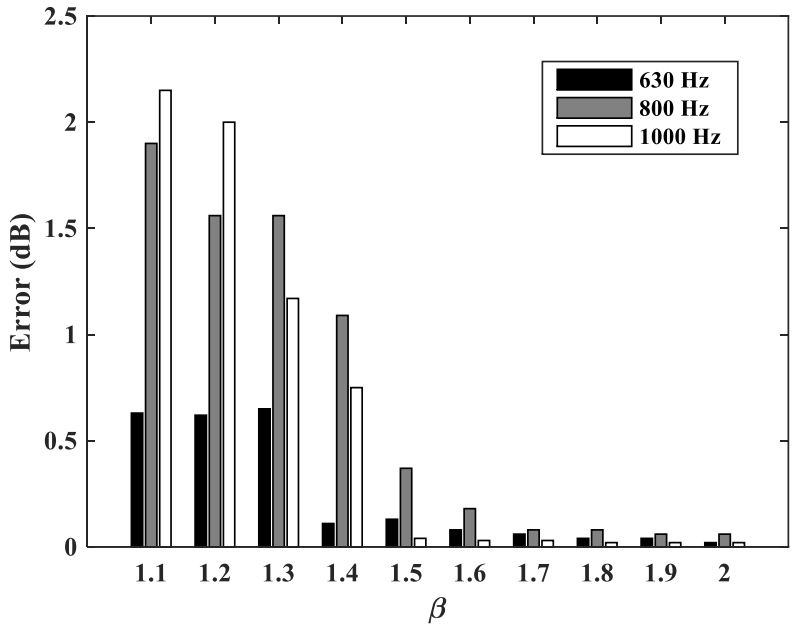

Figure 4.9 CTF calculation error for different β values within one-third octave bands centered at: 630Hz, 800Hz, and 1000Hz.

4.2.3 Numerical Validations for the Piecewise Scheme

The proposed selection criterion is applied to calculate the overall pressure response of the cavity within the one-third octave band with a center frequency of 630Hz, with the results shown in Figure 4.10 using β=1.5. It can be observed that the system responses at the resonance frequencies are well predicted by using only 60 CF terms while the old convergence rule would require 80 terms. Slight discrepancies exist at some non-resonant frequencies especially in the higher frequency part of the band. The corresponding one-third octave band SPL error is calculated, giving 0.13dB within the frequency band contained in Figure 4.10. The errors in Eq. 4.4 and the CF terms used by the proposed criterion and the traditional criterion for other one-third octave bands are listed in Table 3. It can be seen that β=1.5 leads to a slightly larger but still acceptable accuracy compared to the case of β=2 for all the bands in mid-

frequency range (starting from the band of 500Hz according to the previous definition). It is expected that the accuracy in the low-frequency range may deteriorate because of the insufficient modal density, exemplified by the band below 315Hz. As to the model size, the proposed selection criterion obviously reduces the number of the CF terms used, i.e. the matrix size in Eq. 3.11, leading to an expected increase in the calculation efficiency. It is understandable that the proposed criterion intends to guaranty the calculation accuracy only within the targeted frequency band, instead of trying to cover the entire frequency range, as shown in Figure 4.11a, in which the lower frequencies are deliberately abandoned. Nevertheless, as shown in Figure 4.11b, the proposed criterion can be applied to any arbitrarily selected bands, one at a time so that the entire frequency range can be covered by moving the bands in a sequential way. This sequential calculation scheme is what the piecewise computational means. This way, the calculation efficiency can be maximized in each frequency band of interest.

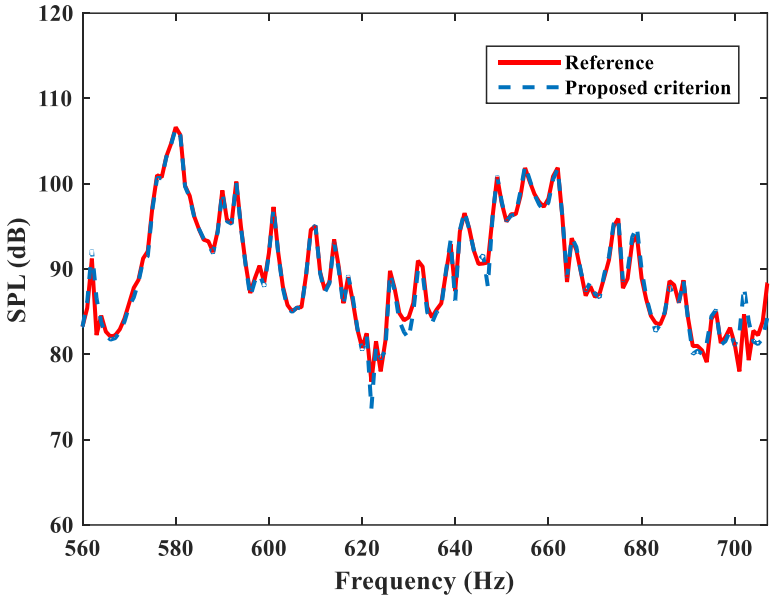

Figure 4.10 Calculated SPL using the proposed selection criterion for the one-third octave frequency band (center frequency: 630Hz).

Table 4.2 Performance of the proposed selection criterion

Center frequency of the one-third octave bands	Error		Piecewise terms		CTF terms (previous rule)
	β =1.5	β =2	β =1.5	β =2	
250Hz	1.16dB	0.21dB	20	22	31
315Hz	1.14dB	0.47dB	26	28	40
400Hz	0.75dB	0.52dB	34	36	51
500Hz	0.58dB	0.49dB	40	42	64
630Hz	0.13dB	0.02dB	50	60	80
800Hz	0.37dB	0.06dB	80	96	137
1000Hz	0.04dB	0.02dB	122	146	218

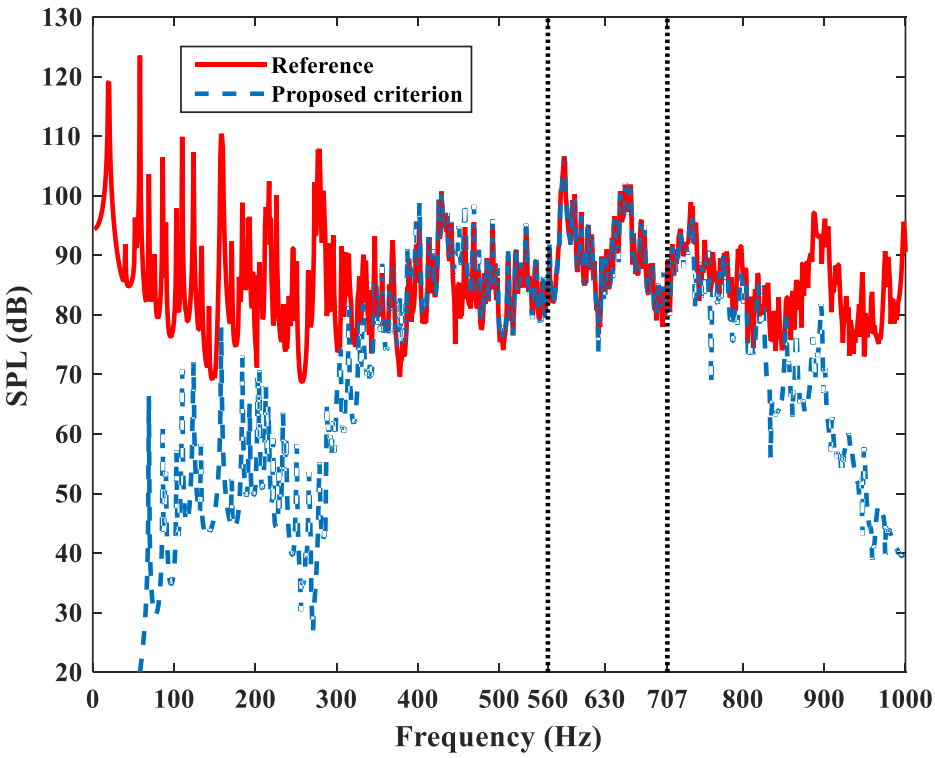

(a)

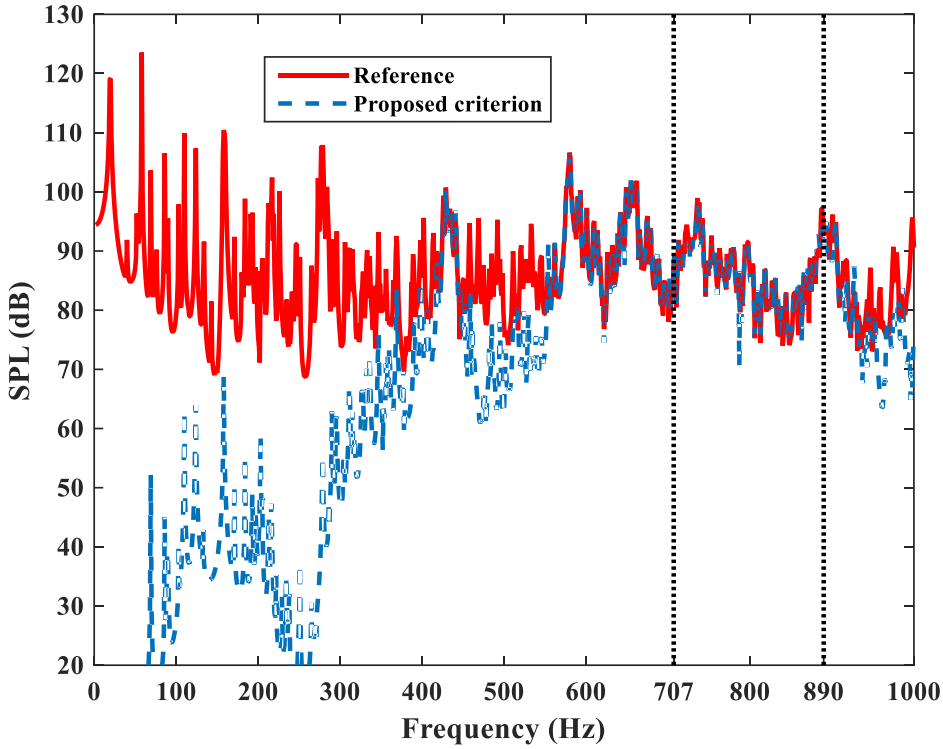

(b)

Figure 4.11 Sound pressure level using the proposed criterion targeting two selected one-third octave bands with the center frequency: (a) 630Hz; (b) 800Hz.

To further test the performance and the robustness of the proposed criterion, calculations are made by varying the system damping and the boundary condition of the panel, respectively. As far as the panel boundary is concerned, it is set to be clamped on all edges whilst all other parameters remaining the same. The condensed mobility in Eq. 3.12 is no longer obtained from analytical solution but from a numerical calculation using FEM software, implemented in COMSOL. Only results with β =1.5 are shown. The error with respect to various damping combinations and the error within different frequency bands of the clamped panel case are listed in Table 4.3 and Table 4.4, respectively. One can find in Table 4.3 that generally larger damping leads to a larger error of the calculation; the effect, however, is not significant at low damping levels. As to the effect of panel boundary conditions, one notices that

the errors in Table 4.4 are larger than those observed in Table 4.2. This is attributed to the inherent error existing in the finite element simulation used as the reference result. Limited by the calculation capacity, the mesh size could not be further refined. The SPL response at a randomly chosen point (0.3, 0.6, 0.7)m is shown in Figure 4.12. The proposed frequency piecewise computational scheme predicts well the system response at and close to resonances. Although one observes discrepancies at regions close to the anti-resonance frequencies where the system dynamics are weak. These regions, however, are not the major concern in terms of mid-and-high frequency calculations.

Table 4.3 Performance of the proposed criterion $\beta = 1.5$ for different sub-system damping combinations

Damping / Frequency	η^s=0.01 η^a=0.002	η^s=0.02 η^a=0.001	η^s=0.02 η^a=0.002
500Hz	0.80dB	0.64dB	0.76dB
630Hz	0.23dB	0.20dB	0.40dB
800Hz	0.45dB	0.35dB	0.52dB
1000Hz	0.20dB	0.19dB	0.34dB

Table 4.4 Performance of the proposed criterion $\beta = 1.5$ (clamped panel boundary)

Center frequency	400Hz	500Hz	630Hz	800Hz	1000Hz
Error	1.02dB	0.61dB	0.56dB	0.47dB	0.40dB

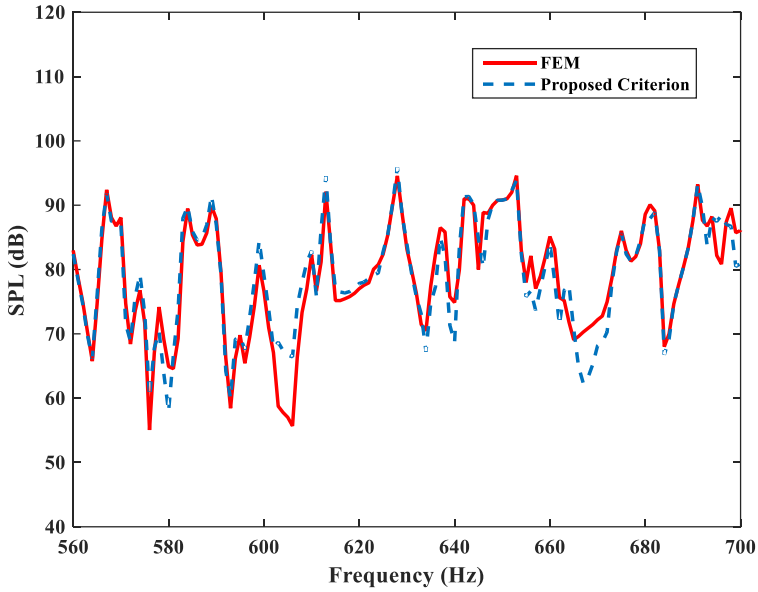

Figure 4.12 Sound pressure level using the proposed criterion targeting one-third octave bands within the 630Hz band (clamped plate).

Another case of a cavity with boundary impedance, coupled to a clamped panel, is considered. The impedance wall is located at *y*=0 within the *YOZ* plane as shown in Figure 2.3, with a normalized acoustic impedance of 33.5 with respect to the characteristic impedance of air $\rho_0 c_0$ [164]. Notice that the sound velocity c_0 =340*(1+0.001i) is complex. Therefore, the impedance used here is a complex quantity, including both resistance and reactance parts. The changes in the boundary conditions of the cavity serve the purpose of breaking down the symmetrical modal shape of the cavity as well as its spatial matching with the plate over the coupling surface. The impedance boundary can either be treated as a subsystem to be substituted into Eq. 3.11, or modeled as part of the entire cavity [164]. The former option is adopted in the present case. The calculated frequency band is increased to [1000, 1600]Hz. The volume averaged SPL calculated with β =1.5 is compared with the FEM result in Figure 4.13. It can be seen that the proposed piecewise computational scheme predicts well the system response in the entire frequency band of interest.

However, one observes discrepancies in regions where the system dynamics are weak. Three factors might result in these errors: higher frequencies, clamped plate boundary and the impedance wall. In Table 4.4, it can be observed that higher frequencies have little effect on the calculation error. Therefore, the change in the system boundary could be the main contributing factor. The inherent calculation error of the finite element simulation may also be part of the reasons behind these discrepancies. In the present case, the calculation time is also observed to be reduced. To give an indicative idea, the calculation time is rough 1/5 and 1/2 that of the FEM and conventional CTF, respectively. It should be noted that the exact calculation time may vary depending on the computer capability and the case under investigation.

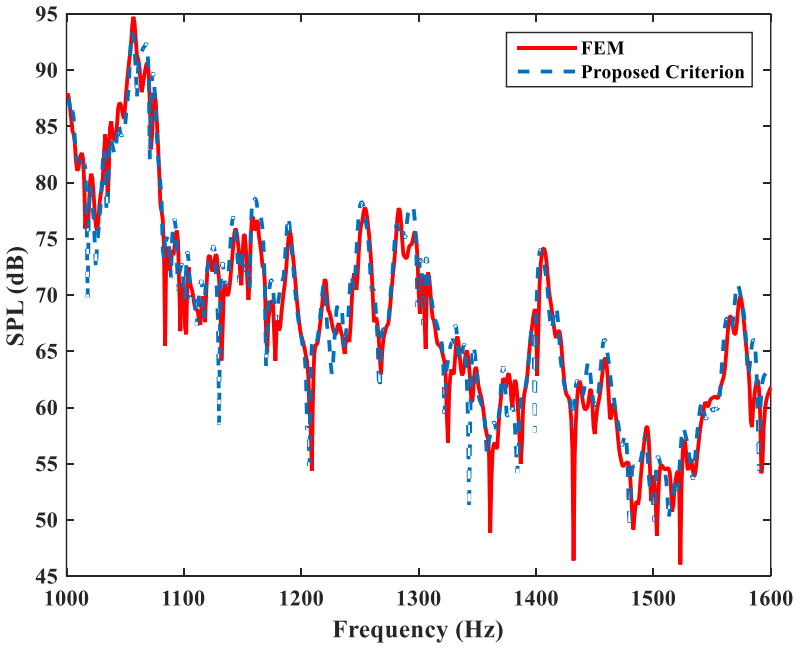

Figure 4.13 Sound pressure level using the proposed criterion targeting [1000, 1600]Hz (clamped plate and cavity with impedance boundary).

As a final remark, the calculation accuracy using the proposed piece-wise criterion and the time required for dealing with a larger cavity, (5 x 3 x 3)m for instance, is also tested. Under the same calculation condition as Fig. 8, the same calculation accuracy

is achieved, with however a much longer computation time (roughly 20 times). This is obviously due to the significant increase of the modal density in the frequency band.

4.3 Conclusions

Aiming at achieving effective modeling of a coupled panel-cavity system in the mid-to-high frequency range, a piecewise convergence behavior of the complex exponential function based CTF method is revealed, allowing a model reduction for mid-frequency simulations. This unique feature of the complex exponential functions is attributed to their wavy feature and spatial matching with the dynamics of the physical system. Based on that, a series selection criterion for the complex exponential CFs is proposed to further increase the calculation efficiency. Given a targeted frequency band $[f_l, f_h]$, all complex exponential CFs φ_{rs} with their wavelengths $\lambda_{c,rs}$ delimited by $\alpha\lambda_h < \lambda_{c,pq} < \beta\lambda_l$ are kept to form a subset, to be used in the calculation. It has been shown that using α=1 and β=1.5 can guarantee an acceptable prediction accuracy in most of the analyzed cases. Calculation errors might be larger in some frequency bands but still within the tolerance level typically required for mid-to-high frequency modeling. The most significant advantage of the proposed criterion is that it allows accurate modeling of the system in a piecewise manner in terms of frequency bands at a much-reduced model and calculation cost.

CHAPTER 5 Piecewise Computational Scheme for the Strongly Coupled Systems

In the last Chapter, a piecewise computational scheme based on the CTF method was developed to increase the modeling efficiency of mid-to-high frequency vibroacoustic systems. The scheme provides a controllable balance between the computational accuracy and efficiency, as illustrated using a plate-cavity system. However, such structure acoustic interaction is believed to be weak as mentioned in Section 2.2 of Chapter 1. Actually, one of the key challenges in the mid-to-high frequency modeling is the inability of the SEA in dealing with the strongly coupled system, which requires the use of deterministic approaches. This Chapter extends the previously established piecewise computational scheme beyond the weak-coupling assumption. Firstly, a coupling strength factor is proposed to quantify the coupling strength between two coupled sub-systems. Using an acoustic system comprising two mutually connected sub-cavities as a benchmark, one would see how different parameters influence the coupling strength. The piecewise computational scheme is revisited and validated in relation to the changes in the coupling strength level. Effects of the coupling strength on the computational error of the piecewise computational scheme are systematically studied. Finally, the applicability of the piecewise scheme is experimentally validated.

5.1 Coupling Strength Quantification

This section discusses the way to quantify the coupling strength between two coupled sub-systems and how different parameters would influence the coupling strength. According to the research of Kim and Brennan [165], the coupling between a vibrating plate and an acoustic cavity is considered to be weak since the response of either one sub-system, structural or acoustical, has little variation when the other one is attached. Therefore, a plate-cavity system is not suitable for the coupling strength investigations. To tackle the problem, a system of stronger coupling strength is required. Thus, a connected sub-cavities configuration is used as shown in Figure 5.1. This pure acoustic system will be used to introduce and validate the coupling strength factor. Then, similar analyses are repeated in a plate-cavity system for reference.

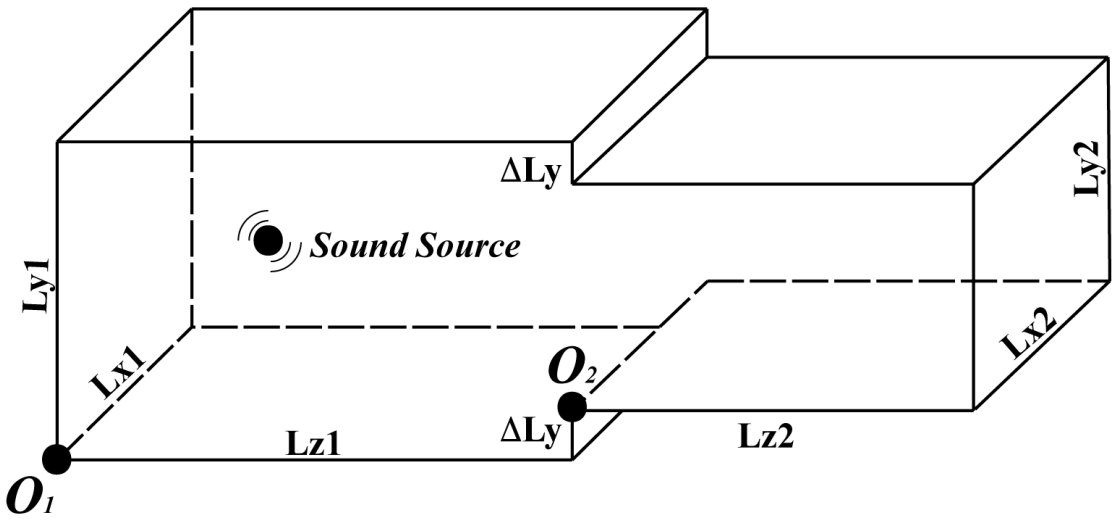

Figure 5.1 Configurations of the coupled acoustic system, excited by an internal sound source in the main sub-cavity.

5.1.1 Definition of the Coupling Strength Factor

In this thesis, the coupling strength is quantified by evaluating the response differences over the coupling interface before and after the attached sub-system is added. For the selected configuration in Figure 5.1, the coupling strength is quantified by the acoustic pressure differences over the coupling interface with and without the attached sub-cavity, $|\boldsymbol{P}_C - \boldsymbol{P}_e|$, where $\boldsymbol{P}_{\mathrm{C}}$ is the coupled pressure response and $\boldsymbol{P}_{\mathrm{e}}$ is the uncoupled blocked pressure. In light of Eq. 3.11, one has

$$\mathbf{P_c} = -\mathbf{Z}_{\mathbf{C}}^{2}[\mathbf{Z}_{\mathbf{C}}^{1} + \mathbf{Z}_{\mathbf{C}}^{2}]^{-1}\mathbf{P_e}. \tag{5.1}$$

When $\boldsymbol{P}_C \approx \boldsymbol{P}_{\mathrm{e}}$, the coupling is considered to be weak.

To quantify the coupling strength, a coupling strength factor Ω is defined, to be further used to assist the validations of the piecewise computational scheme under different coupling strength conditions. Define the coupling strength matrix $\mathbf{S} = -\mathbf{Z}_{\mathrm{C}}^{2}[\mathbf{Z}_{\mathrm{C}}^{1} + \mathbf{Z}_{\mathrm{C}}^{2}]^{-1}$ from Eq. 5.1. Because $\mathbf{Z}_{\mathrm{C}}^{1}$ and $\mathbf{Z}_{\mathrm{C}}^{2}$ are both invertible, **S** can be rewritten as $\mathbf{S} = \mathbf{K}^{-1}\boldsymbol{\Lambda}\mathbf{K}$ where the columns of **K** are the eigenvectors of **S** and $\boldsymbol{\Lambda}$ is a diagonal matrix containing the corresponding eigenvalues of **S**. For an uncoupled acoustic system, all λ_N are equal to one. λ_N is positively correlated with the response level p_N of the *N*th condensation function and the response level is smaller when an attached sub-system is added. Thus, we define

$$\Omega = \left|1 - \frac{\sum_N \lambda_N}{N}\right|, \tag{5.2}$$

where *N* is the dimension of **S** and λ_N is the *N*th eigenvalue of **S**. The summation of the eigenvalues can be replaced by the trace for easier calculation. Ω should increase as the coupling strength becomes stronger. For instance, Ω equals to zero when there

is no coupling and equals to one when the attached sub-system is equivalent to a pressure release boundary. Additionally, Ω is independent of the type and number of the selected condensation functions, so long as the convergence rules are satisfied.

5.1.2 Numerical Analyses on the Coupling Strength Factor

5.1.2.1 Analyses in a Cavity-cavity System

In this section, the relationship between the proposed Ω and the acoustic response differences over the coupling interface before and after coupling will be validated using an acoustic cavity shown in Figure 5.1.

Following Eq. 3.11, the condensed impedance matrix $\mathbf{Z}_{\mathrm{C}}^{1}$ and $\mathbf{Z}_{\mathrm{C}}^{2}$ are obtained and the velocity over the interface between the two sub-cavities can be solved either in a full or piecewise manner. Then, the coupling strength matrix **S** is rewritten as

$$\mathbf{S} = [\mathbf{I} + \mathbf{Z}_{\mathrm{C}}^{1}(\mathbf{Z}_{\mathrm{C}}^{2})^{-1}]^{-1}, \tag{5.3}$$

in which $\mathbf{Z}_{\mathrm{C}}^{1}(\mathbf{Z}_{\mathrm{C}}^{2})^{-1}$ can be further expanded as:

$$\mathbf{Z}_{\mathrm{C}}^{1}\left(\mathbf{Z}_{\mathrm{C}}^{2}\right)^{-1} = \frac{V_2}{V_1}\begin{bmatrix} \vdots & \cdots & \\ & \ddots & \vdots \\ & \cdots & \sum_m \frac{C_{kl,m}C_{rs,m}^{*}}{\Lambda_m(\omega_m^2-\omega^2+2i\xi\omega_m\omega)} \end{bmatrix}\begin{bmatrix} \vdots & \cdots & \\ & \ddots & \vdots \\ & \cdots & \sum_n \frac{C_{kl,n}C_{rs,n}^{*}}{\Lambda_n(\omega_n^2-\omega^2+2i\xi\omega_n\omega)} \end{bmatrix}^{-1}.$$

It can be seen from Eq. 5.3 that three factors influence the coupling strength: volume ratio of the two sub-cavities, frequency dependent terms, and the modal matching terms. For the volume ratio, the weak coupling can be identified when $V_2/V_1 \ll 1$. For a given main sub-cavity, the coupling strength increases with V_2. One should notice that the volume ratio is only valid for the current double-sub-cavity configuration. The second factor is the modal matching term $C_{kl,m}C_{rs,m}^{*}$. This factor

is non-dimensional and is determined by the spatial matching level between the CFs and the mode shapes of the two sub-systems. As for the frequency-dependent part, one would intuitively guess the strong coupling happens at resonances. Particularly when the two cavities share the same resonance frequency in the low-frequency range, the coupling process can be referred to the working mechanism of an acoustic resonator within an enclosure. However, in the mid-to-high frequency range, it is less relevant to focus on a single frequency but more reasonable to average it within a frequency band as $\frac{1}{\Delta f}\int_f \Omega df$.

For the present cavity configuration, the coupling strength is quantified based on the pressure differences over the interface with and without the attached sub-cavity, defined as:

$$D = \frac{1}{S}\int_S \frac{|P_e - P_C|}{|P_e|} dS. \tag{5.4}$$

D can be averaged in a frequency band as $\frac{1}{\Delta f}\int_f D df$. To eliminate the influence of the sound source location, P_e is not obtained by setting a particular sound source but assumed to be unit on all basis functions as

$$P_e = \begin{bmatrix} \varphi_{11} \\ \cdots \\ \varphi_{rs} \end{bmatrix}. \tag{5.5}$$

With such definition, Ω should reflect the variation trend of D when the dimension/volume of the attached sub-cavity changes, as shown in Figure 5.2, as a function of volume ratio by setting ΔLy=0 and varying Lz2. Both E and Ω are averaged in two selected frequency bands with a 200Hz bandwidth, centered at 1100Hz and 1500Hz, respectively. Ω obtained from the truncated series using piecewise scheme criterion is also shown for reference. It can be seen that Ω is only

slightly affected by the truncated series so long as the solution converges. Therefore, Ω will be calculated using the truncated series in the piecewise scheme in the following analyses. It can be observed in Figure 5.2 that D and Ω have the same variation trend as a function of V_2/V_1 and both, albeit not monotonously, exhibit an overall increasing trend with V_2/V_1. Fluctuations can be attributed to the resonances of the coupled system. Both D and Ω reach a local maximum value of 0.5 at V_2/V_1=1. It can be surmised that D and Ω will not be larger than 0.5 until $V_2 \gg V_1$, where V_2 can be approximately considered as infinitely large compared to V_1. Since we only aim at modeling the coupling process between two sub-systems with comparable sizes, the case of $V_2 \leq V_1$ will be the main focus of analyses in this paper. To better show the consistent variation trend between D and Ω, D is plotted as a function of in Figure 5.3a and b, averaged in the same two frequency bands. It can be seen that Ω is approximately proportional to D, i.e. the proposed coupling strength factor could effectively reflect the response differences over the interface as well as the coupling strength in agreement with our intuitive understanding.

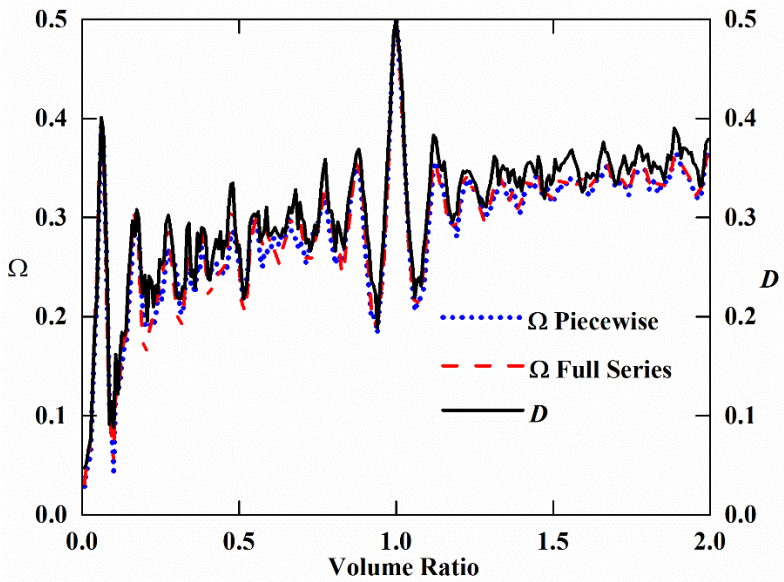

(a)

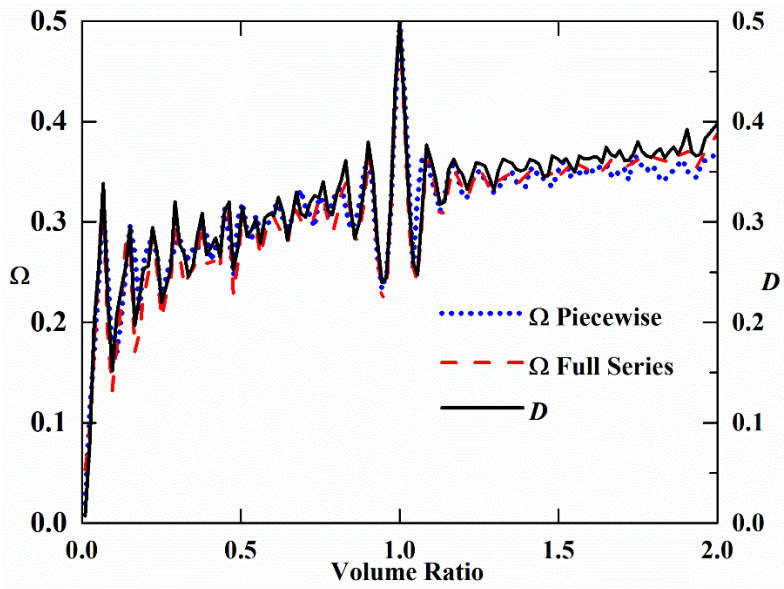

(b)

Figure 5.2 Interface pressure response differences *D* and the coupling strength factor Ω as functions of the volume ratio, averaged in frequency bands of 200Hz wide centered at: (a) 1100Hz; (b) 1500Hz.

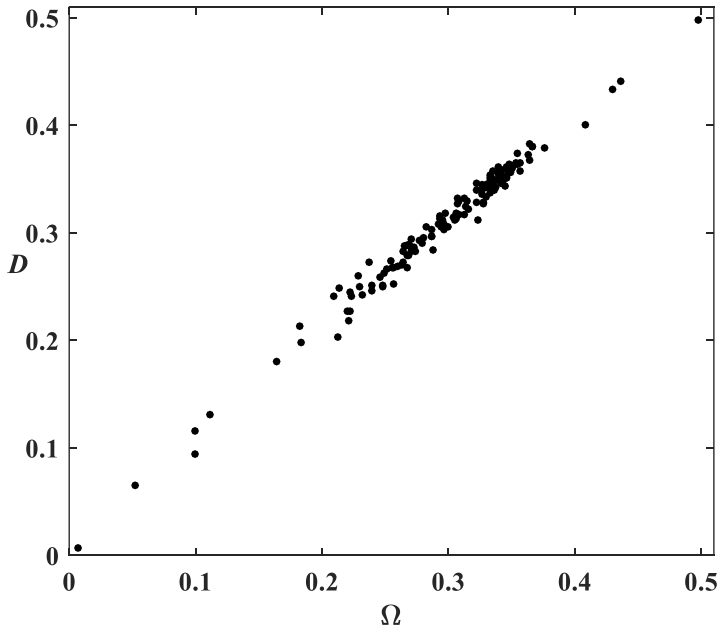

(a)

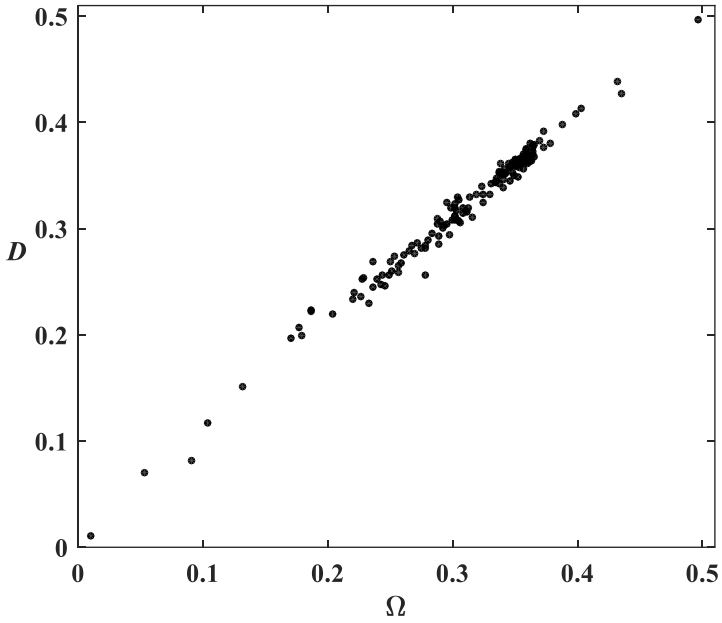

(b)

Figure 5.3 Relationship between the interface pressure response differences *D* and the coupling strength factor Ω, averaged in frequency bands of 200Hz wide centered at: (a) 1100Hz; (b) 1500Hz.

5.1.2.2 Analyses in a Plate-cavity System

Analyses can also be conducted for a plate-cavity system in a similar way. Referring to Figure 3.1, the main sub-system is set to be a plate while the attached sub-system is still an acoustic cavity and only structural excitation exists. The velocity over the interface can be expressed as

$$\mathbf{U_c} = -[(\mathbf{Y_C^1})^{-1} + \mathbf{Z_C^2}]^{-1}\mathbf{P_e}. \tag{5.6}$$

The weak coupling strength can be identified by rearranging Eq. 5.6 into

$$\mathbf{U_c} = -[(\mathbf{Y_C^1})^{-1} + \mathbf{Z_C^2}]^{-1}(\mathbf{Y_C^1})^{-1}\mathbf{U}_f \approx \mathbf{U}_f, \tag{5.7}$$

where $\mathbf{U}_f$ is the free velocity of the structure when it is excited. The coupling strength can be quantified as in Eq. 5.3:

$$\mathbf{S} = [\mathbf{I} + \mathbf{Y}^{-1}(\mathbf{Z}_C^2)^{-1}]^{-1}, \tag{5.8}$$

Then Ω can be obtained from the matrix trace of **S**. The difference between Eq. 5.8 and Eq. 5.3 is that the volume ratio becomes the ratio between the acoustic bulkling stiffness $K_a = \rho_0 c_0^2 S^2/V$ and the plate mass. The same conculsion was also shown in Ref. [165].

Figure 5.4 shows Ω and *D* as functions of the depth of the cavity (in the *z*-direction, also the out-of-plane direction of the plate). Notice *D* is obtained from the plate velocity. The plate is simply supported and made of aluminum, with a dimension of 2.5 x 2 x 0.018 (m). It can be observed that the coupling strength undergoes fast decrease as the cavity depth increases, which is consistent with many previous pieces of research [1, 70, 77]. Nevertheless, the coupling strength is much weaker than that of an acoustic-acoustic system (typically one order of magnitude lower) even if the cavity is very shallow (except for the first few sub-system resonances).

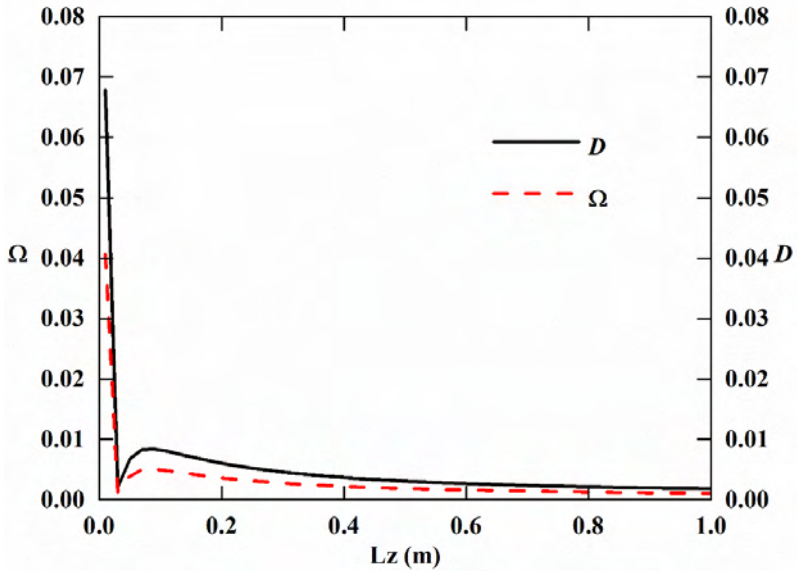

Figure 5.4 Influence of the cavity depth on the coupling strength of a plate-cavity system.

5.2 Numerical Validations of the Piecewise Scheme in Strong Coupling System

All numerical analyses are implemented based on the configuration shown in Fig. 5.1 unless otherwise specified. Before going into error analyses, some validations are presented by comparing the piecewise computational results and the analytical solutions obtained by setting ΔLy=0 and Lz2=Lz1. Notice that this configuration has the strongest coupling strength (Ω=0.5) for the considered cases. Then, the computational error of the piecewise scheme will be examined under different coupling strength levels.

5.2.3 Validations on the Interface Velocity

By setting ΔLy=0, the main sub-cavity and attached sub-cavity form a rigid rectangular cavity so that the analytical solution can be obtained as the reference result. The CTF-based piecewise computational scheme treats the cavity as two sub-systems.

Firstly, the result of the interface velocity prediction is examined. The coupled velocity at 1000Hz is mapped in Figure 5.5. The results obtained from the piecewise scheme and the analytical solution are shown in Figure 5.5a and b, respectively. Generally, the piecewise scheme can well predict the acoustic particle velocity pattern over the interface, particularly at where local maximums exist. However, it can be found that the prediction result of the piecewise scheme is not as accurate as that in the plate-cavity system shown in Chapter 4. This conclusion points at the need and the significance in validating the performance of the piecewise scheme in strongly coupled systems.

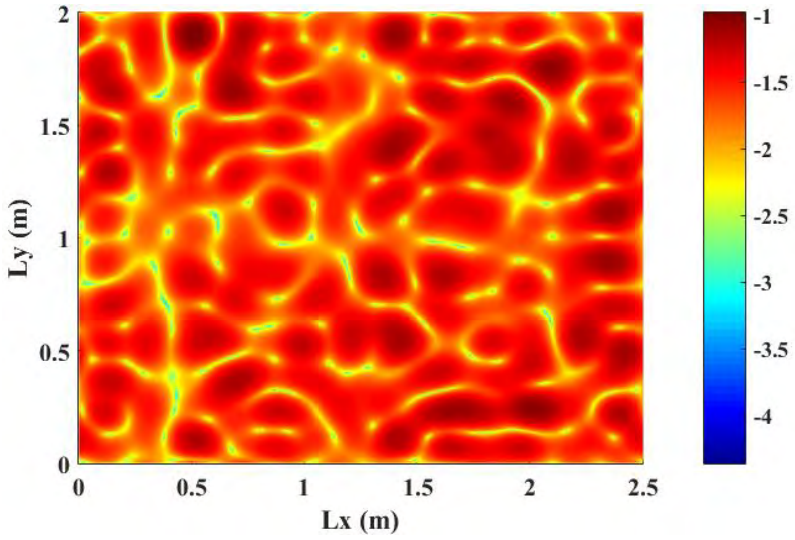

(a)

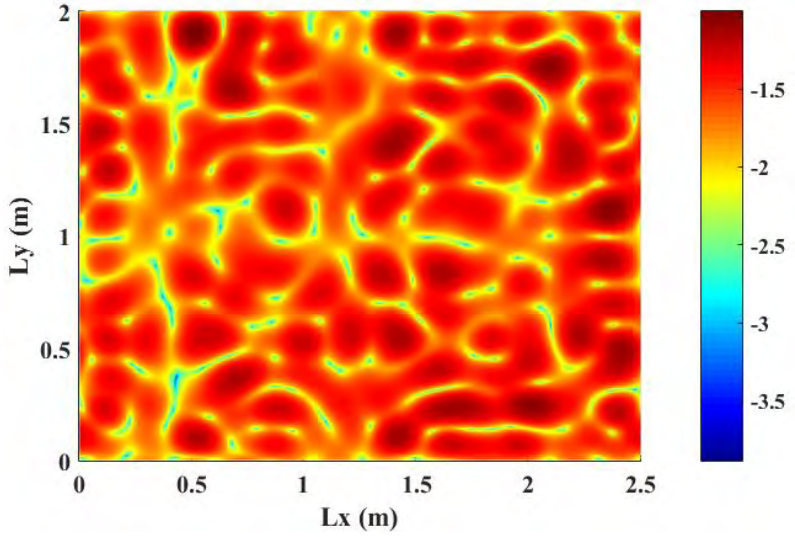

(b)

Figure 5.5 Velocity distribution over the coupling interface at 1000Hz, obtained from: (a) Analytical solution; (b) Piecewise calculation.

5.2.2 Validations on the Acoustic Pressure

After checking the prediction accuracy of the coupled velocity, we examine the response of the two sub-cavities. Comparisons in terms of the sound pressure level

(SPL) are made at two arbitrarily receiving points, located in the sub-cavities 1 and 2 respectively. The results are shown in Figure 5.6, in which only results in mid-to-high frequency bands are presented. The dotted line, obtained from the piecewise scheme, includes 4 individual piecewise calculations, with a 200Hz bandwidth each time. Note a broader band will reduce the computational efficiency and dilute the advantage of the method. Nevertheless, a broader computational band could increase the accuracy of the method due to the inclusion of more CF terms. The results obtained from the full CTF calculation are also shown as a reference. It can be observed that the piecewise calculation can well capture the SPL, especially for those resonance peaks. Although errors exist at some anti-resonance frequencies, they are not the major concern of the mid-to-high frequency problem. Figure 5.7a shows the sound pressure distribution, obtained from the piecewise scheme, over the coupling interface at 1100Hz. The result is consistent with that obtained from the analytical solution in Figure 5.7b. Similar accuracy was also checked to exist at other receiving points and cut surfaces (not shown here). Figure 5.8 shows the volume-averaged SPL within each 200Hz bandwidth. It can be observed that the errors are capped at around 2dB. Notice these errors can be reduced by enlarging the computational bands. The errors are found to be less than 1dB when the same calculations are conducted within the one-third octave bands centered at 1250Hz and 1600Hz.

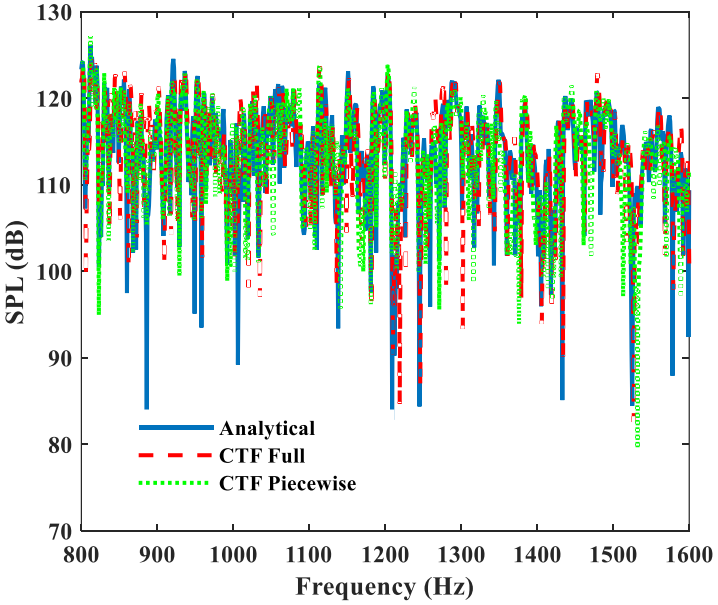

(a)

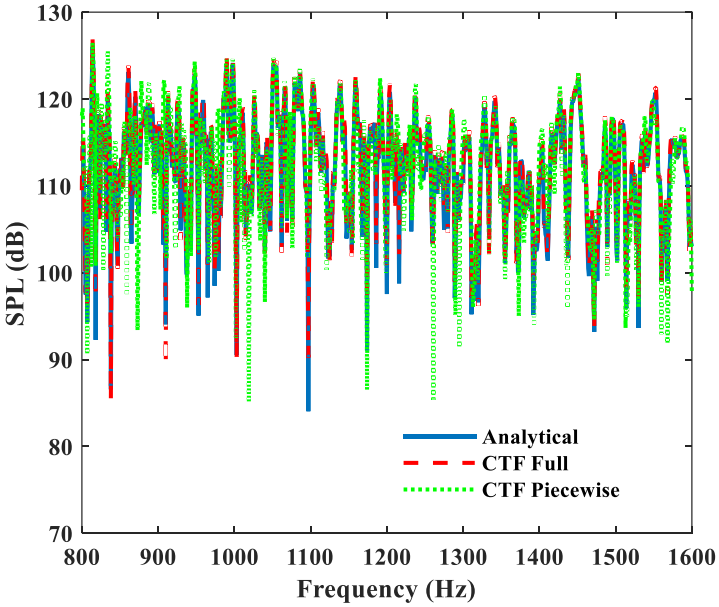

(b)

Figure 5.6 SPL at: (a) (1.7, 1.3, 1.2) m in the main cavity; (b) (2.1, 0.6, 0.9) m in the attached cavity.

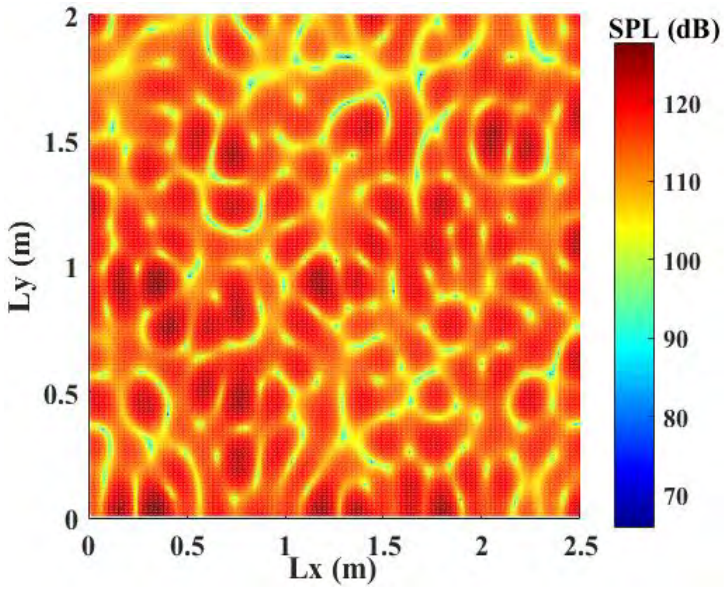

(a)

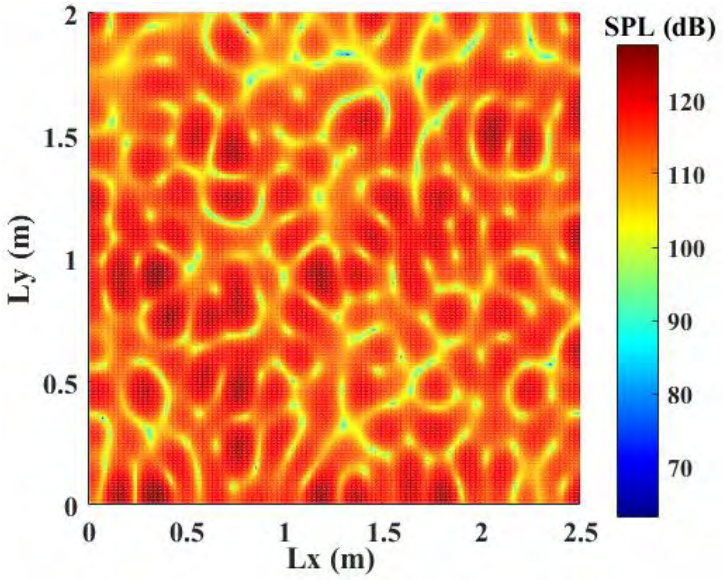

(b)

Figure 5.7 SPL distribution over the coupling interface: (a) Piecewise scheme; (b) Analytical solution.

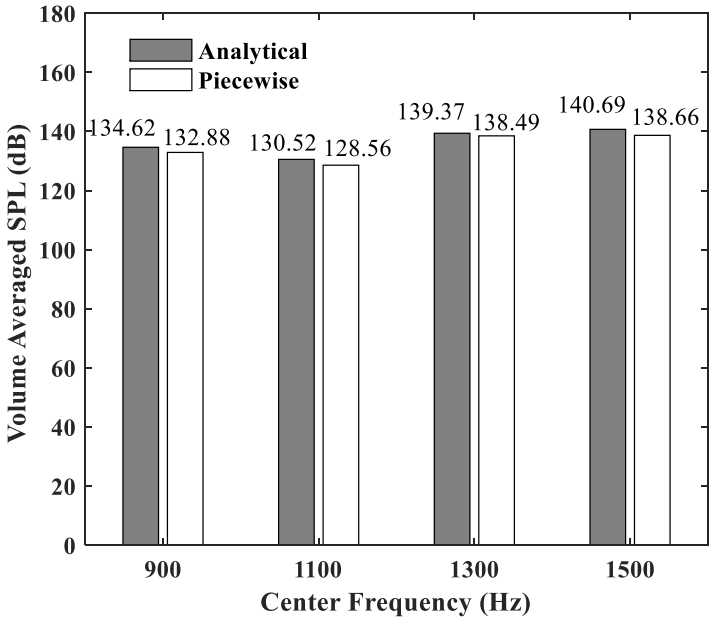

Figure 5.8 Volume-averaged SPL within frequency bands of 200Hz wide: analytical solution and piecewise scheme.

The above results numerically validate the piecewise scheme in a strongly coupled system. The method well balances the efficiency and accuracy within mid-to-high frequency ranges. Particularly, it can provide a detailed prediction of the acoustic field in both sub-systems, which is the most appealing advantage over the SEA.

5.3 The Influence of Coupling Strength on the Piecewise Scheme

In this section, the influence of the coupling strength on the performance of the piecewise computational scheme will be investigated. As discussed above, the coupling strength is mainly determined by the volume ratio and the modal matching matrix in the mid-to-high frequency range. Therefore, firstly these two factors are separately investigated and then a general conclusion is drawn at the end of this section to conclude the relationship between the coupling strength and the performance of the

piecewise scheme. For analyses purposes, the error of the piecewise computational scheme is defined within a given frequency band Δf as:

$$E_c = \frac{1}{S\Delta f}\int_{\Delta f}\int_{S}\left|P_{pw} - P_c\right| dSdf, \tag{5.9}$$

where P_{pw} is the piecewise solution and P_c the full CTF calculation or analytical solution whenever available.

5.3.1 Volume Ratio

This subsection discusses the effect of the volume ratio on the performance of the piecewise computational scheme, by using the same configurations as those used in Figure 5.1. As a reference, the coupling strength factors of the analyzed configurations are shown in Figure 5.9a. As stated, only $V_2 < V_1$ is considered here. Figure 5.9b shows the errors of the piecewise scheme for two frequency bands of 200Hz wide, centered at 1100Hz and 1500Hz, respectively. It can be observed in Figure 5.9b that E_c becomes larger as the volume ratio V_2/V_1 increases. Comparison between Figure 5.9a and b shows that E_c increases as the coupling strength gets stronger. The maximum value of E_c is between 1.6 to 1.8dB when $V_2 = V_1$, which is still within the general tolerance level for the mid-to-high frequency modeling. One may desire for the detailed performance when E_c is the largest at $V_2 = V_1$. These results can be referred to what were summarized in Section 5.2.

It is worth noticing that the relatively large E_c only arises when the volume ratio V_2/V_1 is close to one, when the two cavities are identical. In this case, neither cavity is more deterministic nor statistical than the other. This shows the capability of the piecewise computational scheme in solving strongly coupled systems where

deterministic-statistical methods are no longer applicable to provide detailed system responses of the whole system.

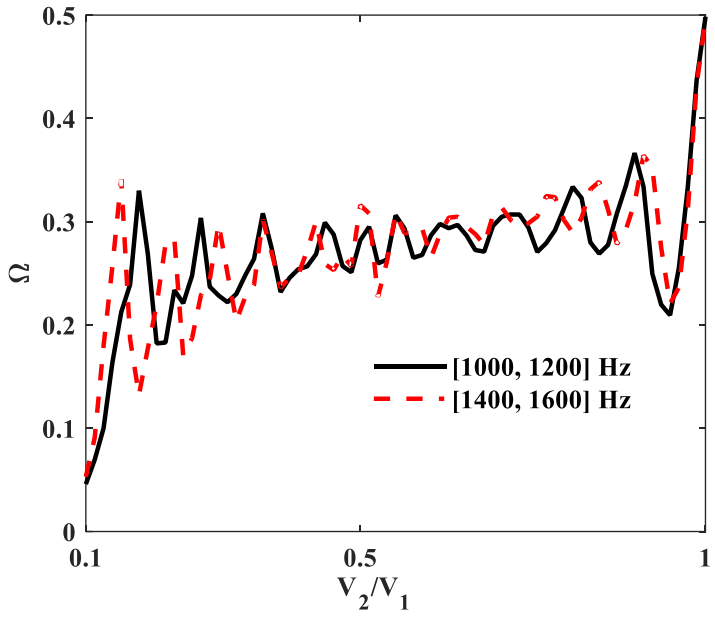

(a)

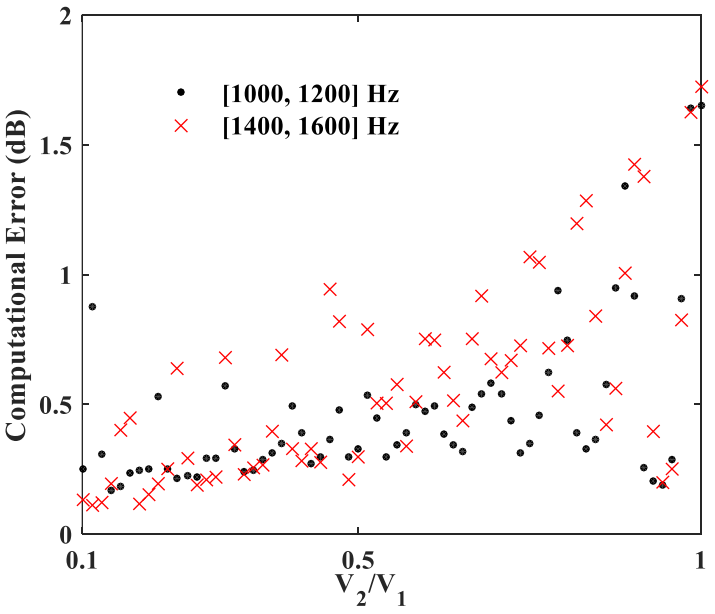

(b)

Figure 5.9 Surface velocity error of the piecewise scheme with respect to different volume ratios in frequency bands of 200Hz wide centered at: (a) 1100Hz; (b) 1500Hz.

5.3.2 Interface Modal Matching

The effect of the interface modal matching on the performance of the piecewise scheme is investigated in this subsection. Different from the volume ratio, appearing as an amplification coefficient in Eq. 5.3, the modal matching matrix is directly determined by the piecewise scheme. The variation of the interface modal matching is achieved by increasing ΔLy from 0 to 0.5m, as shown in Figure 5.1. When ΔLy=0.5m, the interface area becomes half of its largest value. To keep the volume ratio constant at one, the depth of the attached cavity Lz2 is automatically adjusted. All analyzed quantities are frequency averaged within the two frequency bands which are the same as in Figure 5.9.

Firstly, the coupling strength factors are plotted for different ΔLy in Figure 5.10a. It can be observed that the coupling strength generally decreases as ΔLy gets larger, corresponding to a smaller interface area, in line with one's intuition. However, this is not simply due to the smaller interface area because $C_{kl,m}C^*_{rs,m}$ is not only determined by the area but also depends on the wave matching level over the interface, which is very complex in the mid-to-high frequency range. For the present case, the variation trend of Ω indicates that the modal matching level becomes smaller as ΔLy decreases since the influences of the volume ratio and frequency are excluded in the simulations.

The computational errors for different ΔLy are shown in Figure 5.10. Again, one observes the similar variation trends as the coupling strengths have. As ΔLy increases, the computational errors quickly drop at the beginning and converge to a small value around 0.2dB. The same conclusion as in Section 5.3.1 can be drawn in that the computational error is larger when the two cavities are similar. This verifies the

capability of the piecewise scheme in strong coupled cases where the modal matching levels are different.

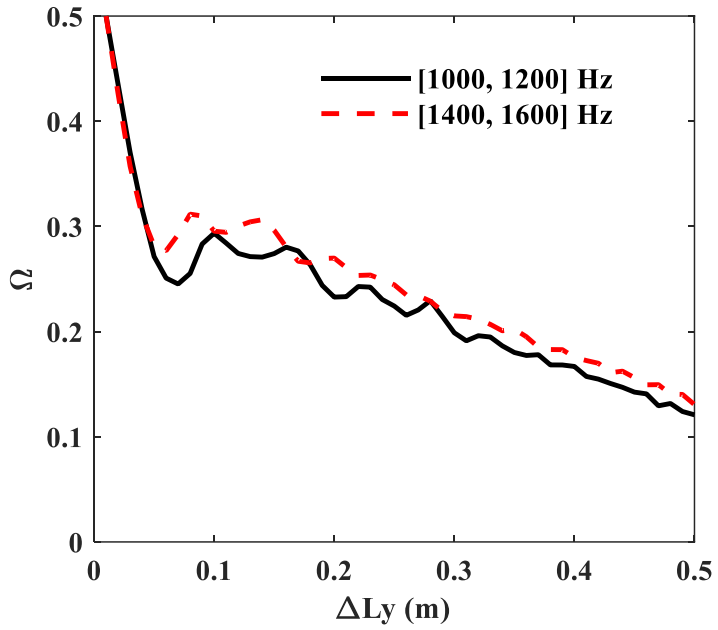

(a)

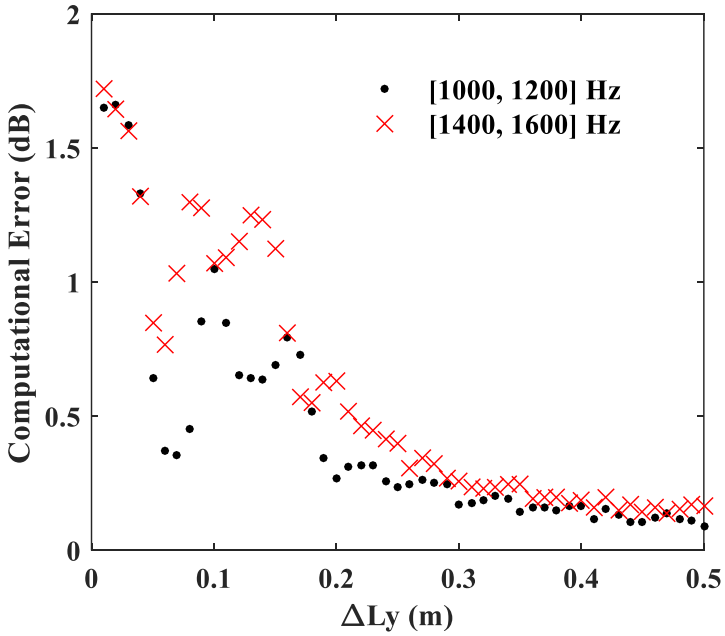

(b)

Figure 5.10 Surface velocity error of the piecewise scheme with respect to different modal matching in frequency bands of 200Hz wide centered at: (a) 1100Hz; (b) 1500Hz.

5.3.3 Coupling Strength

To summarize the above analyses results, the computational data used in Figure 5.2, Figure 5.9, and Figure 5.10 are rearranged and regrouped to plot the computational error E_c as a function of the coupling strength Ω, obtained from different volume ratios and modal matching matrix and averaged in [1000, 1200]Hz and [1400, 1600]Hz, respectively. This results in a total of four sets of results in Figure 5.11 with a different type of markers. It can be observed that, irrespective of the way the coupling strength is obtained, the errors at any given Ω are rather consistent in trend and close in values. For relatively weak coupling strength, when Ω is smaller than 0.2, the error of the piecewise scheme is rather stable and dwells around 0.2dB. When Ω becomes larger than 0.2, the error undergoes fast increases before gradually stabilizes when Ω is larger than 0.4. It should be noted that, between 0.2 and 0.4, that the increasing speed of the error is not exactly the same because the piecewise scheme has different sensitivities to volume ratio, modal matching level, and frequency bands. It is also relevant to note that the higher frequency band exhibits a larger error. One of the plausible reasons is the wave motion over the interface is more complex in a higher frequency band so that a wider calculation bandwidth Δf compared to its center frequency would be needed to warrant a more accurate prediction. However, this can be avoided by considering the one-third octave or octave bands as people usually do in mid-to-high frequency modeling problems.

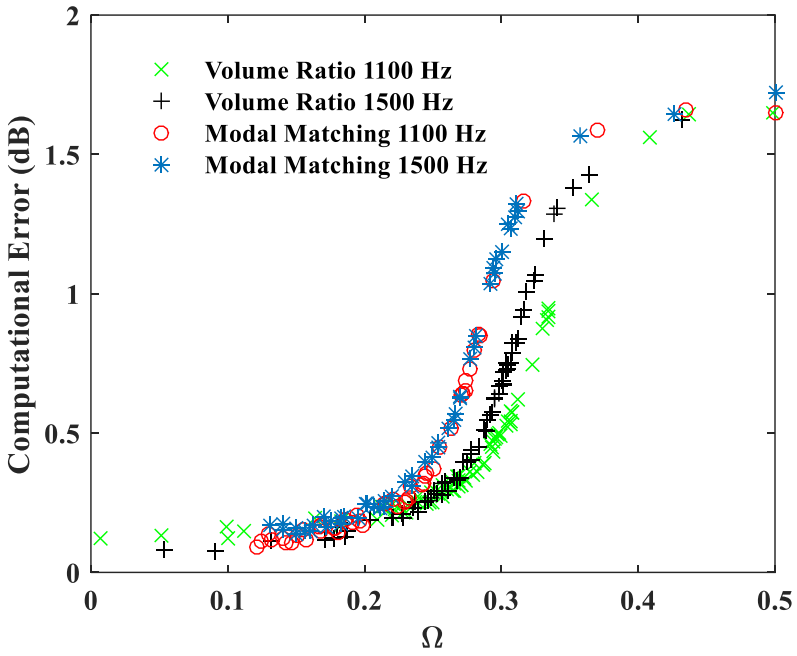

Figure 5.11 Computational error E as a function of the coupling strength varied with volume ratio or modal matching matrix, averaged within [1000, 1200]Hz and [1400, 1600]Hz.

5.4 Experimental Validations

Experimental validations were carryout out using a configuration shown in Figure 5.12. The cavity walls are made of acrylic of 30mm thickness which can be considered as acoustically rigid. A loudspeaker was used to generate an acoustic excitation through a hole drilled at (0.075, 0.05, 0) m over the sidewall. Microphones 1 and 2 were installed at (0.075, 0.05, 0.01) mm and (0.25, 0.15, 0.83) m, respectively, to measure the transfer function between them and eliminate the sound source error at the same time [166]. Limited by the experimental conditions, the cavity dimensions are smaller than those used in the previous simulations. However, a higher frequency band up to 3200Hz was selected instead. For reference, the volume ratio V_2/V_1 is 0.94.

The experiment was conducted within a wide frequency band of [40, 3200]Hz, with results shown in Figs. 5.13a and b, respectively. It was shown in the previous work that the piecewise scheme starts to be applicable when the modal overlap factor is larger than one. In the present test structure, the unit modal overlap factor is at approximately obtained at 1200Hz. Therefore, the full CTF calculation is used within [40, 1200]Hz and the piecewise scheme is used within [1200, 3200]. To obtain more accurate peak values at resonance frequencies, the damping ratio of the first four peaks are obtained from the experimental result while the others are all set to 0.001. It can be observed in Figure 5.13a that the full CTF calculation result agrees well with the experimental one, in terms of both resonance and anti-resonance frequencies as well as the overall trend. The piecewise calculation (Figure 5.13b) was conducted within ten frequency bands of a 200Hz bandwidth and added up to [1200, 3200]Hz. It can be seen that the piecewise scheme can accurately capture the variation trend and most of the resonance peaks. The few missing peaks in the experimental curve can be attributed to the machining tolerance of the cavity and some unavoidable uncertainties. All in all, the validity of the piecewise computational scheme is considered to be verified in such a highly dynamic and strongly coupled system.

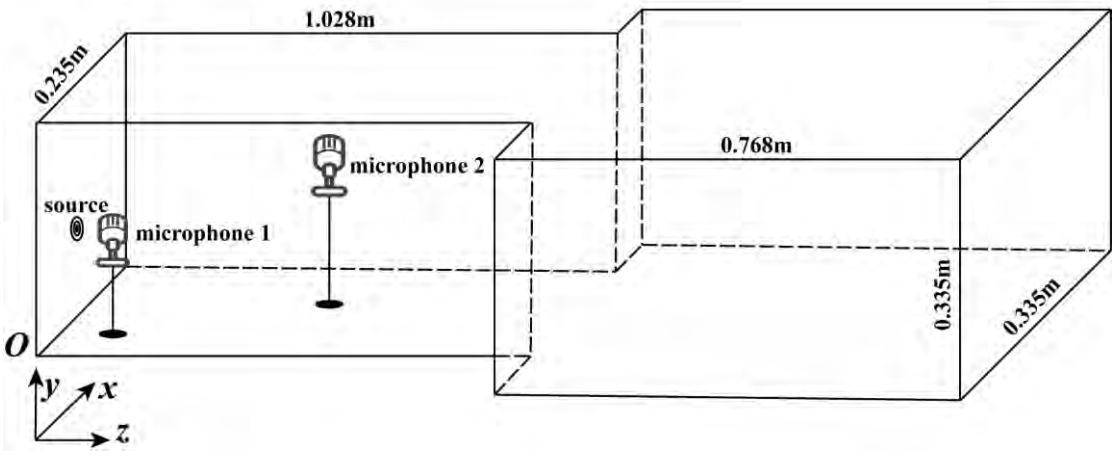

(a)

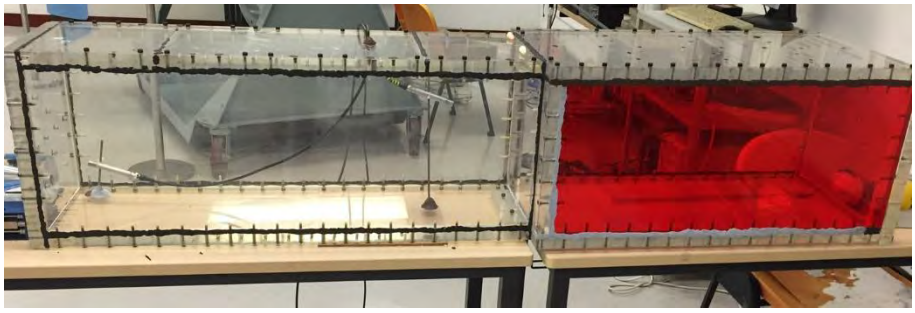

(b)

Figure 5.12 The cavity where the experiments conducted: (a) Cavity configuration; (b) Photo of the cavity.

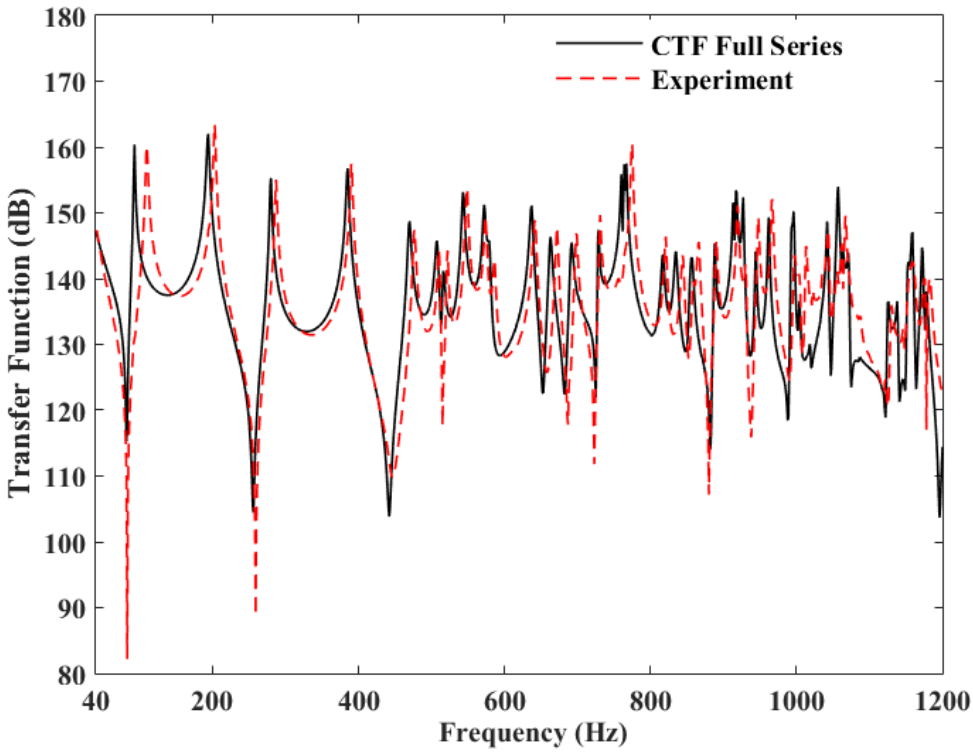

(a)

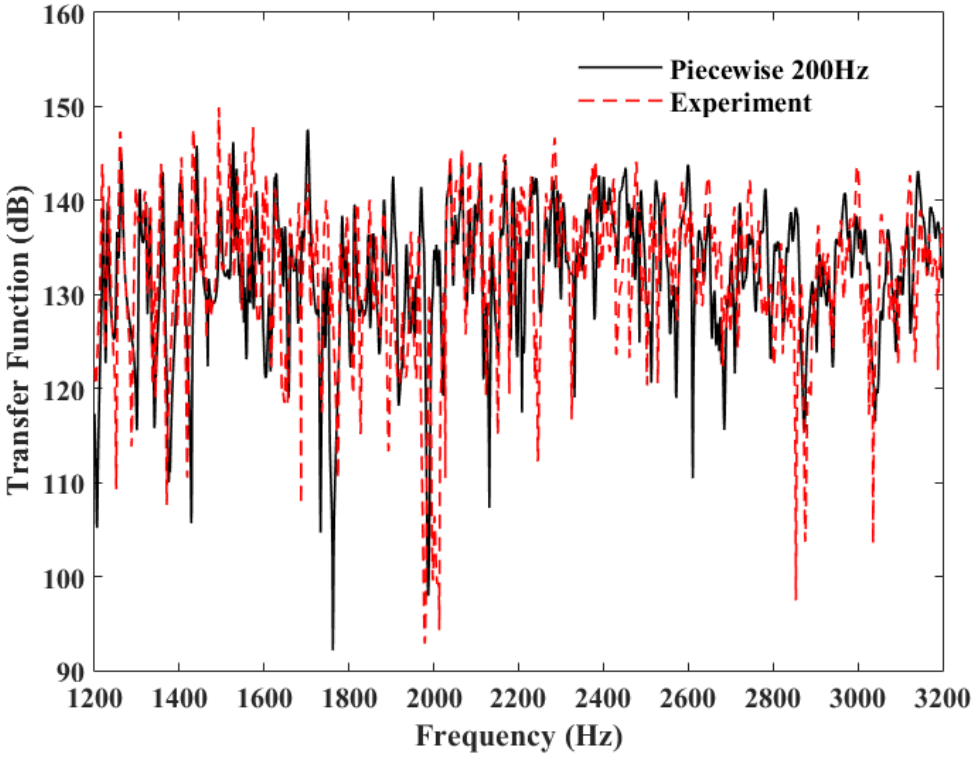

(b)

Figure 5.13 Predicted transfer function between two points, compared to the experimental result: (a) Full CTF calculation; (b) Piecewise scheme.

5.5 Summary

This Chapter extends the application range of a previously proposed piecewise computational scheme to strong coupling cases. The coupling strength is defined by examining the acoustic response differences over the coupling interface before and after the attached sub-system is added. A coupling strength factor Ω is defined to quantify the coupling strength in the context of a multi-degree freedom system and mid-to-high frequency range. With the assistance of Ω, the computational errors of the piecewise scheme are investigated through tactically varying the coupling strength

level, including the strongly coupled system. Generally, the proposed piecewise computational scheme is shown to be applicable in strongly coupled cases, by showing a good agreement with the analytical solutions and the experiment results. Main conclusions are summarized as follows.

1. The proposed coupling strength factor Ω can well reflect the variation trend of the coupling strength between two coupled sub-systems, as reflected by the acoustic response differences over the coupling interface. Three factors are found to affect the coupling strength between two acoustic sub-cavities: volume ratio, interface modal matching level and the frequency. By comparing the value of Ω, the coupling strength in an acoustically coupled system is shown to be generally much stronger than that of the structure-cavity system.

2. The piecewise computational scheme is shown to be effective and accurate enough in the modeling of a strongly coupled acoustic cavity. Without losing the efficiency and compromising its accuracy, the proposed scheme allows a detailed sound field description of each sub-system.

3. The computational error increases when the coupling strength becomes stronger, which, nevertheless, is still within the normal tolerance level in terms of the mid-to-high frequency modeling. For a given system and a prescribed frequency band, the computational error of the piecewise computational scheme can be approximately evaluated from Ω.

CHAPTER 6 Applications in Building Acoustics

In previous Chapters, the CTF method, as well as the piecewise computational scheme, has been thoroughly and systematically validated. In this Chapter, the proposed method will be applied to a simplified Double Skin Façade (DSF) system. The capability of the method will be shown and examined in this particular context. The sound insulation properties of some selected DSF configurations will be parametrically studied. Meanwhile, Micro-Perforated Panels (MPP) will be used as a noise control device, to be integrated into the model. The established CTF framework allows the MPP to be modeled not only as a locally reacting sound absorption device but also as an individual sub-system that is coupled with its surrounding acoustic environment. By revealing the working mechanisms of the MPP, parametric studies are conducted for MPP as well to maximize its performance. As a more realistic configuration, an internal sound transmission model between two floors is studied. It is demonstrated that significant calculation efficiency improvements can be achieved by the proposed piecewise computational scheme, outperforming existing simulation tools widely used in building acoustics.

6.1 Theoretical Model

This section presents the theoretical models of the system to be used later for investigation in this Chapter. The models are built under the general CTF framework detailed in previous Chapters. Either the piecewise or the full calculation schemes can be used according to practical needs, frequency ranges and efficiency requirements. As mentioned above, MPPs will be taken into account in the models. Therefore, their acoustic impedance will first be shown, so that it can be converted to condensed impedance and embedded into the CTF formula.

6.1.1 Modeling on the Micro-Perforated Panel

One of the most popular models to predict the performance of an MPP is given by Maa [167]. The acoustic impedance of the MPP, z_{MPP}, can be described by the hole diameter d, perforation ratio σ and panel thickness t, as:

$$z_{MPP} = r + j\omega m, \tag{6.1}$$

where

$$r = \frac{32\eta t}{\sigma \rho_0 c d^2} k_r, k_r = \left[1 + \frac{k^2}{32}\right]^{1/2} + \frac{\sqrt{2}}{32} k \frac{d}{t} \tag{6.2}$$

$$\omega m = \frac{\omega t}{\sigma c} k_m, k_m = 1 + \left[1 + \frac{k^2}{2}\right]^{-1/2} + 0.85 \frac{d}{t} \tag{6.3}$$

and

$$k = d \sqrt{\frac{\omega \rho_0}{4\eta}}, \tag{6.4}$$

in which η is the air viscosity coefficient.

Traditionally, the MPP governed by Eq. 6.1 works together with a backing cavity, forming a so-called MPP absorber (MPPA). A separation structure within the backing cavity, like a honeycomb, could avoid the interactions among different holes so that the entire MPPA can be treated like a piece of locally reacting material. Basically, the backing cavity contributes no additional acoustic resistance to the MPPA and considering its relative acoustic reactance $-\cot(\omega D/c)$ where D is the depth of the backing cavity, the acoustic impedance of the MPPA is given by

$$z_{MPPA} = r + j[\omega m - \cot\left(\frac{\omega D}{c}\right)], \tag{6.5}$$

Equation 6.5 can be directly embedded into the CTF formulation to obtain the condensed velocity if the MPP is considered to be locally reacting.

However, recent researches [159, 168, 169] show that, without a partitioned backing cavity, an MPP can no longer be treated as a locally reacting material but a structural/acoustic element coupled with the acoustic environment surrounding it. In that case, the velocity over the MPP surface is determined by the acoustic pressure distribution on the two sides, as

$$u_{MPP} = \frac{p_1 - p_2}{\rho_0 c z_{MPP}}. \tag{6.6}$$

Then, u_{MPP} can be decomposed to the CF coordinates so as to be substituted into the CTF formula.

6.1.2 Modeling of DSF systems

A typical configuration consisting of the single-layer DSF system is considered. Although 3D configuration is considered in the following analyses, a 2D projection is shown in Figure 6.1. MPPs are used either as a screen or a sound absorption wall. In

the latter case, when MPP is absent, corresponding surfaces become rigid walls. The DSF cavity and the room are connected through a ventilation opening. Several notations are annotated in Figure 6.1. The room is denoted as Cavity 3 (C3) and an MPP screen divides the DSF cavity into two sub-cavities: C1 and C2. When the MPP is absence, the DSF cavity is denoted as C1 only. The outer glass, inner glass, and ventilation opening are represented as interfaces 1, 2, and 3, respectively. The MPP screen and the locally reacting MPP wall are denoted as interfaces 4 and 5, respectively.

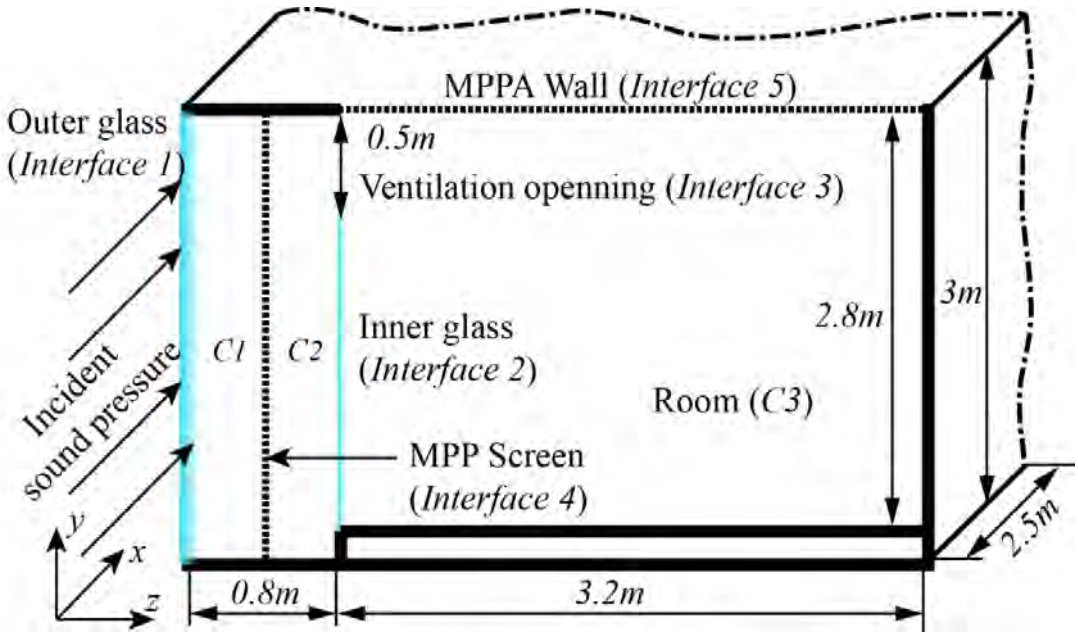

Figure 6.1 Configuration of a single layer DSF system.

For the CTF modeling, the condensed impedance or mobility can be separately obtained for the DSF cavity, room, and glasses, respectively. In what follows, $\mathbf{Y}_1$ and $\mathbf{Y}_2$ are the condensed mobility of the outer glass and the inner glass, respectively. For the condensed impedance, taking $\mathbf{Z}_{23}^{C3}$ as an example, the superscript C3 represents the DSF the room and the subscript 23 represents the prescribed velocity at interface 2 and the pressure response at interface 3. Detailed expressions are given in the

Appendix. When the two MPP interfaces are absent, three force equilibrium equations can be written for the outer glass, the inner glass, and the ventilation opening, as

$$\begin{gathered}(-\mathbf{Y}_1^{-1}+\mathbf{Z}_{11}^{C1})\mathbf{U}_1+\mathbf{Z}_{21}^{C1}\mathbf{U}_2+\mathbf{Z}_{31}^{C1}\mathbf{U}_3=\mathbf{P}_e,\\ \mathbf{Z}_{12}^{C1}\mathbf{U}_1-\left(\mathbf{Z}_{22}^{C1}+\mathbf{Z}_{22}^{C2}-\mathbf{Y}_2^{-1}\right)\mathbf{U}_2-(\mathbf{Z}_{32}^{C1}+\mathbf{Z}_{32}^{C2})\mathbf{U}_3=\mathbf{0},\\ \mathbf{Z}_{13}^{C1}\mathbf{U}_1-\left(\mathbf{Z}_{23}^{C1}+\mathbf{Z}_{23}^{C2}\right)\mathbf{U}_2-(\mathbf{Z}_{33}^{C1}+\mathbf{Z}_{33}^{C2})\mathbf{U}_3=\mathbf{0}\end{gathered} \tag{6.7}$$

where $\mathbf{P}_e$ is the external pressure excitation, $\mathbf{U}_1$, $\mathbf{U}_2$, and $\mathbf{U}_3$ are the condensed velocity vectors of the outer glass, inner glass, and ventilation opening, respectively. Writing Eq. 6.7 into matrix form and inversing the impedance matrix, the condensed velocity vector can be solved as,

$$\begin{bmatrix}\mathbf{U}_1\\ \mathbf{U}_2\\ \mathbf{U}_3\end{bmatrix}=\begin{bmatrix}-\mathbf{Y}_1^{-1}+\mathbf{Z}_{11}^{C1} & \mathbf{Z}_{21}^{C1} & \mathbf{Z}_{31}^{C1}\\ \mathbf{Z}_{12}^{C1} & -\mathbf{Z}_{22}^{C1}-\mathbf{Z}_{22}^{C2}-\mathbf{Y}_2^{-1} & -\mathbf{Z}_{32}^{C1}-\mathbf{Z}_{32}^{C2}\\ \mathbf{Z}_{13}^{C1} & -\mathbf{Z}_{23}^{C1}-\mathbf{Z}_{23}^{C2} & -\mathbf{Z}_{33}^{C1}-\mathbf{Z}_{33}^{C2}\end{bmatrix}^{-1}\begin{bmatrix}\mathbf{P}_e\\ \mathbf{0}\\ \mathbf{0}\end{bmatrix}. \tag{6.8}$$

With two MPPAs taken into account, the governing equations of the whole system are given by,

$$\begin{gathered}(-\mathbf{Y}_1^{-1}+\mathbf{Z}_{11}^{C1})\mathbf{U}_1+\mathbf{Z}_{41}^{C1}\mathbf{U}_4=\mathbf{P}_e,\\ -(\mathbf{Z}_{22}^{C2}+\mathbf{Z}_{22}^{C3}-\mathbf{Y}_2^{-1})\mathbf{U}_2-(\mathbf{Z}_{32}^{C2}+\mathbf{Z}_{32}^{C3})\mathbf{U}_3+\mathbf{Z}_{42}^{C2}\mathbf{U}_4+\mathbf{Z}_{52}^{C3}\mathbf{U}_5=\mathbf{0}\\ -(\mathbf{Z}_{23}^{C2}+\mathbf{Z}_{23}^{C3})\mathbf{U}_2-(\mathbf{Z}_{33}^{C2}+\mathbf{Z}_{33}^{C3})\mathbf{U}_3+\mathbf{Z}_{43}^{C2}\mathbf{U}_4+\mathbf{Z}_{53}^{C3}\mathbf{U}_5=\mathbf{0},\\ \mathbf{Z}_{14}^{C1}\mathbf{U}_1+\mathbf{Z}_{24}^{C2}\mathbf{U}_2+\mathbf{Z}_{34}^{C2}\mathbf{U}_3+(\mathbf{Z}_{44}^{C1}+\mathbf{Z}_{44}^{C2}+\mathbf{Z}_{MPP})\mathbf{U}_4=\mathbf{0}\\ \mathbf{Z}_{25}^{C3}\mathbf{U}_2+\mathbf{Z}_{35}^{C3}\mathbf{U}_3-(\mathbf{Z}_{55}^{C3}+\mathbf{Z}_{MPPA})\mathbf{U}_5=\mathbf{0}\end{gathered} \tag{6.9}$$

in which $\mathbf{Z}_{MPP}$ and $\mathbf{Z}_{MPPA}$ are the condensed impedance matrix of the fully coupled MPP and the locally reacting MPP, respectively. The condensed velocity of the system with MPP can be solved as

$$\begin{bmatrix}\mathbf{U}_1\\ \mathbf{U}_2\\ \mathbf{U}_3\\ \mathbf{U}_4\\ \mathbf{U}_5\end{bmatrix} = -\mathbf{I}_{MPP}\begin{bmatrix}\mathbf{P}_e\\ \mathbf{0}\\ \mathbf{0}\\ \mathbf{0}\\ \mathbf{0}\end{bmatrix}, \tag{6.10}$$

where I_{MPP}^{-1} is written as

$$\begin{bmatrix} -\mathbf{Y}_1^{-1}+\mathbf{Z}_{11}^{C1} & \mathbf{0} & \mathbf{0} & -\mathbf{Z}_{41}^{C1} & \mathbf{0} \\ \mathbf{0} & \mathbf{Z}_{22}^{C2}+\mathbf{Z}_{22}^{C3}+\mathbf{Y}_2^{-1} & \mathbf{Z}_{32}^{C2}+\mathbf{Z}_{32}^{C3} & -\mathbf{Z}_{42}^{C2} & -\mathbf{Z}_{52}^{C3} \\ \mathbf{0} & \mathbf{Z}_{23}^{C1}+\mathbf{Z}_{23}^{C2} & \mathbf{Z}_{33}^{C1}+\mathbf{Z}_{33}^{C2} & -\mathbf{Z}_{43}^{C2} & -\mathbf{Z}_{53}^{C3} \\ -\mathbf{Z}_{14}^{C1} & -\mathbf{Z}_{24}^{C2} & -\mathbf{Z}_{34}^{C2} & \mathbf{Z}_{44}^{C1}+\mathbf{Z}_{44}^{C2}+\mathbf{Z}_{MPP} & \mathbf{0} \\ \mathbf{0} & -\mathbf{Z}_{25}^{C3} & -\mathbf{Z}_{35}^{C3} & \mathbf{0} & \mathbf{Z}_{55}^{C3}+\mathbf{Z}_{MPPA} \end{bmatrix}^{-1}.$$

6.2 Numerical Analyses

In this section, numerical results are presented and analyzed in terms of system response, sound insulation, energy transmission, and MPP effects. Then, similar analyses will be conducted for a DSF system with two floors. The acoustic properties of the system without MPP is studied first.

Dimensions of the system are shown in Figure 6.1. The length in the *x*-direction is 2.5m. The two glasses are assumed to be simply supported. The thickness of the outer glass and the inner glass are 18mm and 12mm, respectively. All boundaries are assumed to be acoustically rigid. The outer glass is subject to a diffused incident acoustic wave excitation as

$$p_d = \frac{1}{2\pi}\int_0^{2\pi}\int_0^{\frac{\pi}{2}} p_e d\theta_1\, d\theta_2 \tag{6.11}$$

6.2.1 System Response Predictions

The acoustic response in the system is first studied. Three sets of the result are presented in Figure 6.2. The SPL prediction results from the CTF model at a randomly selected point (0.6, 1.7, 2.4)m are shown in Figure 6.2a. The location is referred to as the local coordinate of the room. Recall that the mid-frequency is considered beginning at the modal overlap factor M=1, which is approximately 218Hz for the present room sub-system. Thus, the low-frequency result is obtained from the full CTF calculation. After entering the mid-frequency range, the piecewise scheme is used. The piecewise computational scheme is implemented within six one-third octave bands centered at 250Hz, 315Hz, 400Hz, 500Hz, 630Hz, and 800Hz, respectively. Similar treatment will be followed throughout this Chapter. Due to the inherent limitation of the FEM in terms of frequency outreach, only the low-frequency results can be validated against the FEM results, as shown in Figure 6.2a. It can be seen that all the resonance peaks are well predicted despite some inconsistencies at the anti-resonance frequencies and the level of some resonance peaks. The sound pressure level is integrated within one-third octave bands for reference, as shown in Figure 6.2b. Figure 6.2c plots the SPL distribution over the surface x = 0.6m at 400Hz. It can be seen that the acoustic field, as well as the contour lines, can be obtained, which allows further analyses and sound field optimizations. It is worth noticing that the information in Figure 6.2a and c can hardly be obtained when the room is modeled with the SEA.

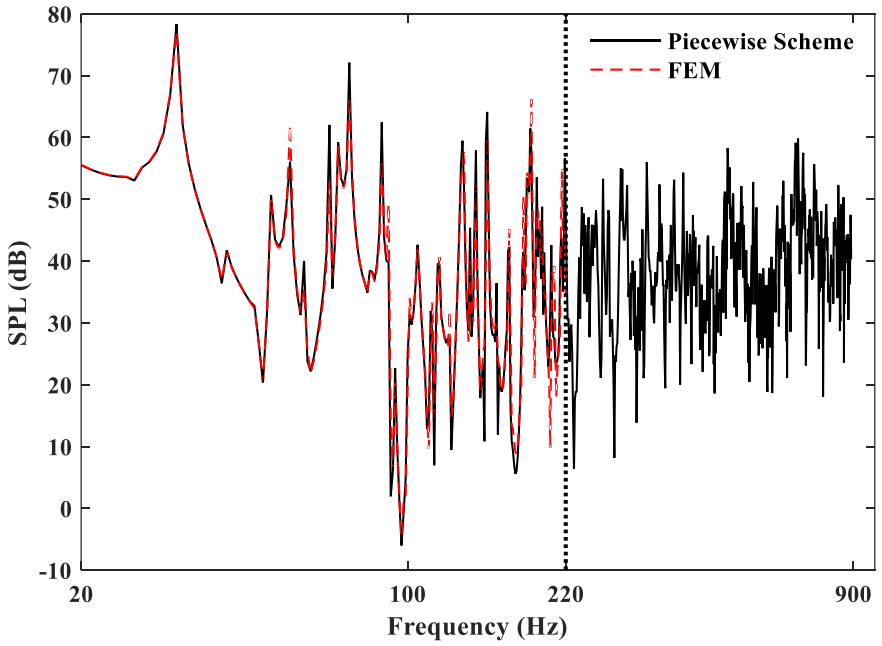
Piecewise Scheme
FEM
SPL (dB)
Frequency (Hz)
80
70
60
50
40
30
20
10
0
-10
20
100
220
900

(a)

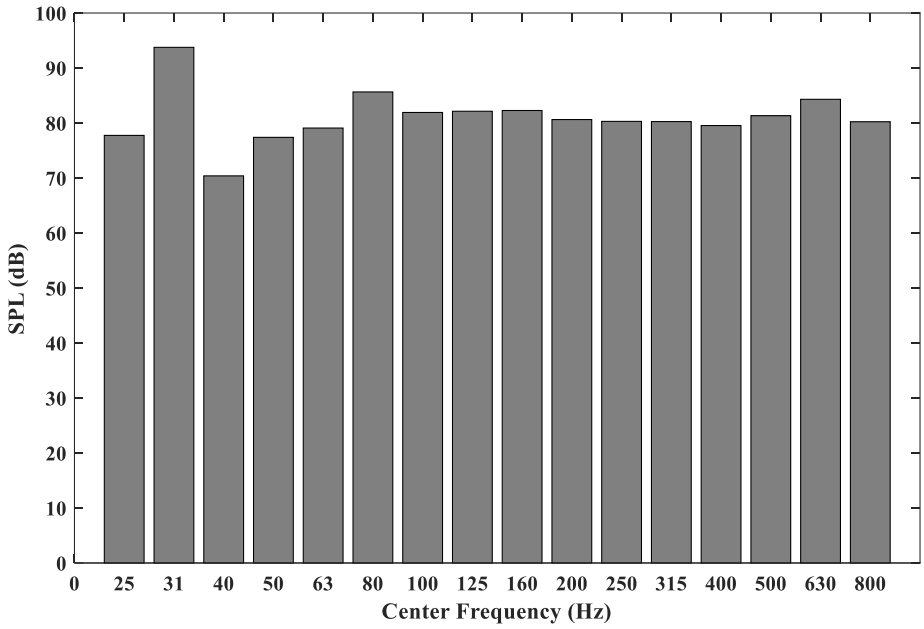
SPL (dB)
Center Frequency (Hz)
100
90
80
70
60
50
40
30
20
10
0
0
25
31
40
50
63
80
100
125
160
200
250
315
400
500
630
800

(b)

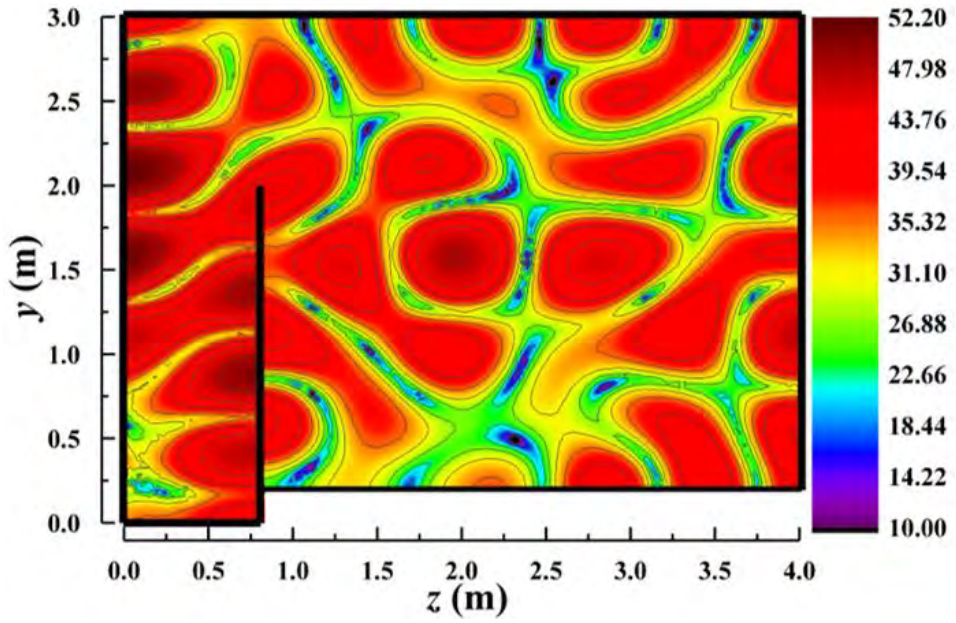

(c)

Figure 6.2 Acoustic response within the room structure: (a) SPL at a randomly selected receiving point (0.6, 1.7, 2.4) m, compared with the FEM results within the low-frequency range. (b) Equivalent sound pressure level inside the room within one-third octave bands. (c) SPL field map at a randomly cut surface x = 0.6 m, 400Hz.

The vibration responses of the two glasses are shown in Figure 6.3. Figure 6.3a shows the averaged square velocity $\widehat{U}_s$ of the glasses. Thanks to the orthogonality of the complex exponential functions used, this can be obtained as:

$$\widehat{U}_s = \frac{1}{S}\sum_n |\mathbf{U}_\alpha|^2 \tag{6.12}$$

where S is the area of the glass and α corresponds to the interface index of the glass shown in Figure 6.1.

It can be seen that the velocity difference between the two glasses is relatively small in the very low-frequency range since in this range the acoustic wavelength is much larger than the depth of the DSF cavity. In the mid-to-high frequency range, the velocity amplitude of the outer glass becomes larger than that of the inner glass. The

total energy of the two glasses, obtained from the summation of the potential energy and the kinetic energy, are integrated within one-third octave bands and shown in Figure 6.3b. It can be found the vibration energy of the outer glass is generally of a few orders of magnitude higher than that of the inner glass.

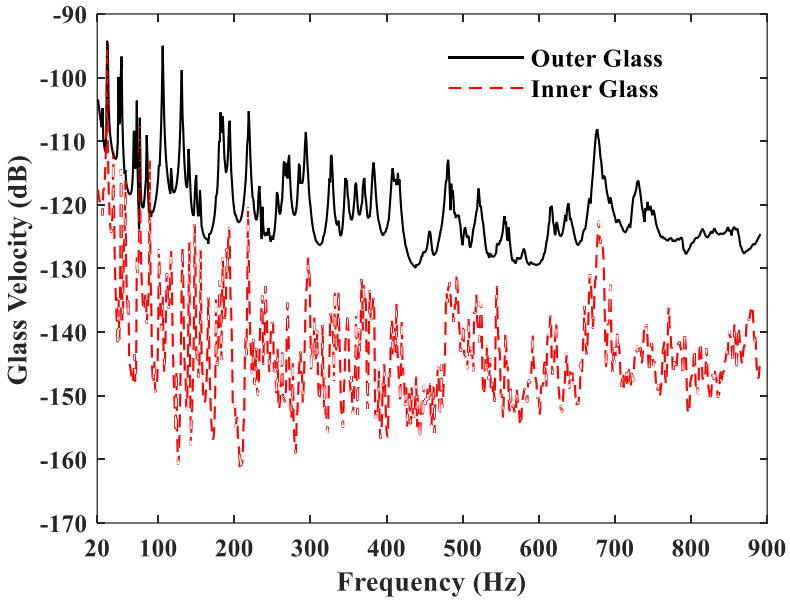

(a)

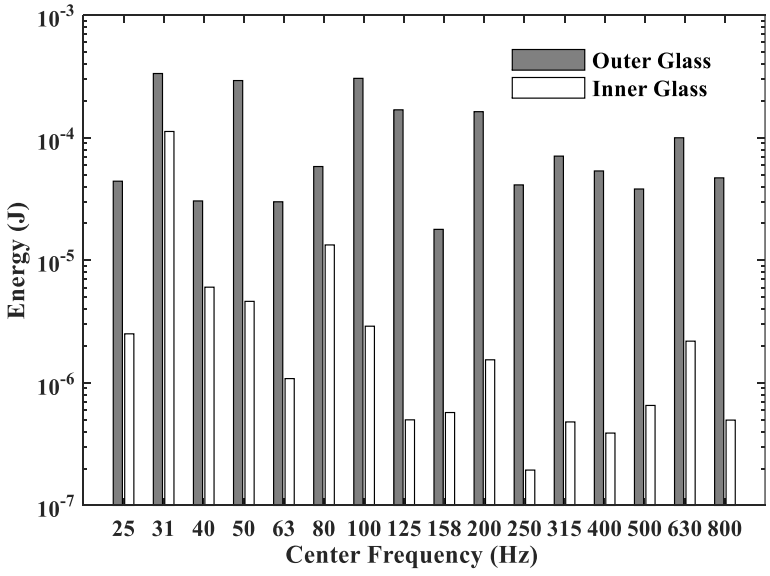

(b)

Figure 6.3 CTF predictions on the vibration response of two glass panels: (a) Squared velocity integrated over the glass surface with respect to frequency; (b) Total energy level (J) of the glass integrated within one-third octave frequency bands.

6.2.2 Sound Insulation

The SRI for the present configuration can be defined as:

$$SRI = 10\log_{10}\frac{\frac{1}{S}\int P^{e\,2}dS}{\frac{1}{V}\int p^2 dV}. \tag{6.13}$$

where S is the area of the outer glass and V is the volume of the room. Then, the SRI is calculated for two sets of glass damping ratio, 1%, and 10%, and shown in Figure 6.4a. It can be observed that generally an approximate 30dB sound reduction can be achieved by the present DSF structure except for the first few resonance frequencies of the outer glass, at which frequencies the SRIs are negative. A significant reduction in the SRI can be observed in Figure 6.4a at approximate 650Hz, which is the critical frequency of the outer glass. The critical frequency of the inner glass is beyond the current calculation frequency range. Within the mid-to-high frequency range, the panel with a 10% damping ratio introduces approximately 10dB general increase in the SRI compared with the 1% damping ratio case.

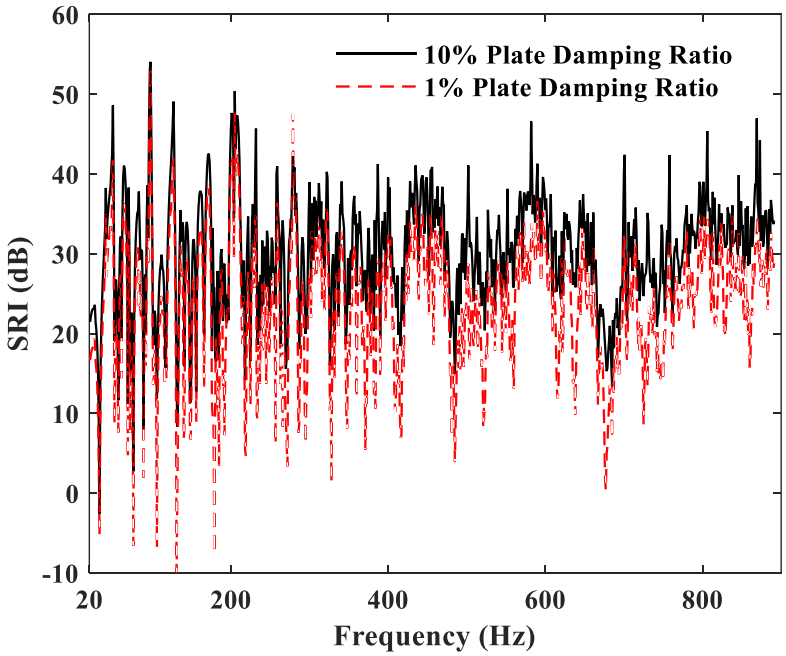

Figure 6.4 SRI prediction results for the simplified DSF system.

To further analyze the sound power transmitted into the room, the sound power transmitted through two different paths, *i.e.* ventilation opening and the inner glass, are compared. The transmitted sound power level L_w is obtained by integrating the sound intensity over the ventilation opening and the inner glass, respectively,

$$L_w = 10\log_{10}\frac{\int |I_z| dS}{10^{-12}}. \tag{6.14}$$

where I_z is the z-direction component of the sound intensity and S is the area of either the inner glass or the ventilation opening. Because the sound power level L_w is generally positive, we use L_w to represent the power going into the room (positive I_z) and $-L_w$ to represent the power out of the room (negative I_z). Figure 6.5a shows the power transmitted via the inner glass. Notice that the frequency in the x-axis is in log scale. The upper half of the figure (y>0) shows the frequencies at which the power flows into the room while the lower half (y<0) presents that out of the room. It can be seen that at some frequencies the power flows out of the room into the inner glass,

which can be attributed to the resonant effect of the glass. However, the power generally flows into the room via the ventilation opening except for a few low-frequency bands, as shown in Figure 6.5b. The total power transmitted into the room can be obtained by setting S in Eq. 6.14 as the summation of the glass and the ventilation opening, which is shown in Figure 6.5c.

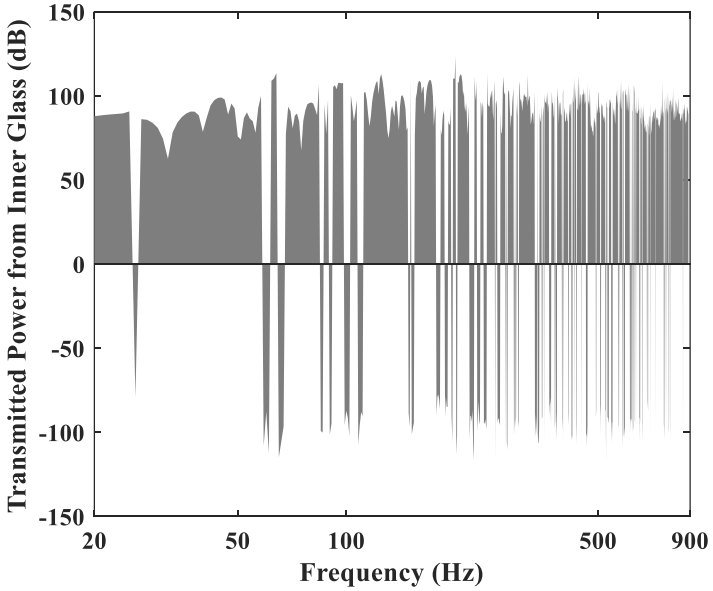

(a)

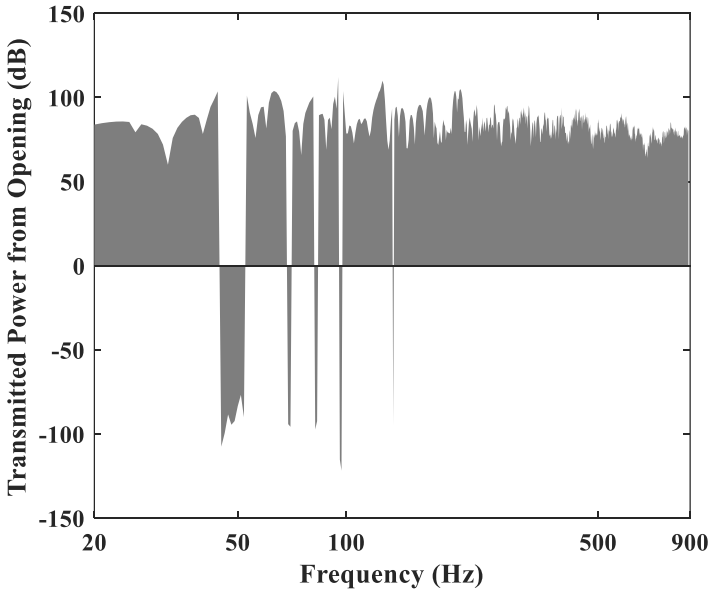

(b)

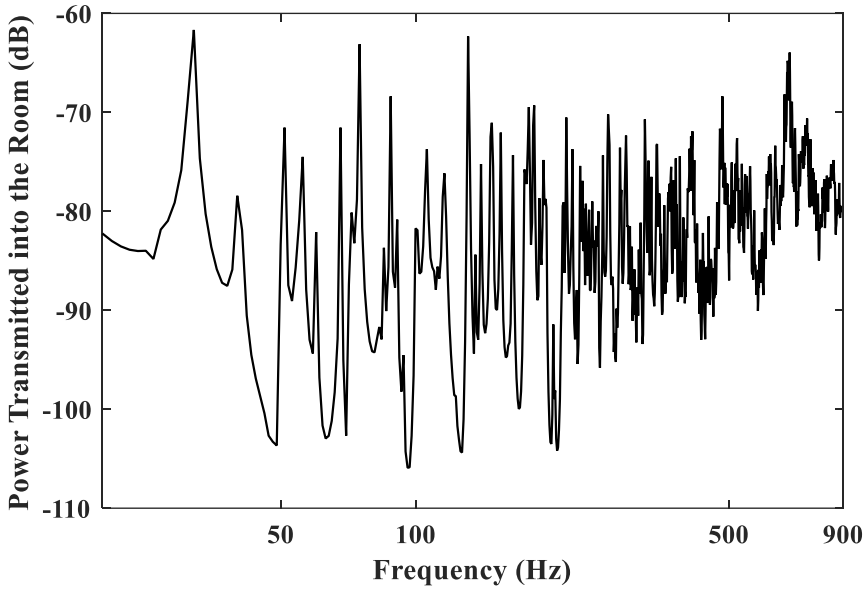

(c)

Figure 6.5 Transmitted power into the room from: (a) Inner glass; (b) Ventilation opening; (c) Inner glass plus ventilation opening.

From the above analyses, it can be confirmed that the power transmitted via the ventilation opening is more than that via the inner glass. Therefore, the transmissibility of the ventilation opening is further analyzed here, with respect to its size in the *y*-direction. Notice that the total height of the inner glass and the opening remains the same. Figure 6.6a and b present the SRI with respect to different opening sizes at 500 and 600Hz, respectively. It can be observed that when the ventilation opening size L_o is larger than the half wavelength of acoustic waves, the corresponding SRI fluctuates depending on the complex modal interaction between the DSF cavity and the room in the mid-to-high frequency range. When L_o becomes smaller than the half acoustic wavelength, the SRI exhibits obvious increase owing to the vanishing higher-order waves along the *y*-direction. Therefore, noise transmission through the opening starts to be dominant, as compared with its counterpart through the inner glass, when frequency increases up to a certain level.

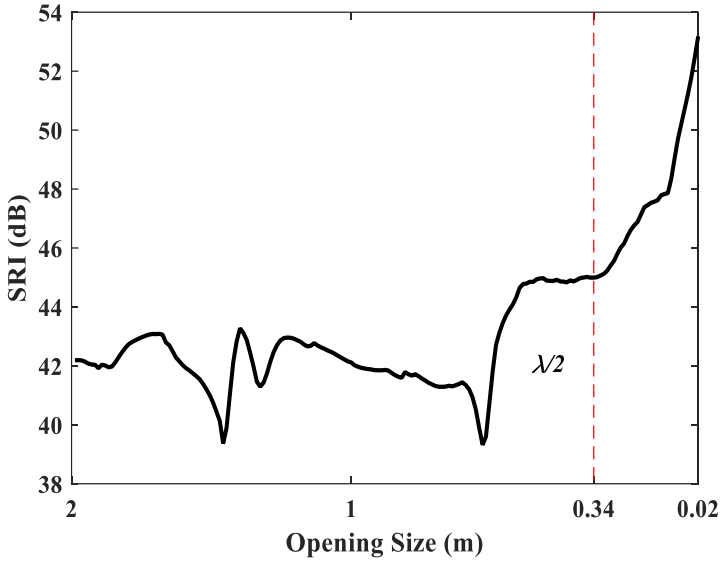

(a)

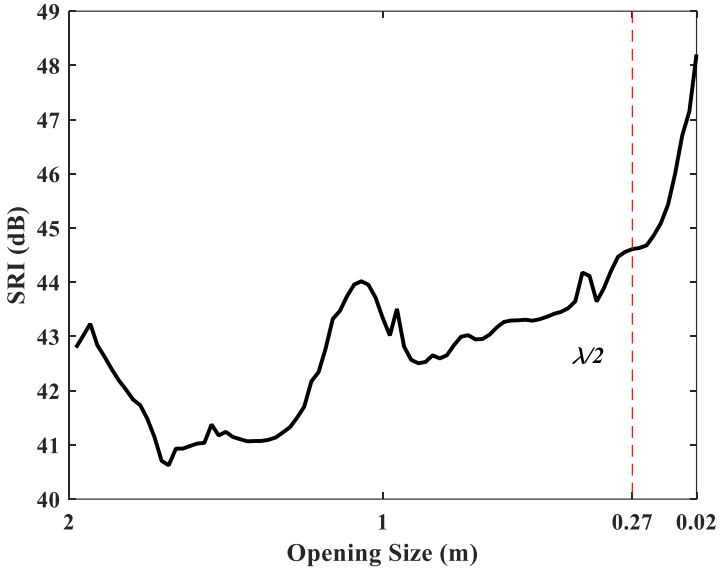

(b)

Figure 6.6 The influence of the opening size on the SRI at: (a) 500Hz; (b) 630Hz.

6.2.3 Analyses on the Micro-Perforated Panel

This section discusses the control performance and the location optimization of the MPP. According to the above analyses, efforts should be made at the frequencies

where the half acoustic wavelength is smaller than L_0, which is 212Hz for the present configuration. The parameters of the selected MPP are listed in Table 6.1.

Table 6.1 Parameters of the micro-perforated panel

Parameters	Hole diameter	Panel thickness	Perforation ratio	Depth of backing cavity
Value (Unit)	0.1 (mm)	0.1 (mm)	1%	0.1 (m)

For the locally reacting MPP, the absorption coefficient can be obtained by simply substituting the parameter in Table 6.1 into Eq. 6.5. For the MPP screen mounted within the DSF cavity, the absorption equation is not suitable anymore due to the existence of the ventilation opening. However, although it may not be reliable, the absorption coefficient of the fully coupled MPP can still be obtained for reference, by approximating the backing DSF cavity C2 as the cavity depth D in Eq. 6.5. The two absorption curves are shown in Figure 6.7. It can be seen the effective bandwidth of the two MPPs almost covers all the concerned frequencies.

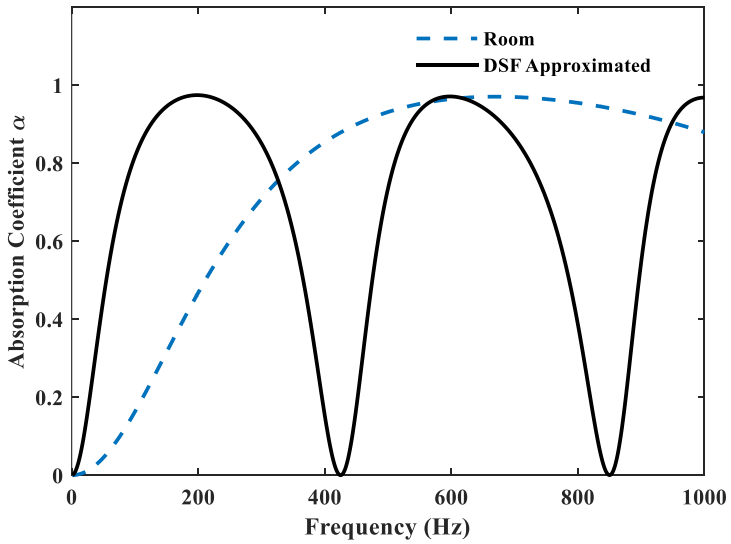

Figure 6.7 Absorption coefficient of the two MPP arrangements.

6.2.3.1 Performance Discussions

Figure 6.8a and b show the SPL response at a randomly selected point (0.6, 1.7, 2.4)m and the sound pressure integrated within the whole room, respectively. The results in Figure 6.8 include four different MPP arrangements, which are without MPP, with locally reacting MPP, with a fully coupled MPP screen, and with both. It can be observed that the SPL within the room is significantly reduced within the effective working bandwidth of the MPP. Obviously, using simultaneously the locally reacting MPP and the fully coupled MPP screen lead to the best noise reduction performance among the four cases. However, if only one MPP type is considered, it can be found that at low frequencies the performances of the two MPP arrangements are similar while at relatively high frequencies that of the locally reacting MPP is better, which is consistent with the evaluations from the absorption curve in Figure 6.7.

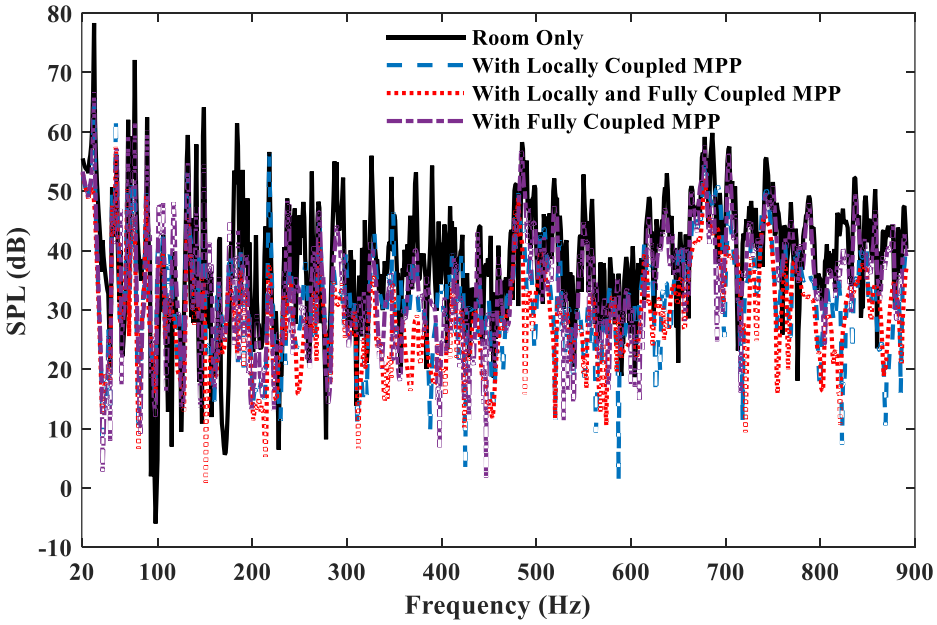

(a)

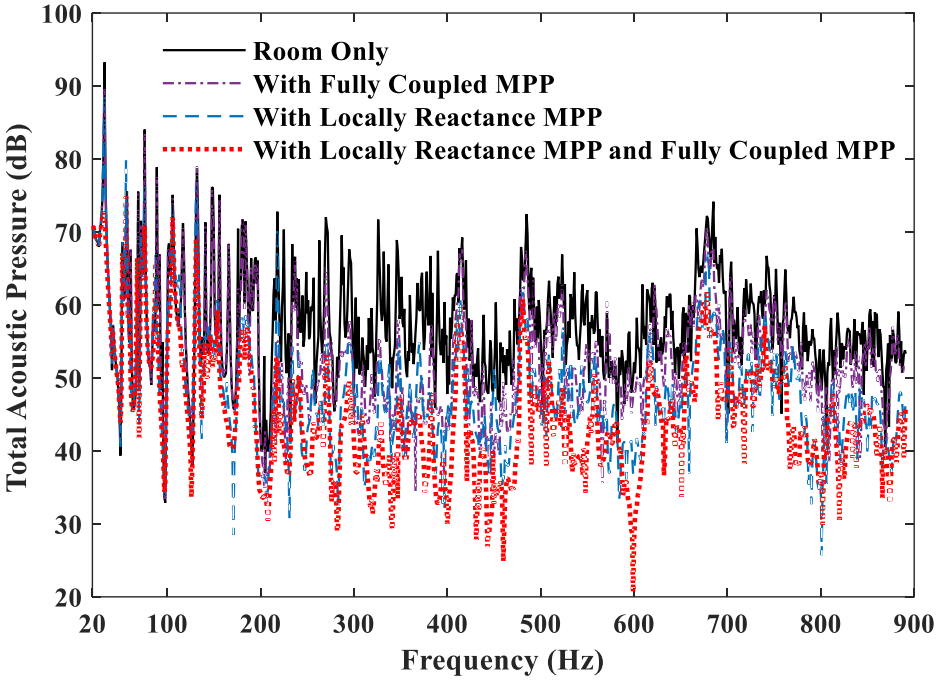

(b)

Figure 6.8 Performance of different MPP arrangements within the DSF system: (a) At a single point (0.6, 1.7, 2.4) m; (b) Total acoustic pressure within the room.

The influence of the locally reacting MPP on the sound pressure distribution within the room is analyzed. Figure 6.9a and b give the SPL distribution over a cut surface located at x = 0.6m, without and with the locally reacting MPP, respectively. To better compare the SPL difference, the two figures use the same color scale. It can be observed that the deployment of the MPP not only suppresses the SPL within the room but also change the whole sound pressure distribution, which can be confirmed by comparing the contour lines. Figure 6.9c shows the sound intensity distribution over the cut surface. It can be seen that the sound power indeed flows into the MPP surface, which illustrates the sound absorption capability of MPP. One also notices the absorption power of MPP is obviously much larger when it is close to the opening, consistent with one's intuition. This point is quantitatively studied in the next section.

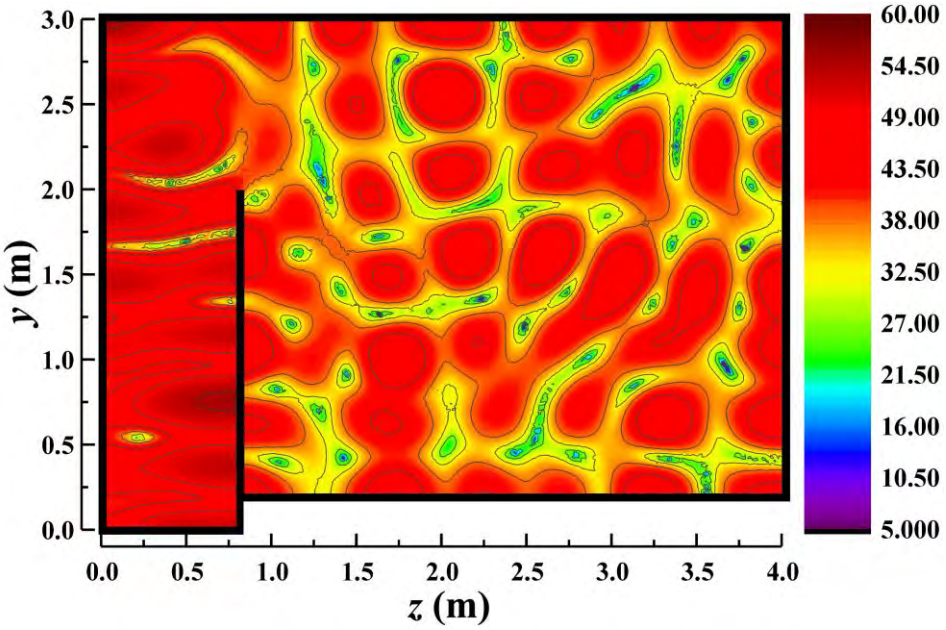
3.0
2.5
2.0
1.5
1.0
0.5
0.0
y (m)
0.0 0.5 1.0 1.5 2.0 2.5 3.0 3.5 4.0
z (m)
60.00
54.50
49.00
43.50
38.00
32.50
27.00
21.50
16.00
10.50
5.000

(a)

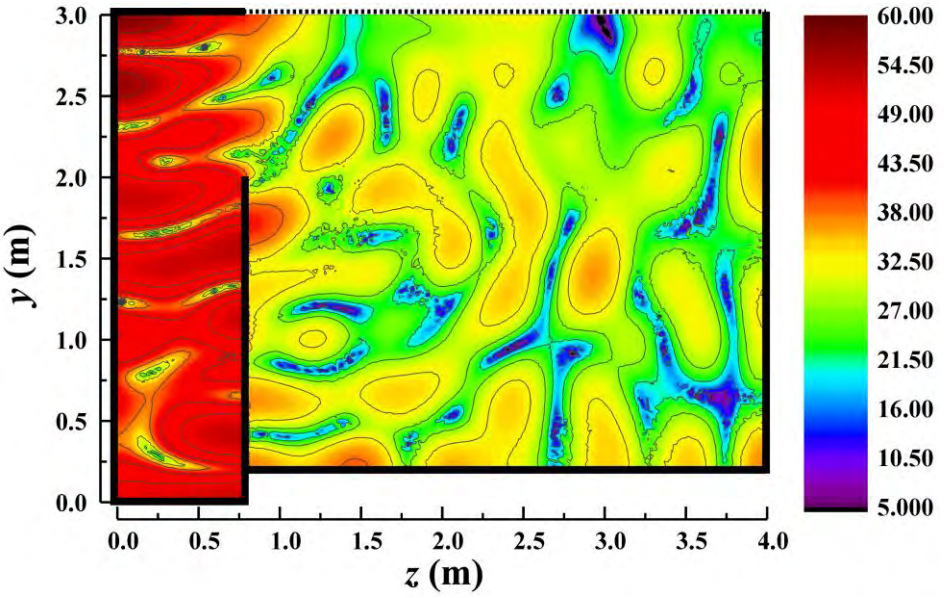
3.0
2.5
2.0
1.5
1.0
0.5
0.0
y (m)
0.0 0.5 1.0 1.5 2.0 2.5 3.0 3.5 4.0
z (m)
60.00
54.50
49.00
43.50
38.00
32.50
27.00
21.50
16.00
10.50
5.000

(b)

(c)

Figure 6.9 Mapping at the cut surface x = 0.6m, 530Hz: (a) SPL without MPPA; (b) SPL with locally reactance MPP over the ceiling; (c) Sound intensity within the room when locally reactance MPP is mounted.

Then, a similar comparison is made by considering both the locally reacting MPP and the fully coupled MPP screen. Different from the locally reacting MPP, the fully coupled MPP interacts with its surrounded acoustic environment and works when a pressure difference exists across the MPP. Figure 6.10 shows the performance of the fully coupled MPP screen at 400Hz. It can be observed that considerable SPL reduction can be further obtained on the basis of the existence of the locally reacting MPP. According to the equivalent absorption coefficient in Figure 6.7, the performance of the fully coupled MPP screen should have been poor at 400Hz. However, due to the interaction with the surrounding environment, the performance of the MPP screen cannot be simply evaluated from the absorption coefficient itself.

An evident pressure difference can be seen on the two sides of the MPP from y = 1m to y = 2m, which indicates the working mechanism of the fully coupled MPP screen.

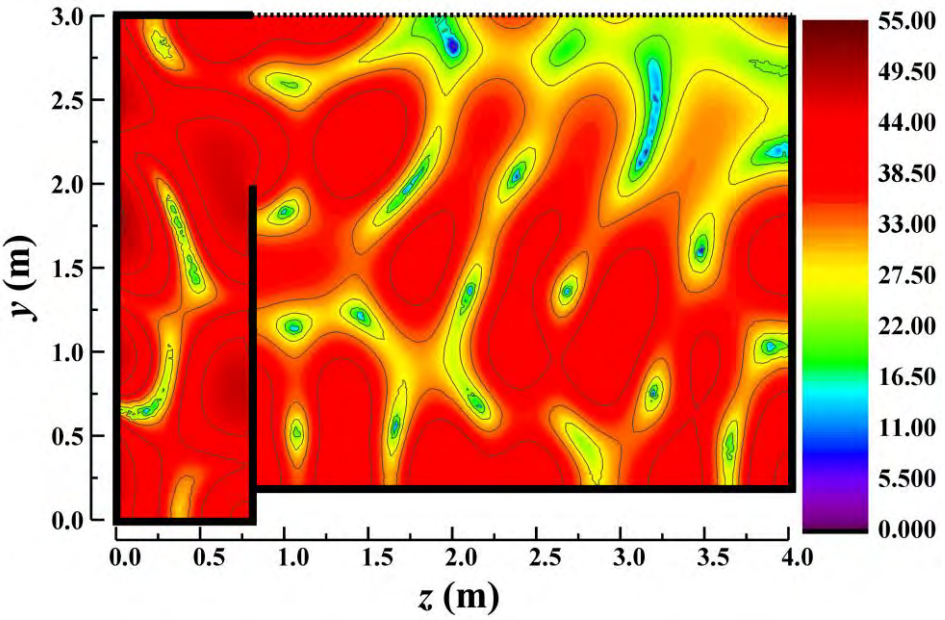

(a)

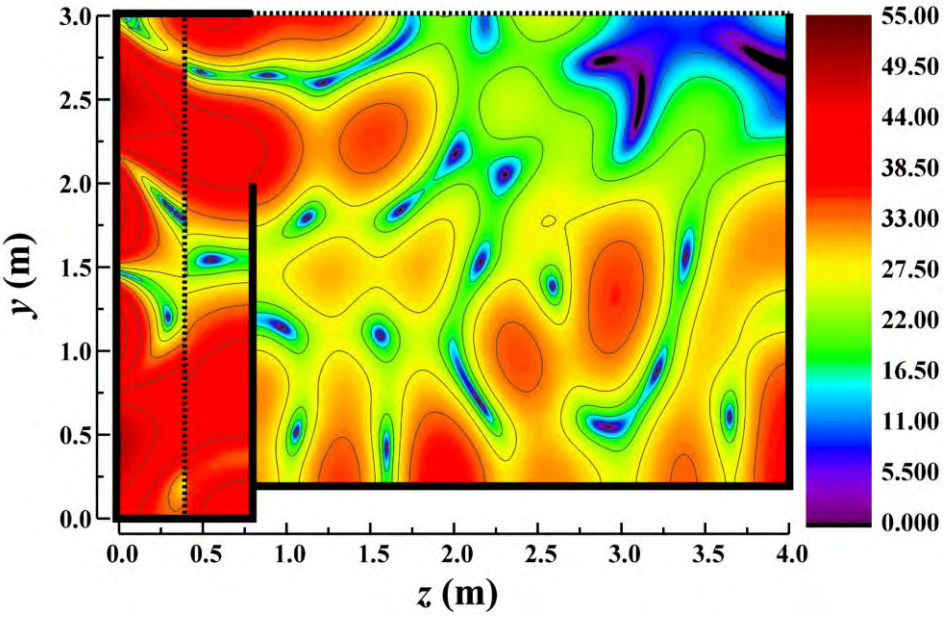

(b)

Figure 6.10 Mapping at the cut surface x = 0.6m, 329Hz: (a) SPL with locally reactance MPP; (b) SPL with locally reactance MPP and fully coupled MPP.

As a final remark, the SPL integrated within one-third octave bands of the four cases are shown in Figure 6.11. It is worth noticing that, for example within the 125Hz band, no SPL reduction is observed when only the fully coupled MPP screen is used. However, after the sound field is rebuilt by the locally reacting MPP, the fully coupled MPP could bring an extra suppression to the SPL. This implies the great design and optimization space offered by the MPP screen. Nevertheless, this needs to be conducted case by case and no generalized conclusions can be drawn here.

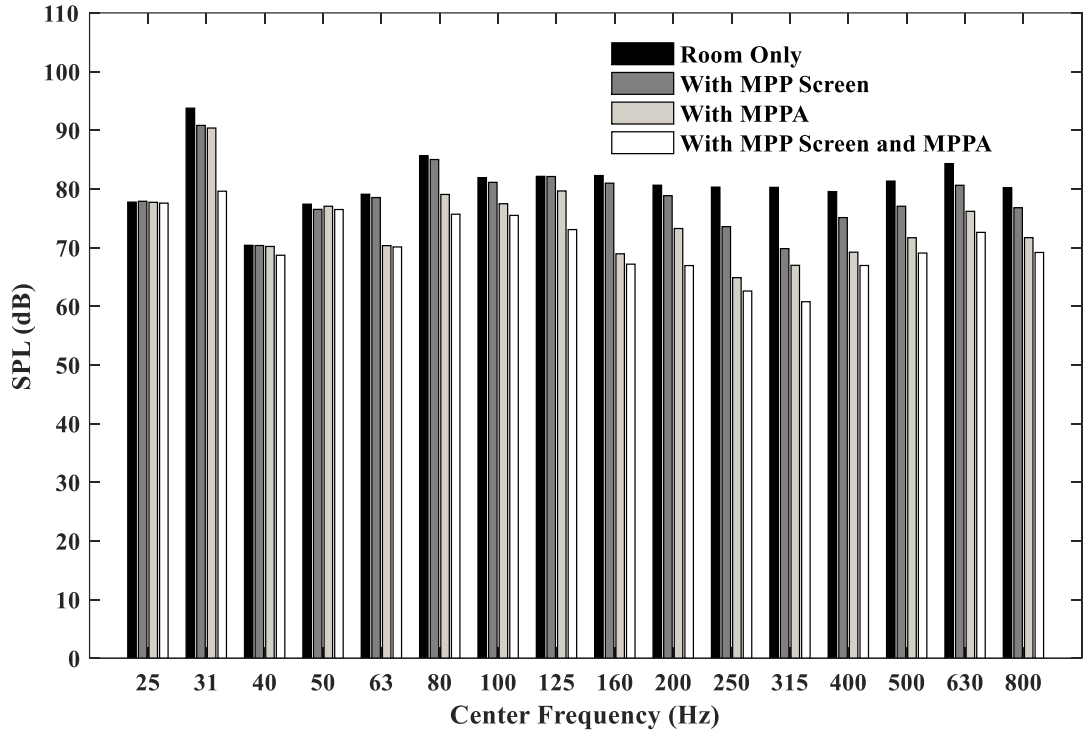

Figure 6.11 SPL within the room, integrated within one-third octave bands.

6.2.3.2 Arrangement Optimizations

To optimize the MPP arrangements, sound power absorption efficiency has to be evaluated first. For the locally reacting MPP, the absorption power is given by

integrating I_y over the MPP surface. For the fully coupled MPP, the absorption power can be calculated as

$$L_{wMPP} = \int (p_1 - p_2) u_{MPP} dS. \tag{6.15}$$

Furthermore, for the MPP screen, an equivalent absorption coefficient can be defined as

$$\alpha_{eq} = \int \frac{I_{z1} - I_{z2}}{I_{z1}} dS, \tag{6.16}$$

where I_{z1} and I_{z2} are the z-component of the sound intensity on the input side and the output side of the fully coupled MPP, respectively. The calculated α_{eq}, with and without the locally reacting MPP, are shown in Figure 6.12. It can be found that the absorption coefficient is higher in the low-frequency range, which is beyond the predicted working bandwidth of the MPP shown in Figure 6.7. This shows that the complex acoustic field, to which the MPP screen is exposed, creates a favorable working environment for MPP, thus promoting its in-situ sound absorption, which cannot be predicted by conventional sound absorption formula. This again confirms the effectiveness and design necessity of the MPP arrangement, with the aid of effective simulation tools like the one we developed.

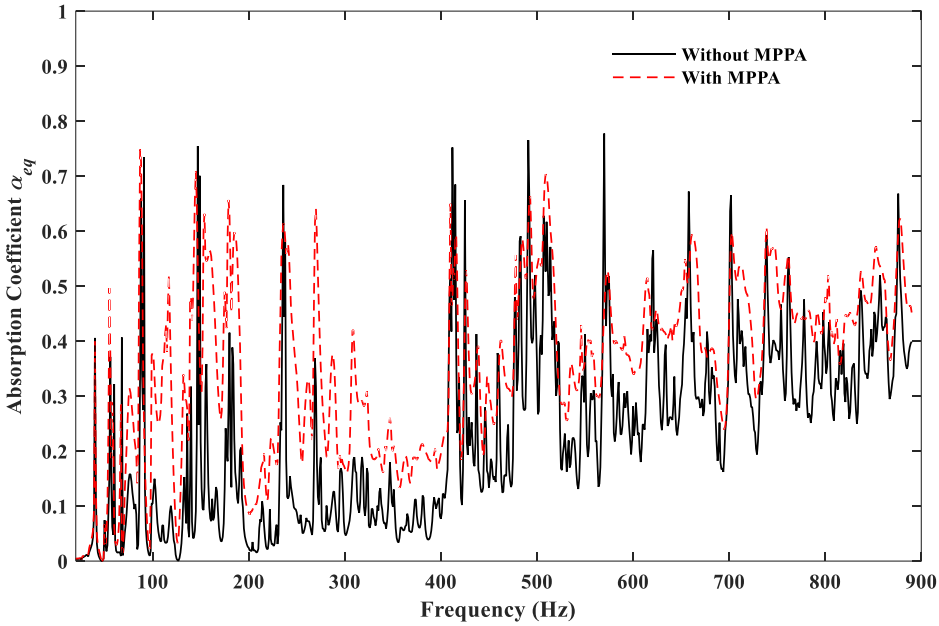

Figure 6.12 Equivalent absorption ratio of the fully coupled MPP screen.

For the current single layer insulation problems, attention should also be paid to the optimization of the locally reacting MPP. Because in practice, the available area over the ceiling is usually very limited. According to the sound intensity mapping in Figure 6.9c, mounting the MPP close to the ventilation opening seems to be a better choice. Therefore, the absorption efficiency along the z-direction is assessed by integrating the sound intensity I_y as

$$L_{wx} = \int_0^{L_x} I_y dx \ \left(\mathrm{W/m}\right). \tag{6.17}$$

To better reflect the general performance, L_{wz} is further integrated within four one-third octave frequency bands where the MPP absorption coefficient α is larger than 0.8. The results are shown in Figure 6.13. It can be seen that the absorption efficiency reaches a maximum at the opening and drops fast along with the distance in the depth direction of the room. The curves bounce back a little at the end of the room due to the intensification effect of the sound pressure [170]. Therefore, the MPP should better be mounted close to either the ventilation opening or the side walls.

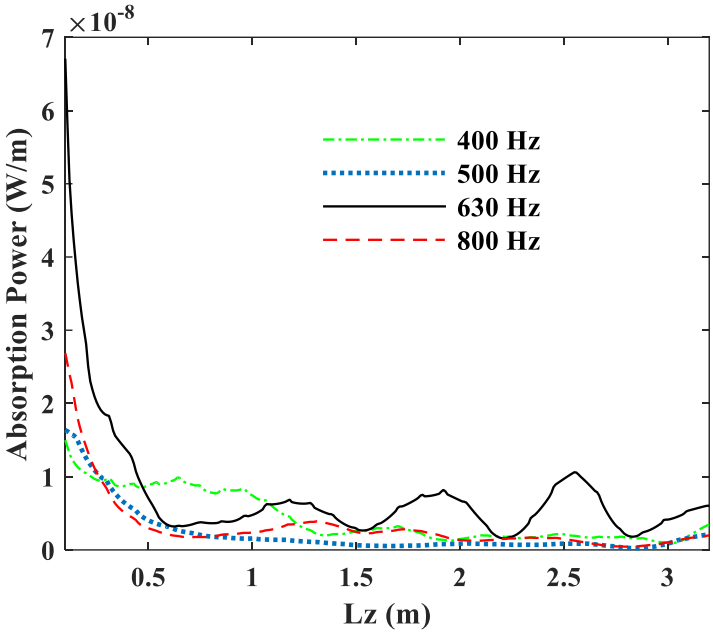

Figure 6.13 Absorption power efficiency of the locally reacting MPP along the depth direction (z-direction).

When MPPs of different working bandwidths are needed, the same analyses as in Figure 6.13 are conducted for MPPs of different parameters, of which the absorption coefficients are shown in Figure 6.14. The parameters of the other two MPPs are set to cover lower frequency ranges. L_{wz} for the selected MPPs are shown in Figure 6.15. Similar curve tendencies can be observed for the two different MPPs in Figure 6.15a and b, although the amplitude of the absorption power differs significantly.

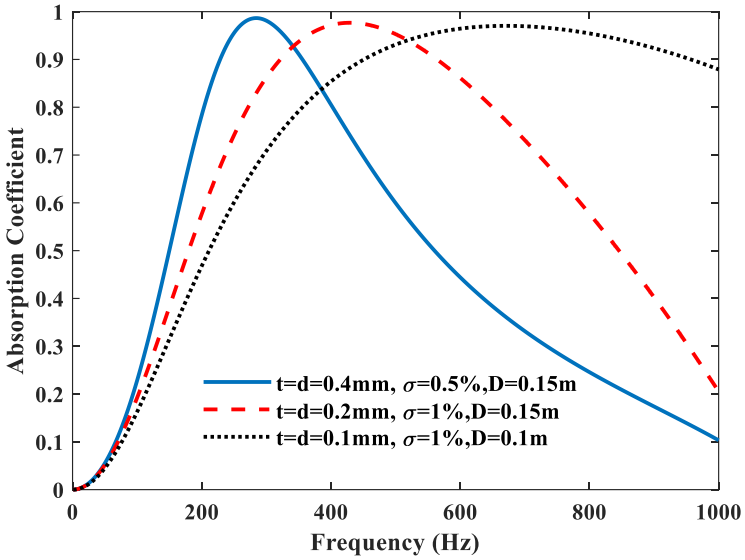

Figure 6.14 Parameters and the absorption coefficient of the selected MPP.

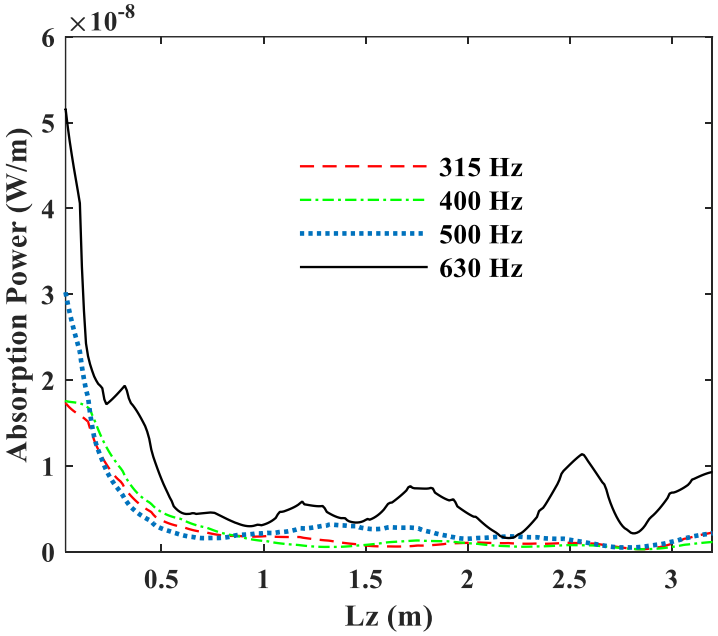

(a)

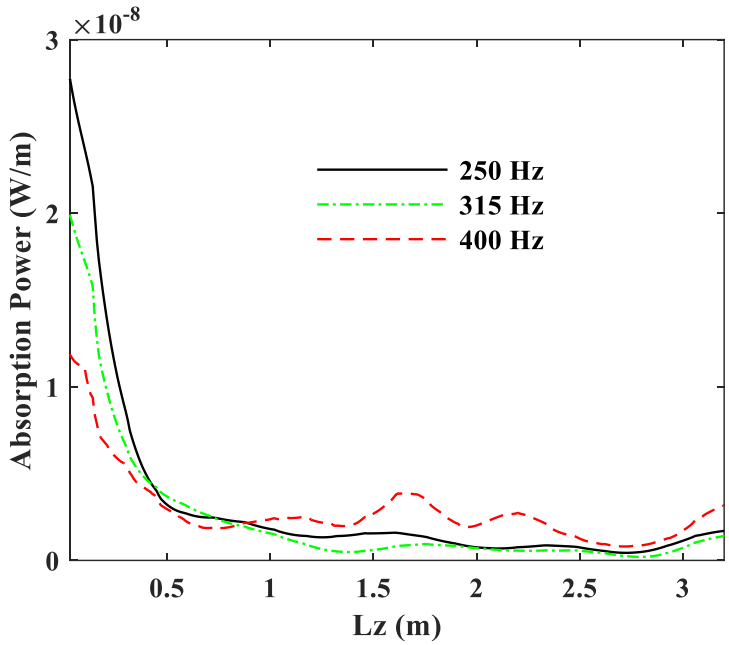

(b)

Figure 6.15 Absorption power efficiency of the locally reactance MPP along the depth direction (z-direction): (a) MPP 1; (b) MPP 2.

However, it is unrealistic to mount all MPPs close to the ventilation opening. To assess the influence of the location on the performance of different MPPs, the absorption power is integrated within all working bandwidth (α>0.8) and normalized with respect to the maximum value of each. The results are shown in Figure 6.16. It can be found that the absorption power, also can be noted as control efficiency, of the MPP with a higher working efficiency drops faster as the mounting distance becomes larger to the opening. This conclusion indicates that the MPPs of higher working frequencies should be mounted closer to the opening when the total available area is limited.

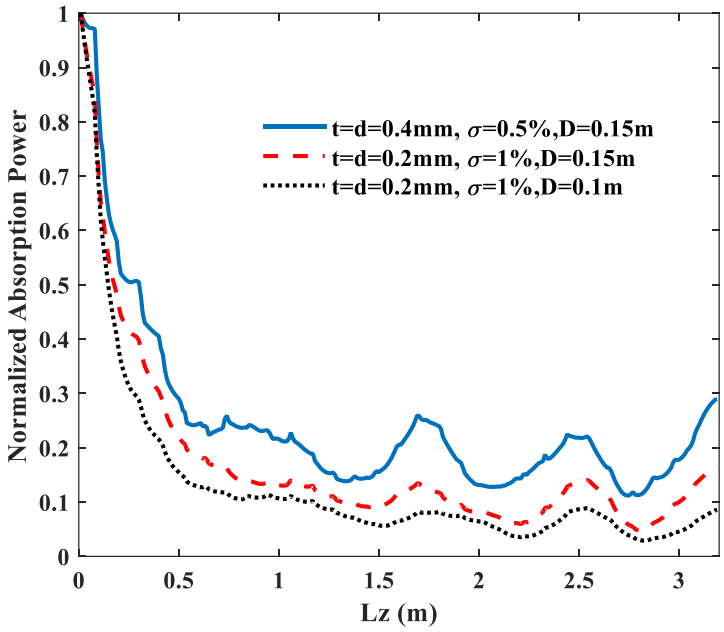

Figure 6.16 Normalized absorption power efficiency of the locally reacting MPP along the depth direction (z-direction).

6.2.4 Sound Transmissions between different floors

In this section, numerical analyses are conducted for a double floor configuration as shown in Figure 6.17, of which the height is twice that of the single floor DSF system in Figure 6.1. Other dimensions in x-axis and z-axis remain the same. The only sound transmission path between the two floors is the DSF cavity in this case. A sound source of $0.1m^3/s$ volume velocity is located at (0.6, 1.6, 2)m of the lower floor and a receiver is at (0.3, 1,7, 2)m of the upper floor. Because the following results only serve for the exhibition of computational capability in a more complex system, attentions are only focused on the sound field predictions. The notations in Figure 6.17 is for writing the CTF equations of the double floor configuration, which are presented in the Appendix.

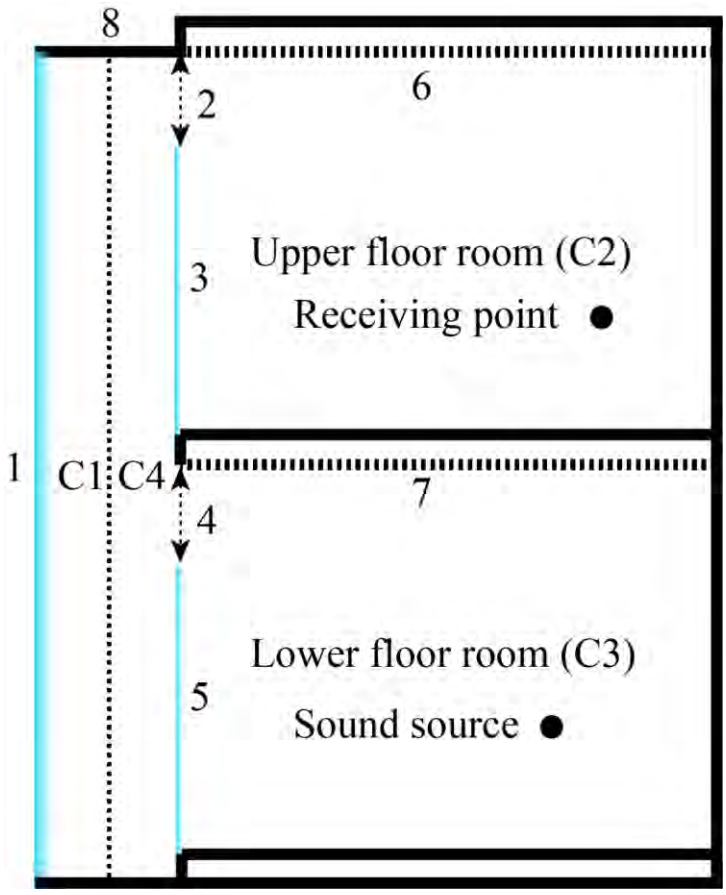

Figure 6.17 Sound transmission through the DSF cavity: double floor configuration.

The calculated SPL at the receiving point and volume integrated SPL are shown in Figure 6.18a and b, respectively. It can be observed that an approximately 20dB SPL reduction can be achieved in the effective working frequencies of the MPP. Comparing with the single floor case, one finds that the MPP has a better performance in reducing the airborne noise than dealing with the structure-borne noise.

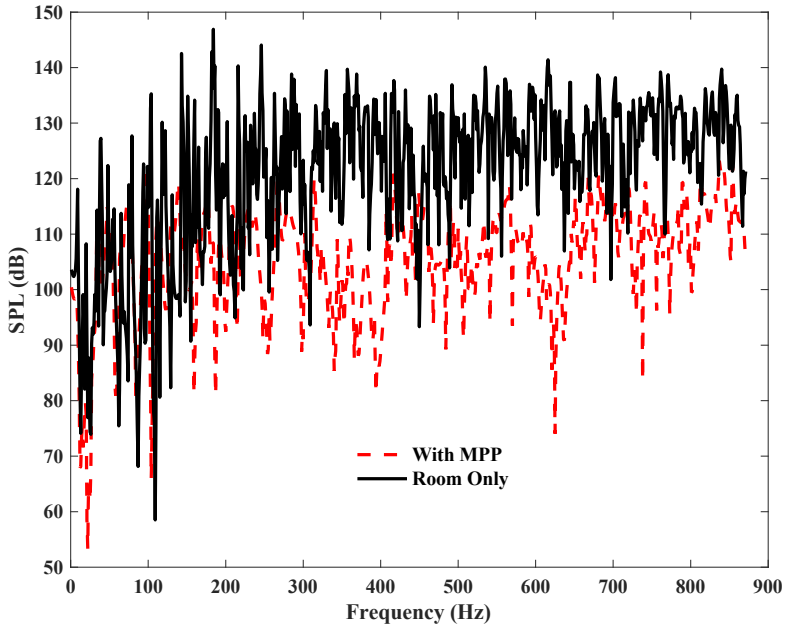

(a)

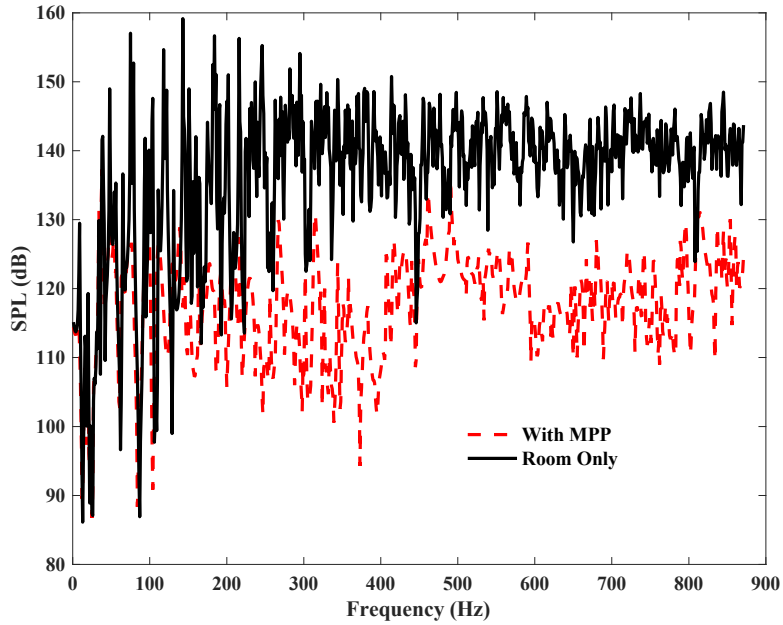

(b)

Figure 6.18 SPL predictions in double floor configuration: (a) At point (0.3, 1,7, 2)m of the upper room; (b) Volume integrated within the upper room.

Figure 6.19 compares the difference in SPL distribution with and without MPP arrangements. It can be observed that the MPP can significantly reduce the received SPL on the upper floor. In Figure 6.19b, the effectiveness of the fully coupled MPP screen can be confirmed by comparing the pressure difference on its two sides.

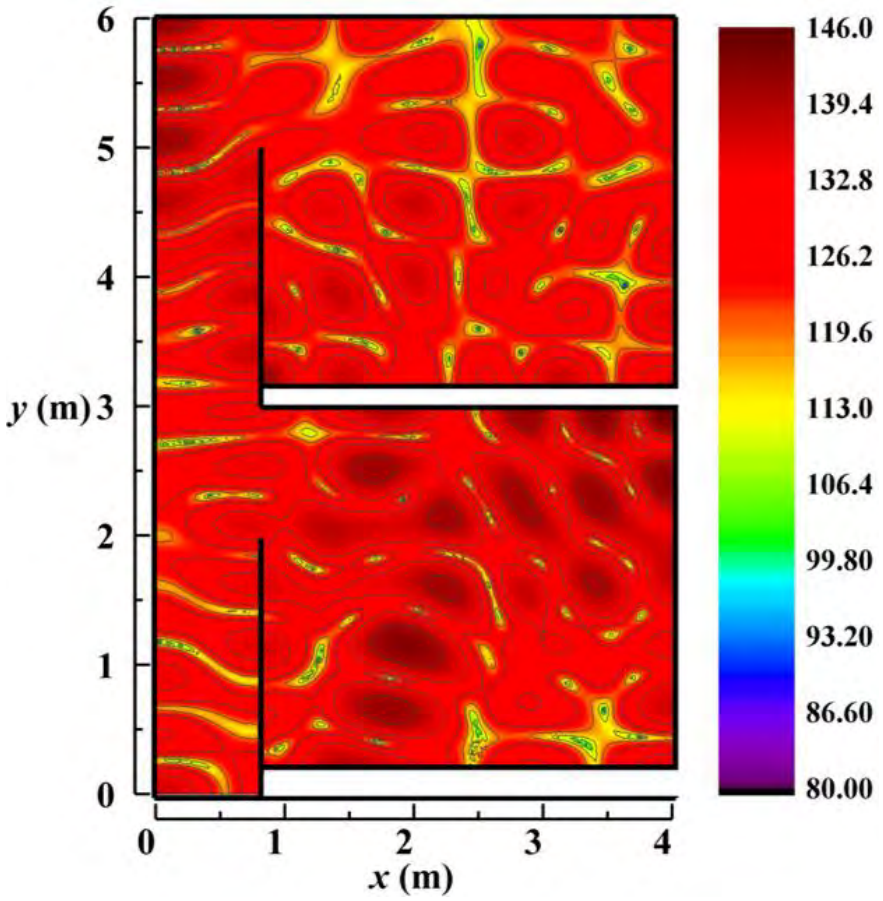

(a)

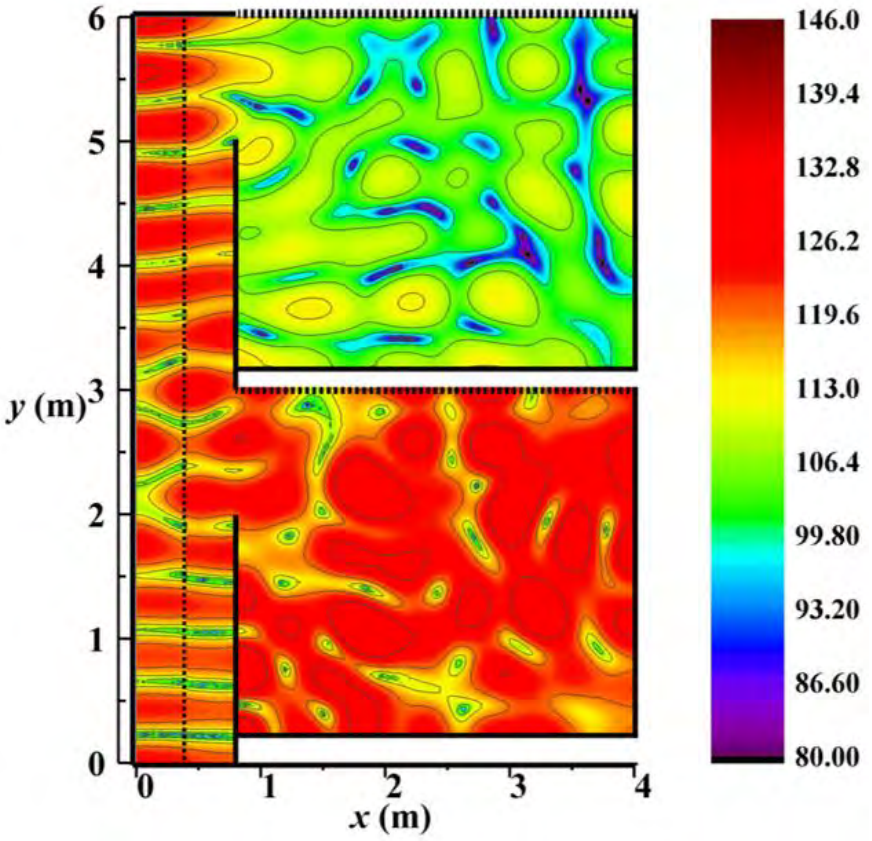

(b)

Figure 6.19 SPL field and contours at 400Hz: (a) Room only; (b) With locally reacting and fully coupled MPP.

6.2.5 Efficiency Comparisons

As a final remark, the calculation efficiency improvement by the piecewise scheme compared with the full calculation is summarized in Table 6.2. 2D modeling is also listed for reference because it is a common simplification in building acoustics. It can be seen the piecewise scheme can significantly reduce the element number of the assembled condensed impedance matrix. The higher the frequency band concerned is, the more evident the improvement is.

Table 6.2 Calculation efficiency comparisons between the piecewise scheme and the full calculation

Matrix Size Reduction (%)	Center Frequency (Hz)					
	315	400	500	630	800	1000
2D Simplified	-	39.5	49.0	56.4	61.6	68.5
Single Floor	21.8	31.3	40.7	44	48.2	50
Single Floor MPP	27.8	34.5	39.1	43.6	45.8	49.1
Double Floor	22.5	33.2	42.2	45.1	49.6	50.4
Double Floor MPP	26.6	34.8	41.1	44.7	46.9	49.2

6.3 Summary

In this chapter, a simplified DSF system is thoroughly studied using the proposed simulation method in terms of frequency responses, sound insulation performance, energy transmission path, and the noise mitigation performance as well as the underlying physical mechanism using MPPs. It is shown that the proposed modeling methodology allows a fine and detailed description of this type of complex vibro-acoustic system with relatively complex dynamics and a large dimension in the entire frequency range including the mid-to-high one.

The parametric study shows that the sound insulation capability of the DSF system is highly dependent on the size of the ventilation opening. For the single-layer DSF sound insulation problem, the ventilation opening dominates the sound power transmission process in a relatively high-frequency range. The SRI significantly

increases in the low-frequency range when the size of the ventilation opening becomes smaller than the half acoustic wavelength.

It is found that the MPP could effectively reduce the SPL within the room. By analyzing the energy absorption efficiency of the MPP with different parameters, arrangement suggestions are given to achieve better noise control performance for a given problem. The MPPs of higher working bandwidth should be mounted closer to the opening when the total available area is limited.

It is concluded that the piecewise scheme is less computation-intensive and demanding in terms of computation capability and calculation time than the full CTF calculation. The later can be regarded as among the traditional sub-structure or interface model reduction methods.

CHAPTER 7 Conclusions and Future Works

This thesis proposed a CTF approach for the vibro-acoustic system modeling, based on which a piecewise computational scheme was developed to increase the mid-to-high frequency modeling efficiency. This chapter highlights the major work that has been accomplished and the main contributions and conclusions obtained from the analyses. Finally, recommendations on the possible improvement of the method and future works are presented.

7.1 Summary

In Chapter 2, two benchmark solutions for a plate-cavity system, modal method, and wave method are revisited. The controversy and skepticisms surrounding the velocity continuity problem of the modal method were clarified. It is shown that the modal-based decomposition method allows correct prediction of both the acoustic pressure and the acoustic velocity inside an acoustic cavity covered by a flexural structure upon using appropriate series truncation criterion. The acoustic pressure prediction using modal method can be sufficiently accurate, throughout the cavity including vibrating interface as long as a sufficient number of cavity modes (prescribed by the pressure convergence criterion) are used, in agreement with the common understanding reported in the literature. The conventionally used pressure criterion, however, cannot guaranty the velocity prediction accuracy, especially when the calculation point is close to the vibrating structure, due to the inherent properties of the modal shape functions. Nevertheless, numerical studies reveal an oscillating

convergence pattern of the acoustic particle velocity with the increase of the decomposition terms in the cavity depth direction. More specifically, for a given calculation point, the calculated particle velocity using modal approach first monotonously approaches to the exact value with a relatively small but increasing number of terms, overshoots and then converges to the exact solution in an oscillating manner, starting roughly from the generalized mode number G = 1. For a given distance from the vibrating plate, the modal series in the cavity depth direction should be truncated up to G = 1.5, 2.5, 3.5… etc. Explained using the series decomposition theories and verified in both 1D and 3D configurations, the proposed velocity truncation criterion requires the use of all these lower-order modes in the cavity depth direction, whose 3/4 wavelengths are larger than the distance between the calculation point and the vibrating plate, to ensure a good prediction accuracy for the particle velocity. Therefore, when both the pressure criterion and the proposed velocity convergence rule are satisfied, a fast convergence of the particle velocity can be achieved.

Chapter 3 presents the basic theory behind the CTF method. A benchmark model consisting of a plate-cavity system is used to illustrate the approach. The rightness of the model is validated through comparisons with the modal solutions. Three types of function are tested as the condensation functions (CFs), which are gate functions, complex exponential functions, and Chebyshev polynomials, respectively. The convergence conditions of the three types of function are revealed. It is concluded that the method can effectively predict the system response, either in a point by point manner or in terms of the total energy level of the whole system.

Based on the theoretical CTF framework, Chapter 4 reveals a piecewise convergence behavior of the complex exponential functions, enabling a model reduction for the mid-to-high frequency simulations. This unique property of the complex exponential functions is attributed to their wavy feature and spatial matching with the dynamics of the physical system. Based on that, a series selection criterion for the complex exponential CFs is proposed to further increase the calculation efficiency. Given a targeted frequency band $[f_l, f_h]$, all complex exponential CFs φ_{pq} with their wavelengths $\lambda_{c,pq}$ delimited by $\alpha\lambda_h < \lambda_{c,pq} < \beta\lambda_l$ are kept to form a subset, to be used in the calculation. It has been shown that using α=1 and β=1.5 can guarantee an acceptable prediction accuracy in most of the analyzed cases. Calculation errors might be larger in some frequency bands but still within the tolerance level typically required for mid-to-high frequency modeling. The most significant advantage of the proposed criterion is that it allows accurate modeling of the system in a piecewise manner in terms of frequency bands with a much-reduced model and at a reduced calculation cost.

Chapter 5 extends the application range of the piecewise computational scheme to strong coupling cases. The coupling strength is defined by examining the acoustic response differences over the coupling interface before and after the attached sub-system is added. A coupling strength factor Ω is proposed to quantify the coupling strength in the context of a multi-degree freedom system and mid-to-high frequency range. It is found that the proposed coupling strength factor Ω can well reflect the variation trends of the coupling strength between two coupled sub-systems, as reflected by the acoustic response differences over the coupling interface. Factors which affect the coupling strength between two acoustic sub-cavities are volume ratio,

interface modal matching level, and the frequency. Similar quantification can also be achieved for structural-acoustic coupled systems. By comparing the value of Ω, the coupling strength of the cavity-cavity system is shown to be generally much stronger than that of the plate-cavity system. On the other hand, the piecewise computational scheme is shown to be effective and accurate enough in the modeling of a strongly coupled acoustic cavity. Without losing the efficiency and compromising its accuracy, the proposed scheme allows a detailed sound field description. The computational error is found to be increased when the coupling strength becomes stronger, which, nevertheless, is still within the normal tolerance level in terms of the mid-to-high frequency modeling. For a given system and a prescribed frequency band, the computational error of the piecewise computational scheme can be approximately evaluated from Ω. If the error is over what is expected, one can consider a larger β when truncating the CF series. Experimental validations are conducted in a strongly coupled acoustic cavity for both full CTF calculation and the piecewise computational scheme.

The established piecewise computational scheme is then applied to a simplified DSF system, as a practical application. The system is thoroughly studied using the proposed simulation method in terms of frequency responses, sound insulation performance, energy transmission path, and the noise mitigation performance as well as the physical mechanism using MPPs. It is shown that the proposed modeling method allows a fine and detailed description of this complex vibro-acoustic system with relatively complex dynamics and a large dimension in the entire frequency range including the mid-to-high one. For the single-layer DSF sound insulation problem, it is found that the transmitted power through the ventilation opening is more than that

through the inner glass. For a given configuration, the SRI is relatively high at low-frequency range when the half acoustic wavelength is larger than the size of the ventilation opening, which can be attributed to the absence of the higher-order waves. For higher frequencies, the half acoustic wavelength is smaller than the size of the ventilation opening. The SRI is relatively small and fluctuates due to the complex interactions between the room and the DSF cavity. It is found that the MPP could considerably reduce the SPL within the room. By analyzing the energy absorption efficiency of the MPP with different parameters, arrangement suggestions are given to achieve better noise control performance for a given problem. Finally, the computational efficiency of the piecewise computational scheme is shown. It is concluded that the piecewise scheme is less computation-intensive and demanding in terms of computation capability and calculation time than the full CTF calculation. The later can be regarded as among the traditional sub-structure or interface model reduction methods.

7.2 Main Conclusions

Main conclusions are summarized as follows.

- For the benchmark Plate-cavity problem, the acoustic pressure prediction using modal method can be sufficiently accurate, throughout the cavity including vibrating interface as long as a sufficient number of cavity modes are used. Using all these lower-order modes in the cavity depth direction, whose 3/4 wavelengths are larger than the distance between the calculation point and the vibrating plate, can ensure a good prediction accuracy for the acoustic particle velocity.

- The proposed CTF modeling approach allows the use of condensation functions, which can be either discrete functions of continuous functions. The proposed CTF method can effectively predict the system response, either in a point by point manner or in terms of the total energy level of the whole system. Impedance, mobility and the interface velocity can be properly described with only a few dominated terms if the selected function shape could match the interface deformation of the two coupled sub-systems.

- As a further improvement of the CTF approach for the mid-to-high frequency modeling, a piecewise computational scheme is proposed based on complex exponential functions, which allows a good balance between the computational efficiency and accuracy. To deal with systems with a various degree of coupling strength, a coupling strength factor is defined to quantify the coupling strength between two multi-degree-of-freedom sub-systems in the mid-to-high frequency context. The piecewise computational scheme is then shown to be effective and applicable to systems with increasing coupling strength. The computational error is found to increase when the coupling strength becomes stronger, which, nevertheless, is still within the normal tolerance level in terms of the mid-to-high frequency modeling.

- The piecewise scheme is shown to be effective in dealing with complex coupled systems, exemplified by a simplified DSF structure. For a typical DSF configuration, the partial ventilation opening is found be to the main path for sound transmission. The transmissibility through it significantly increases

when its size becomes larger than the half acoustic wavelength. As a typical noise mitigation measure, locally reacting MPP and fully coupled MPPA are shown to be effective for room noise control. In particular, MPP should be mounted as closely as possible to the opening, for the targeted higher frequency range.

7.3 Recommendations and Future Works

This thesis proposed a mid-to-high frequency method. The completed works mainly focus on how to select and truncate the interface condensation functions in a given system and frequency band, in order to increase the computational efficiency while preserving the wealth of the information that can be provided. However, there are two major challenges faced at present in terms of the condensation functions. Firstly, most numerical analyses and the experimental validations are conducted based on rectangular sub-systems and idealized boundaries. Practical structures usually have irregular shapes and complex boundary conditions. Although theoretically the proposed piecewise computational scheme can be extended to spherical or cylindrical coordinate following the same procedure, there are still some cases where the coordinate separation might be extremely difficult. The selected condensation functions should be improved to adapt to the system accordingly.

The other challenge arises in dealing with the systems where the interface deformation wavelengths are not uniform. Typical examples include a stiffened plate or a tapered plate. In these cases, the complex exponential functions may not be able to match the interface wavy feature anymore. Although there are a large number of

works focusing on the modeling of such plates, how to adopt these models to the present method is still pending to be studied.

The uncertainty in the system within the mid-to-high frequency range could be another concern which warrants future studies. As reviewed in Chapter 1, short-wavelength sub-systems are more sensitive to the small imperfections and manufacturing error when frequency increases. All these inevitable elements, which are also difficult, if not impossible, to quantify, are among the so-called uncertainty parameters.

Two other types of uncertainties that are commonly accepted are classified as parametric and non-parametric uncertainties, respectively. For the parametric uncertainties, they can be described by the probability distribution functions. In light of the uncertainty propagation theory, it is reasonable to surmise that the influence caused by the uncertainty can be captured by the complex exponential functions based on the analyses conducted in this thesis. As for the non-parametric uncertainties, it is more challenging to include them in the piecewise computational framework. Gate functions are one possible choice to tackle the problem. As stated in Chapter 3, the condensed impedance of the gate functions can be obtained from either a theoretical model or an experimental test. Considering a coupled system in which one sub-system is deterministic and the other is uncertain. FEM or modal methods can be used to obtain the condensed impedance matrix over the interface of the deterministic sub-system. For the uncertain sub-system, experimental measurements can be conducted gate by gate. The measurement points should follow the half-wavelength principle. The uncertainties which cannot be captured by such measurement can be considered as negligible.

Appendix

A.1 Integral Results

The integration between the complex exponential functions and the system modes are given here. Because the integral in *x* and *y* directions are symmetrical, only the integral in the *y* direction is shown.

A.1.1 Integral of a Plate

For a simply supported rectangular plate, the integral is written as

$$\int_0^{L_y} \sin(\frac{m_y \pi y}{L_y}) \exp(j \frac{s \pi y}{L_y}) dy. \quad \text{A.1}$$

The output depends on the value of m_y and *r*. The possible results are listed below:

- When $s = 0$, $\int_0^{L_y} \sin(\frac{m_y \pi y}{L_y}) \exp(j \frac{s \pi y}{L_y}) dy = \frac{L_y}{m_y \pi} [1 - (-1)^{m_y}]$.
- When $s = m_y$, $\int_0^{L_y} \sin(\frac{m_y \pi y}{L_y}) \exp(j \frac{s \pi y}{L_y}) dy = \frac{j L_y}{2}$.
- When $s = -m_y$, $\int_0^{L_y} \sin(\frac{m_y \pi y}{L_y}) \exp(j \frac{s \pi y}{L_y}) dy = -\frac{j L_y}{2}$
- Otherwise, the integral is given by

  $\int_0^{L_y} \sin(\frac{m_y \pi y}{L_y}) \cos(\frac{s \pi y}{L_y}) dy = \frac{1}{2\pi} [\frac{-L_y}{(m_y + s)} * [(-1)^{m_y + s} - 1] + \frac{L_y}{(m_y - s)} [(-1)^{m_y - s} - 1]$.

A.1.1 Integral of a Cavity

For an acoustic cavity, the results are a bit more complex. Taking the *y*-direction of the ventilation opening in Chapter 6 as an example, the configuration along the *y*-axis is shown in Figure A.1. Notice the opening can be any sub-section on the *y*-axis.

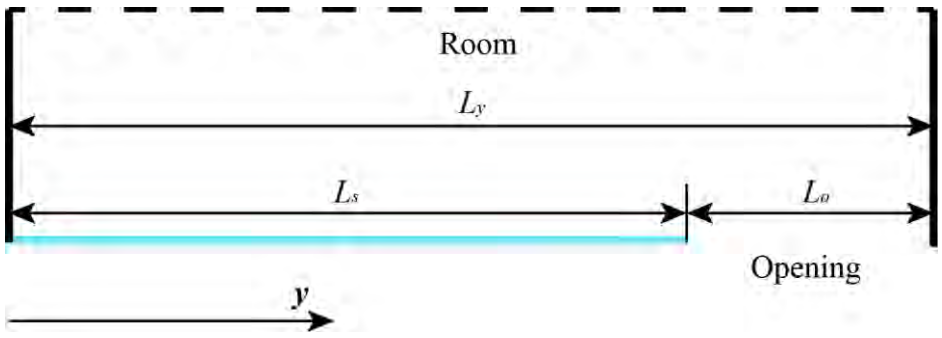

Figure A.1 Illustration on the acoustic mode and the complex exponential function.

Then, the integral is written as:

$$\int_{L_s}^{L_s+L_o} \cos\left(\frac{n_y \pi y}{L_y}\right) \exp\left[j \frac{s\pi(y-L_s)}{L_o}\right] dy. \quad \text{A.2}$$

The output depends on the value of n_y, s, L_y, and L_o. The possible results are listed below:

- When $n_y = r = 0$, $\int_{L_s}^{L_s+L_o} \cos\left(\frac{n_y \pi y}{L_y}\right) \exp\left[j \frac{s\pi(y-L_s)}{L_o}\right] dy = L_o$.
- When $sL_y = n_y L_o$, the real part is given by

$$\int_{L_s}^{L_s+L_o} \cos\left(\frac{n_y \pi y}{L_y}\right) \cos\left[\frac{s\pi(y-L_s)}{L_o}\right] dy = \frac{1}{2} y \cos\left(\frac{n_y \pi L_s}{L_y}\right) - \frac{L_y}{4 n_y \pi} \left[\sin\left(\frac{n_y \pi}{L_y}(L_s - 2y)\right)\right]\Bigg|_{L_s}^{L_s+L_o} = \frac{1}{2} L_o \cos\left(\frac{n_y \pi L_s}{L_y}\right) + \frac{L_y}{4 n_y \pi}\left[\sin\left(\frac{n_y \pi}{L_y}(L_s + 2L_o)\right) - \sin\left(\frac{n_y \pi L_s}{L_y}\right)\right],$$

and the imaginary part is given by

$$\int_{L_s}^{L_s+L_o}\cos(\frac{n_y\pi y}{L_y})\sin[j\frac{s\pi(y-L_s)}{L_o}]dy=\frac{1}{2}y\sin\left(\frac{n_y\pi L_s}{L_y}\right)-\frac{L_y}{4n_y\pi}\cos[\frac{n_y\pi}{L_y}(L_s-$$

$$2y)]\Big|_{L_s}^{L_s+L_o}=\frac{1}{2}L_o\sin\left(\frac{n_y\pi L_s}{L_y}\right)-\frac{L_y}{4n_y\pi}\left[\cos\left(\frac{n_y\pi}{L_y}(L_s+2L_o)\right)+\cos\left(\frac{n_y\pi L_s}{L_y}\right)\right].$$

- Otherwise, the real part is given by

$$\int_{L_s}^{L_s+L_o}\cos(\frac{n_y\pi y}{L_y})\cos[\frac{s\pi(y-L_s)}{L_o}]\,dy=\frac{L_yL_o}{2\pi}\left[\frac{1}{sL_y+n_yL_o}\sin[\frac{s\pi L_y(y-L_s)+n_y\pi L_oy}{L_yL_o}]+\right.$$

$$\left.\frac{1}{sL_y-n_yL_o}\sin[\frac{s\pi L_y(y-L_s)-n_y\pi L_oy}{L_yL_o}]\right]\Big|_{L_s}^{L_s+L_o}=\frac{n_yL_0^2L_y}{\pi(n_y^2L_0^2-s^2L_y^2)}[(-1)^s\sin\left(\frac{n_y\pi(L_s+L_o)}{L_y}\right)-$$

$$\sin\left(\frac{n_y\pi L_s}{L_y}\right)],$$

and the imaginary part is given by

$$\int_{L_s}^{L_s+L_o}j\cos(\frac{n_y\pi y}{L_y})\sin[\frac{s\pi(y-L_s)}{L_o}]dy=\frac{jL_yL_o}{2\pi}\left[\frac{1}{sL_y+n_yL_o}\cos[\frac{s\pi L_y(y-L_s)+n_y\pi L_oy}{L_yL_o}]+\right.$$

$$\left.\frac{1}{sL_y-n_yL_o}\cos[\frac{s\pi L_y(y-L_s)-n_y\pi L_oy}{L_yL_o}]\right]\Big|_{L_s}^{L_s+L_o}=\frac{jsL_y^2L_0}{\pi(n_y^2L_0^2-s^2L_y^2)}[(-1)^s\cos\left(\frac{n_y\pi(L_s+L_o)}{L_y}\right)-$$

$$\cos\left(\frac{n_y\pi L_s}{L_y}\right)].$$

A.2 CTF Model of the Double Layer DSF System

The configuration of the system can be referred to as Fig. 6.18. When the MPP is absent, the force equilibrium equations of the five interfaces are:

$$-(\mathbf{Y}_1^{-1}+\mathbf{Z}_{11}^{C1})\mathbf{U}_1+\mathbf{Z}_{21}^{C1}\mathbf{U}_2+\mathbf{Z}_{31}^{C1}\mathbf{U}_3+\mathbf{Z}_{41}^{C1}\mathbf{U}_4+\mathbf{Z}_{51}^{C1}\mathbf{U}_5=\mathbf{0},$$

$$\mathbf{Z}_{12}^{C1}\mathbf{U}_1-(\mathbf{Z}_{22}^{C1}+\mathbf{Z}_{22}^{C2})\mathbf{U}_2-(\mathbf{Z}_{32}^{C1}+\mathbf{Z}_{32}^{C2})\mathbf{U}_3-\mathbf{Z}_{42}^{C1}\mathbf{U}_4-\mathbf{Z}_{52}^{C1}\mathbf{U}_5=\mathbf{0},$$

$$\mathbf{Z}_{13}^{C1}\mathbf{U}_1-(\mathbf{Z}_{23}^{C1}+\mathbf{Z}_{23}^{C2})\mathbf{U}_2-(\mathbf{Z}_{33}^{C1}+\mathbf{Z}_{33}^{C2}+\mathbf{Y}_3^{-1})\mathbf{U}_3-\mathbf{Z}_{43}^{C1}\mathbf{U}_4-\mathbf{Z}_{53}^{C1}\mathbf{U}_5=\mathbf{0},$$

$$\mathbf{Z}_{12}^{C1}\mathbf{U}_1-\mathbf{Z}_{24}^{C1}\mathbf{U}_2-\mathbf{Z}_{33}^{C1}\mathbf{U}_3-(\mathbf{Z}_{44}^{C1}+\mathbf{Z}_{44}^{C3})\mathbf{U}_4-(\mathbf{Z}_{54}^{C1}+\mathbf{Z}_{54}^{C3})\mathbf{U}_5=\mathbf{P}_4,$$

$$\mathbf{Z}_{15}^{C1}\mathbf{U}_1-\mathbf{Z}_{25}^{C1}\mathbf{U}_2-\mathbf{Z}_{35}^{C1}\mathbf{U}_3-(\mathbf{Z}_{45}^{C1}+\mathbf{Z}_{45}^{C3})\mathbf{U}_4-(\mathbf{Z}_{55}^{C1}+\mathbf{Z}_{55}^{C3}+\mathbf{Y}_5^{-1})\mathbf{U}_5=\mathbf{P}_5,$$

in which $\mathbf{P}_4$ and $\mathbf{P}_5$ are the blocked pressure vector in the condensation functions coordinate. For the present case, they are decomposed in terms of the complex exponential functions.

With the locally reacting MPP walls and the fully coupled MPP screen taken into account, the force equilibrium equations of the seven interface are:

$$-(\mathbf{Y}_1^{-1} + \mathbf{Z}_{11}^{C1})\mathbf{U}_1 + \mathbf{Z}_{81}^{C1}\mathbf{U}_8 = \mathbf{0},$$

$$(\mathbf{Z}_{22}^{C4} + \mathbf{Z}_{22}^{C2})\mathbf{U}_2 + (\mathbf{Z}_{32}^{C4} + \mathbf{Z}_{32}^{C2})\mathbf{U}_3 + \mathbf{Z}_{42}^{C4}\mathbf{U}_4 + \mathbf{Z}_{52}^{C4}\mathbf{U}_5 + \mathbf{Z}_{62}^{C2}\mathbf{U}_6 - \mathbf{Z}_{82}^{C4}\mathbf{U}_8 = \mathbf{0},$$

$$(\mathbf{Z}_{23}^{C4} + \mathbf{Z}_{23}^{C2})\mathbf{U}_2 + (\mathbf{Z}_{33}^{C4} + \mathbf{Z}_{33}^{C2} + \mathbf{Y}_3^{-1})\mathbf{U}_3 + \mathbf{Z}_{43}^{C4}\mathbf{U}_4 + \mathbf{Z}_{53}^{C4}\mathbf{U}_5 + \mathbf{Z}_{62}^{C2}\mathbf{U}_6 - \mathbf{Z}_{82}^{C4}\mathbf{U}_8 = \mathbf{0},$$

$$\mathbf{Z}_{24}^{C4}\mathbf{U}_2 + \mathbf{Z}_{34}^{C4}\mathbf{U}_3 + (\mathbf{Z}_{44}^{C4} + \mathbf{Z}_{44}^{C3})\mathbf{U}_4 + (\mathbf{Z}_{54}^{C4} + \mathbf{Z}_{54}^{C3})\mathbf{U}_5 + \mathbf{Z}_{74}^{C3}\mathbf{U}_7 - \mathbf{Z}_{84}^{C4}\mathbf{U}_8 = \mathbf{P}_4,$$

$$\mathbf{Z}_{25}^{C4}\mathbf{U}_2 + \mathbf{Z}_{35}^{C4}\mathbf{U}_3 + (\mathbf{Z}_{45}^{C4} + \mathbf{Z}_{45}^{C3})\mathbf{U}_4 + (\mathbf{Z}_{55}^{C4} + \mathbf{Z}_{55}^{C3} + \mathbf{Y}_5^{-1})\mathbf{U}_5 + \mathbf{Z}_{75}^{C3}\mathbf{U}_7 - \mathbf{Z}_{85}^{C4}\mathbf{U}_8 = \mathbf{P}_5\,,$$

$$\mathbf{Z}_{26}^{C2}\mathbf{U}_2 + \mathbf{Z}_{36}^{C2}\mathbf{U}_3 = (\mathbf{Z}_{66}^{C2} + \mathbf{Z}_{MPPA})\mathbf{U}_6,$$

$$\mathbf{Z}_{47}^{C3}\mathbf{U}_4 + \mathbf{Z}_{57}^{C3}\mathbf{U}_5 + \mathbf{P}_7 = (\mathbf{Z}_{77}^{C3} + \mathbf{Z}_{MPPA})\mathbf{U}_7,$$

$$\mathbf{Z}_{18}^{C1}\mathbf{U}_1 - \mathbf{Z}_{28}^{C4}\mathbf{U}_2 - \mathbf{Z}_{38}^{C4}\mathbf{U}_3 - \mathbf{Z}_{48}^{C4}\mathbf{U}_4 - \mathbf{Z}_{58}^{C4}\mathbf{U}_5 = (\mathbf{Z}_{88}^{C1} + \mathbf{Z}_{88}^{C4} + \mathbf{Z}_{MPP})\mathbf{U}_8.$$

References

[1] E.H. Dowell, G.F. Gorman, and D.A. Smith, "Acoustoelasticity: General theory, acoustic natural modes and forced response to sinusoidal excitation, including comparisons with experiment,″ Journal of Sound and Vibration **52**(4), 519-542 (1977).

[2] F.J. Fahy and P. Gardonio, *Sound and structural vibration: radiation, transmission and response*. 2007: Academic press.

[3] M. Petyt, *Introduction to finite element vibration analysis*. 2010: Cambridge university press.

[4] B. Pluymers, W. Desmet, D. Vandepitte, and P. Sas, "Application of an efficient wave-based prediction technique for the analysis of vibro-acoustic radiation problems,″ Journal of Computational and Applied Mathematics **168**(1-2), 353-364 (2004).

[5] R.H. Lyon, *Theory and application of statistical energy analysis*. 2014: Elsevier.

[6] F.J. Fahy, "Statistical energy analysis: a critical overview,″ Philosophical Transactions of the Royal Society of London A: Mathematical, Physical and Engineering Sciences **346**(1681), 431-447 (1994).

[7] A. Le Bot, *Foundation of statistical energy analysis in vibroacoustics*. 2015: OUP Oxford.

[8] A. Le Bot and V. Cotoni, "Validity diagrams of statistical energy analysis,″ Journal of Sound and Vibration **329**(2), 221-235 (2010).

[9] R.S. Langley and P. Bremner, "A hybrid method for the vibration analysis of complex structural-acoustic systems,″ Journal of the Acoustical Society of America **105**(3), (1999).

[10] C. Soize, "A model and numerical method in the medium frequency range for vibroacoustic predictions using the theory of structural fuzzy," Journal of the Acoustical Society of America **94**(2), 849-865 (1993).

[11] R.R. Craig, "Substructure methods in vibration," Journal of Vibration and Acoustics **117**(B), 207-213 (1995).

[12] R.R. Craig, "A review of time-domain and frequency-domain component mode synthesis method," Modal Analysis **2** 59-72 (1987).

[13] R.R. Craig, "Structural dynamics: an introduction to computer methods," Society for Experimental Mechanics 527 (1995).

[14] F. Bourquin, "Analysis and comparison of several component mode synthesis methods on one-dimensional domains," Numerical Mathematics **58**(1), 11-33 (1990).

[15] C. Farhat and M. Geradin, "On a component mode synthesis method and its application to incompatible substructures," Computers & Structures **51**(5), 459-473 (1994).

[16] R. Craig Jr, "Substructure methods in vibration," Transactions-American Society Of Mechanical Engineers Journal Of Mechanical Design **117** 207-207 (1995).

[17] C. Pierre and M.P. Castanier, *Mid-frequency dynamics of complex structural systems: Assessing the state of the art and defining future research directions*. 2002, DTIC Document.

[18] E. Balmès. *Use of generalized interface degrees of freedom in component mode synthesis*. in *Proceedings of the International Modal Analysis Conference*. 1996.

[19] D.-M. Tran, "Component mode synthesis methods using interface modes. Application to structures with cyclic symmetry," Computers & Structures **79**(2), 209-222 (2001).

[20] M.P. Castanier, Y.-C. Tan, and C. Pierre, "Characteristic constraint modes for component mode synthesis," AIAA journal **39**(6), 1182-1187 (2001).

[21] D. Rixen, "A dual Craig–Bampton method for dynamic substructuring," Journal of Computational applied mathematics **168**(1-2), 383-391 (2004).

[22] D. Markovic, K. Park, and A. Ibrahimbegovic, "Reduction of substructural interface degrees of freedom in flexibility - based component mode synthesis," International Journal for Numerical Methods in Engineering **70**(2), 163-180 (2007).

[23] M. Junge, D. Brunner, J. Becker, and L. Gaul, "Interface - reduction for the Craig–Bampton and Rubin method applied to FE–BE coupling with a large fluid–structure interface," International Journal for Numerical Methods in Engineering **77**(12), 1731-1752 (2009).

[24] C. Farhat and M. Geradin. *A hybrid formulation of a component mode synthesis method*. in *33rd Structures, Structural Dynamics and Materials Conference*. 1991.

[25] C. Bernardi, Y. Maday, and A.T. Patera, *Domain decomposition by the mortar element method*, in *Asymptotic and numerical methods for partial differential equations with critical parameters*. 1993, Springer. p. 269-286.

[26] L. Ji, B.R. Mace, and R.J. Pinnington, "A mode-based approach for the mid-frequency vibration analysis of coupled long- and short-wavelength structures," Journal of Sound and Vibration **289**(1-2), 148-170 (2006).

[27] B. Mace and P. Shorter, "A local modal/perturbational method for estimating frequency response statistics of built-up structures with uncertain properties," Journal of Sound and Vibration **242**(5), 793-811 (2001).

[28] M. Malhotra, *Iterative solution methods for large-scale finite element models in structural acoustics*. 1997.

[29] R. Baušys and N.E. Wiberg, "Adaptive finite element strategy for acoustic problems," Journal of Sound and Vibration **226**(5), 905-922 (1999).

[30] W. Desmet, P. Sas, and D. Vandepitte, "An indirect Trefftz method for the steady-state dynamic analysis of coupled vibro-acoustic systems," Computer Assisted Mechanics and Engineering Sciences **8**(2-3), 271-288 (2001).

[31] L. Kovalevsky, H. Riou, and P. Ladevèze, "A Trefftz approach for medium-frequency vibrations of orthotropic structures," Computers & Structures **143** 85-90 (2014).

[32] P. Ladevèze, L. Arnaud, P. Rouch, and C. Blanzé, "The variational theory of complex rays for the calculation of medium - frequency vibrations," Engineering Computations **18**(1/2), 193-214 (2001).

[33] H. Riou, P. Ladevèze, and L. Kovalevsky, "The Variational Theory of Complex Rays: An answer to the resolution of mid-frequency 3D engineering problems," Journal of Sound and Vibration **332**(8), 1947-1960 (2013).

[34] M. Ouisse, L. Maxit, C. Cacciolati, and J.-L. Guyader, "Patch transfer functions as a tool to couple linear acoustic problems," Journal of Vibration and Acoustics **127**(5), 458-466 (2005).

[35] G. Veronesi, C. Albert, E. Nijman, J. Rejlek, and A. Bocquillet, *Patch transfer function approach for analysis of coupled vibro-acoustic problems involving porous materials*. 2014, SAE Technical Paper.

[36] V. Meyer, L. Maxit, J.L. Guyader, T. Leissing, and C. Audoly, "A condensed transfer function method as a tool for solving vibroacoustic problems," Proceedings of the Institution of Mechanical Engineers, Part C: Journal of Mechanical Engineering Science **230**(6), 928-938 (2015).

[37] V. Meyer, L. Maxit, J.L. Guyader, and T. Leissing, "Prediction of the vibroacoustic behavior of a submerged shell with non-axisymmetric internal substructures by a condensed transfer function method," Journal of Sound and Vibration **360** 260-276 (2016).

[38] A.J. Keane and W.G. Price, "Statistical energy analysis of strongly coupled systems," Journal of Sound and Vibration **117**(2), 363-386 (1987).

[39] E.K. Dimitriadis and A.D. Pierce, "Analytical solution for the power exchange between strongly coupled plates under random excitation: a test of statistical energy analysis concepts," Journal of Sound and Vibration **123**(3), 397-412 (1988).

[40] F.J. Fahy and P.P. James, "A study of the kinetic energy impulse response as an indicator of the strength of coupling between SEA subsystems," Journal of Sound and Vibration **190**(3), 363-386 (1996).

[41] F.J. Fahy and A.D. Mohammed, "A study of uncertainty in applications of SEA to coupled beam and plate systems, part I: computational experiments," Journal of Sound and Vibration **158**(1), 45-67 (1992).

[42] P.P. James and F.J. Fahy, "A modal interaction indicator for qualifying Cs as an indicator of strength of coupling between sea subsystems," Journal of Sound and Vibration **235**(3), 451-476 (2000).

[43] B.R. Mace. *Weak and strong coupling in statistical energy analysis: quantification and consequences*. in *International Congress on Sound and Vibration*. 2003. Stockholm.

[44] J.W. Yoo, D.J. Thompson, and N.S. Ferguson, "Investigation of beam-plate systems including indirect Coupling in terms of Statistical Energy Analysis," Journal of Mechanical Science Technology **21**(5), 723 (2007).

[45] K. Renji, "On the number of modes required for statistical energy analysis-based calculations," Journal of Sound and Vibration **269** 1128-1132 (2004).

[46] S. Finnveden, "A quantitative criterion validating coupling power proportionality in statistical energy analysis," Journal of Sound and Vibration **330**(1), 87-109 (2011).

[47] L. Maxit and J.L. Guyader, "Extension of SEA model to subsystems with non-uniform modal energy distribution," Journal of Sound and Vibration **265**(2), 337-358 (2003).

[48] N. Totaro and J.L. Guyader, "Extension of the statistical modal energy distribution analysis for estimating energy density in coupled subsystems," Journal of Sound and Vibration **331**(13), 3114-3129 (2012).

[49] F. Han, R. Bernhard, and L. Mongeau, "Prediction of flow-induced structural vibration and sound radiation using energy flow analysis," Journal of Sound and Vibration **227**(4), 685-709 (1999).

[50] B.R. Mace, "On the statistical energy analysis hypothesis of coupling power proportionality and some implications of its failure," Journal of Sound and Vibration **178**(1), 95-112 (1994).

[51] B.R. Mace, "Statistical energy analysis, energy distribution models and system modes," Journal of Sound and Vibration **264**(2), 391-409 (2003).

[52] B.R. Mace, "Statistical energy analysis: coupling loss factors, indirect coupling and system modes," Journal of Sound and Vibration **279**(1-2), 141-170 (2005).

[53] S.B. Hong, A. Wang, and N. Vlahopoulos, "A hybrid finite element formulation for a beam-plate system," Journal of Sound and Vibration **298**(1-2), 233-256 (2006).

[54] X. Zhao and N. Vlahopoulos, "A basic hybrid finite element formulation for mid-frequency analysis of beams connected at an arbitrary angle," Journal of Sound and Vibration **269**(1-2), 125-164 (2004).

[55] X.I. Zhao and N. Vlahopoulos, "A Hybrid Finite Element Formulation for Mid-Frequency Analysis Of Systems with Excitation Applied on Short Members," Journal of Sound and Vibration **237**(2), 181-202 (2000).

[56] R.M. Grice and R.J. Pinnington, "A method for the vibration analysis of built-up structures, part II: analysis of the plate-stiffened beam using a combination of finite element analysis and analytical impedances," Journal of Sound and Vibration **230**(4), 851-875 (2000).

[57] A. Pratellesi, M. Viktorovitch, N. Baldanzini, and M. Pierini, "A hybrid formulation for mid-frequency analysis of assembled structures," Journal of Sound and Vibration **309**(3-5), 545-568 (2008).

[58] P.J. Shorter and R.S. Langley, "On the reciprocity relationship between direct field radiation and diffuse reverberant loading," Journal of the Acoustical Society of America **117**(1), 85 (2005).

[59] V. Cotoni, P. Shorter, and R. Langley, "Numerical and experimental validation of a hybrid finite element-statistical energy analysis method," Journal of the Acoustical Society of America **122**(1), 259-70 (2007).

[60] R.S. Langley and V. Cotoni, "Response variance prediction for uncertain vibro-acoustic systems using a hybrid deterministic-statistical method," Journal of the Acoustical Society of America **122**(6), 3445-63 (2007).

[61] P.J. Shorter and R.S. Langley, "Vibro-acoustic analysis of complex systems," Journal of Sound and Vibration **288**(3), 669-699 (2005).

[62] B. Van Hal, W. Desmet, and D. Vandepitte, "Hybrid finite element—wave-based method for steady-state interior structural-acoustic problems," Computers & Structures **83**(2-3), 167-180 (2005).

[63] K. Vergote, B. Van Genechten, D. Vandepitte, and W. Desmet, "On the analysis of vibro-acoustic systems in the mid-frequency range using a hybrid deterministic-statistical approach," Computers & Structures **89**(11-12), 868-877 (2011).

[64] K. Vergote, D. Vandepitte, and W. Desmet. *On the use of a hybrid wave based-statistical energy approach for the analysis of vibro-acoustic systems in the mid-frequency range*. in *ISMA2010*. 2010. Leuven.

[65] A. Cicirello and R.S. Langley, "Vibro-Acoustic Response of Engineering Structures With Mixed Type of Probabilistic and Nonprobabilistic Uncertainty Models," ASCE-ASME Journal of Risk and Uncertainty in Engineering Systems, Part B: Mechanical Engineering. **1**(4), (2015).

[66] A. Cicirello and R.S. Langley, "The vibro-acoustic analysis of built-up systems using a hybrid method with parametric and non-parametric uncertainties," Journal of Sound and Vibration **332**(9), 2165-2178 (2013).

[67] A. Cicirello and R.S. Langley, "Efficient parametric uncertainty analysis within the hybrid Finite Element/Statistical Energy Analysis method," Journal of Sound and Vibration **333**(6), 1698-1717 (2014).

[68] E.H. Dowell and H.M. Voss, "The effect of a cavity on panel vibration," AIAA Journal **1**(2), 476-477 (1963).

[69] A.J. Pretlove, "Free vibrations of a rectangular panel backed by a closed rectangular cavity," Journal of Sound and Vibration **2**(3), 197-209 (1965).

[70] A.J. Pretlove, "Forced vibrations of a rectangular panel backed by a closed rectangular cavity," Journal of Sound and Vibration **3**(3), 252-261 (1966).

[71] A.J. Pretlove and A. Craggs, "A simple approach to coupled panel-cavity vibrations," Journal of Sound and Vibration **11**(2), 207-215 (1970).

[72] R.W. Guy, "The transmission of sound through a cavity-backed finite plate," Journal of Sound and Vibration **27**(2), 207-223 (1973).

[73] R.W. Guy, "The Steady State Transmission of Sound at Normal and Oblique Incidence through a Thin Panel Backed by a Rectangular Room – A Multi-Modal Analysis," Acta Acustica united with Acustica **49**(4), 323-333 (1979).

[74] R.W. Guy, "The response of a cavity backed panel to external airborne excitation: A general analysis," Journal of the Acoustical Society of America **65**(3), 719-731 (1979).

[75] M.C. Bhattacharya and M. Crocker, "Forced vibration of a panel and radiation of sound into a room," Acta Acustica united with Acustica **22**(5), 275-294 (1969).

[76] R.W. Guy, "Pressure developed within a cavity backing a finite panel when subjected to external transient excitation," Journal of the Acoustical Society of America **68**(6), 1736-1747 (1980).

[77] F.J. Fahy, "Vibration of containing structures by sound in the contained fluid," Journal of Sound and Vibration **10**(3), 490-512 (1969).

[78] J. Pan and D.A. Bies, "The effect of fluid structural coupling on sound waves in an enclosure - theoretical part," Journal of the Acoustical Society of America **87**(2), 691-707 (1989).

[79] E. Anyunzoghe and L. Cheng, "Improved integro-modal approach with pressure distribution assessment and the use of overlapped cavities," Applied Acoustics **63**(11), 1233–1255 (2002).

[80] J.H. Ginsberg, "On Dowell's simplification for acoustic cavity-structure interaction and consistent alternatives," Journal of the Acoustical Society of America **127**(1), 22-32 (2010).

[81] J.T. Du, W.L. Li, Z.G. Liu, H.A. Xu, and Z.L. Ji, "Acoustic analysis of a rectangular cavity with general impedance boundary conditions," Journal of the Acoustical Society of America **130**(2), 807-817 (2011).

[82] J.T. Du, W.L. Li, H.A. Xu, and Z.G. Liu, "Vibro-acoustic analysis of a rectangular cavity bounded by a flexible panel with elastically restrained edges," Journal of the Acoustical Society of America **131**(4), 2799-2810 (2012).

[83] C.F. Eyring, "Reverberation time in "dead" rooms," Journal of the Acoustical Society of America **1**(2A), 217-241 (1930).

[84] G. Millington, "A modified formula for reverberation," Journal of the Acoustical Society of America **4**(1A), 69-82 (1932).

[85] A. Nowoświat, M. Olechowska, and J. Ślusarek, "Prediction of reverberation time using the residual minimization method," Applied Acoustics **106**(42-50 (2016).

[86] J. Escolano, J.M. Navarro, and J.J. Lopez, "On the limitation of a diffusion equation model for acoustic predictions of rooms with homogeneous dimensions," Journal of the Acoustical Society of America **128**(4), 1586-1589 (2010).

[87] M. Hornikx, "Acoustic modeling for indoor and outdoor spaces," Journal of Building Performance Simulation **8**(1), 1-2 (2015).

[88] M. Hornikx, C. Hak, and R. Wenmaekers, "Acoustic modeling of sports halls, two case studies," Journal of Building Performance Simulation **8**(1), 26-38 (2015).

[89] P. Chevret and J. Chatillon, "Implementation of diffraction in a ray-tracing model for the prediction of noise in open-plan offices," Journal of the Acoustical Society of America **132**(5), 3125-3137 (2012).

[90] E. Scarpetta and M.A. Sumbatyan, "The contribution of the edge effects in the multiple high-frequency Kirchhoff diffraction by plane surfaces," Wave Motion **50**(2), 210-225 (2013).

[91] C.H. Jeong, D. Lee, S. Santurette, and J.G. Ih, "Influence of impedance phase angle on sound pressures and reverberation times in a rectangular room," Journal of the Acoustical Society of America **135**(2), 712-723 (2014).

[92] S. Siltanen, T. Lokki, S. Tervo, and L. Savioja, "Modeling incoherent reflections from rough room surfaces with image sources," Journal of the Acoustical Society of America **131**(6), 4606-4614 (2012).

[93] J.M. Navarro and J. Escolano, "Simulation of building indoor acoustics using an acoustic diffusion equation model," Journal of Building Performance Simulation **8**(1), 3-14 (2015).

[94] J.M. Navarro, J. Escolano, and J.J. Lopez, "Implementation and evaluation of a diffusion equation model based on finite difference schemes for sound field prediction in rooms," Applied Acoustics **73**(6-7), 659-665 (2012).

[95] J.M. Navarro, J. Escolano, M. Cobos, and J.J. Lopez, "Influence of the scattering and absorption coefficients on homogeneous room simulations that use a diffusion equation model," Journal of the Acoustical Society of America **133**(3), 1218-1221 (2013).

[96] P. Luizard, J.D. Polack, and B.F.G. Katz, "Sound energy decay in coupled spaces using a parametric analytical solution of a diffusion equation," Journal of the Acoustical Society of America **135**(5), 2765-2776 (2014).

[97] S. Kawamura, S. Ito, T. Yoshida, and H. Minamoto, "Isolation effect of a dynamic damper and a trench on ground vibration caused by a construction machine," Applied Acoustics **72**(4), 151-156 (2011).

[98] P. Coulier, G. Lombaert, and G. Degrande, "The influence of source-receiver interaction on the numerical prediction of railway induced vibrations," Journal of Sound and Vibration **333**(12), 2520-2538 (2014).

[99] T.H. Alber, B.M. Gibbs, and H.M. Fischer, "Characterisation of valves as sound sources: Fluid-borne sound," Applied Acoustics **72**(7), 428-436 (2011).

[100] M. Ohlrich, "Predicting transmission of structure-borne sound power from machines by including terminal cross-coupling," Journal of Sound and Vibration **330**(21), 5058-5076 (2011).

[101] A.R. Mayr and B.M. Gibbs, "Point and transfer mobility of point-connected ribbed plates," Journal of Sound and Vibration **330**(20), 4798-4812 (2011).

[102] B.M. Gibbs, "Uncertainties in predicting structure-borne sound power input into buildings," Journal of the Acoustical Society of America **133**(5), 2678-2689 (2013).

[103] C.M. Mak and J.X. Sun, "A study of the effect of floor mobility on structure-borne sound power transmission," Building and Environment **38**(3), 443-445 (2003).

[104] C.M. Mak and J.X. Su, "A power transmissibility method for assessing the performance of vibration isolation of building services equipment," Applied Acoustics **63**(12), 1281-1299 (2002).

[105] Y. Yun and C.M. Mak, "Assessment of the stability of isolated vibratory building services systems and the use of inertia blocks," Building and Environment **45**(3), 758-765 (2010).

[106] J.L. Davy, "Sound transmission of cavity walls due to structure borne transmission via point and line connections," Journal of the Acoustical Society of America **132**(2), 814-821 (2012).

[107] T. Cho, "Vibro-acoustic characteristics of floating floor system: The influence of frequency-matched resonance on low frequency impact sound," Journal of Sound and Vibration **332**(1), 33-42 (2013).

[108] A.N.E. Sousa and B.M. Gibbs, "Parameters influencing low frequency impact sound transmission in dwellings," Applied Acoustics **78** 77-88 (2014).

[109] V. Hongisto, "Sound insulation of double panels - Comparison of existing prediction models," Acta Acustica United with Acustica **92**(1), 61-78 (2006).

[110] S. Kurra, "Comparison of the models predicting sound insulation values of multilayered building elements," Applied Acoustics **73**(6-7), 575-589 (2012).

[111] S. Nakanishi, M. Yairi, and A. Minemura, "Estimation method for parameters of construction on predicting transmission loss of double leaf dry partition," Applied Acoustics **72**(6), 364-371 (2011).

[112] Y.G. Zhang, J.H. Wen, H.G. Zhao, D.L. Yu, L. Cai, and X.S. Wen, "Sound insulation property of membrane-type acoustic metamaterials carrying different masses at adjacent cells," Journal of Applied Physics **114**(6), (2013).

[113] A. Arjunan, C.J. Wang, K. Yahiaoui, D.J. Mynors, T. Morgan, and M. English, "Finite element acoustic analysis of a steel stud based double-leaf wall," Building and Environment **67** 202-210 (2013).

[114] A. Arjunan, C.J. Wang, K. Yahiaoui, D.J. Mynors, T. Morgan, V.B. Nguyen, and M. English, "Development of a 3D finite element acoustic model to predict the sound reduction index of stud based double-leaf walls," Journal of Sound and Vibration **333**(23), 6140-6155 (2014).

[115] E. Reynders, R.S. Langley, A. Dijckmans, and G. Vermeir, "A hybrid finite element - statistical energy analysis approach to robust sound transmission modeling," Journal of Sound and Vibration **333**(19), 4621-4636 (2014).

[116] D.Y. Ou and C.M. Mak, "Experimental validation of the sound transmission of rectangular baffled plates with general elastic boundary conditions," Journal of the Acoustical Society of America **129**(6), EL274-EL279 (2011).

[117] D.Y. Ou and C.M. Mak, "The effects of elastic supports on the transient vibroacoustic response of a window caused by sonic booms," Journal of the Acoustical Society of America **130**(2), 783-790 (2011).

[118] D.Y. Ou and C.M. Mak, "Transient vibration and sound radiation of a stiffened plate," Journal of Vibration and Control **19**(9), 1378-1385 (2013).

[119] N. Atalla, "Modeling the sound transmission through complex structures with attached noise control materials," Wave Motion **51**(4), 650-663 (2014).

[120] T.E. Vigran, "Normal incidence sound transmission loss in impedance tube - Measurement and prediction methods using perforated plates," Applied Acoustics **73**(4), 454-459 (2012).

[121] A. Dijckmans and G. Vermeir, "Development of a hybrid wave based-transfer matrix model for sound transmission analysis," Journal of the Acoustical Society of America **133**(4), 2157-2168 (2013).

[122] T. Asakura, T. Miyajima, and S. Sakamoto, "Prediction method for sound from passing vehicle transmitted through building facade," Applied Acoustics **74**(5), 758-769 (2013).

[123] C. Diaz-Cereceda, J. Poblet-Puig, and A. Rodriguez-Ferran, "The finite layer method for modeling the sound transmission through double walls," Journal of Sound and Vibration **331**(22), 4884-4900 (2012).

[124] D. Urbán, N.B. Roozen, P. Zaťko, M. Rychtáriková, P. Tomašovič, and C. Glorieux, "Assessment of sound insulation of naturally ventilated double skin facades," Building and Environment **110** 148-160 (2016).

[125] J. Wang, T.J. Lu, J. Woodhouse, R.S. Langley, and J. Evans, "Sound transmission through lightweight double-leaf partitions: theoretical modeling," Journal of Sound and Vibration **286**(4-5), 817-847 (2005).

[126] R. del Rey, J. Alba, J.P. Arenas, and V.J. Sanchis, "An empirical modeling of porous sound absorbing materials made of recycled foam," Applied Acoustics **73**(6-7), 604-609 (2012).

[127] J.L. Liu, W. Bao, L. Shi, B.Q. Zuo, and W.D. Gao, "General regression neural network for prediction of sound absorption coefficients of sandwich structure nonwoven absorbers," Applied Acoustics **76** 128-137 (2014).

[128] R. Tayong, T. Dupont, and P. Leclaire, "Experimental investigation of holes interaction effect on the sound absorption coefficient of micro-perforated panels under high and medium sound levels," Applied Acoustics **72**(10), 777-784 (2011).

[129] R. Tayong, "On the holes interaction and heterogeneity distribution effects on the acoustic properties of air-cavity backed perforated plates," Applied Acoustics **74**(12), 1492-1498 (2013).

[130] K. Sakagami, I. Yamashita, M. Yairi, and M. Morimoto, "Sound absorption characteristics of a honeycomb-backed microperforated panel absorber: Revised theory and experimental validation," Noise Control Engineering Journal **58**(2), 157-162 (2010).

[131] K. Sakagami, I. Yamashita, M. Yairi, and M. Morimoto, "Effect of a honeycomb on the absorption characteristics of double-leaf microperforated panel (MPP) space sound absorbers," Noise Control Engineering Journal **59**(4), 363-371 (2011).

[132] T. Bravo, C. Maury, and C. Pinhede, "Enhancing sound absorption and transmission through flexible multi-layer micro-perforated structures," Journal of the Acoustical Society of America **134**(5), 3663-3673 (2013).

[133] C. Lagarrigue, J.P. Groby, V. Tournat, O. Dazel, and O. Umnova, "Absorption of sound by porous layers with embedded periodic arrays of resonant inclusions," Journal of the Acoustical Society of America **134**(6), 4670-4680 (2013).

[134] J.P. Groby, A. Duclos, O. Dazel, L. Boeckx, and W. Lauriks, "Absorption of a rigid frame porous layer with periodic circular inclusions backed by a periodic grating," Journal of the Acoustical Society of America **129**(5), 3035-3046 (2011).

[135] A.R.J. Murray, I.R. Summers, J.R. Sambles, and A.P. Hibbins, "An acoustic double fishnet using Helmholtz resonators," Journal of the Acoustical Society of America **136**(3), 980-984 (2014).

[136] J.P. Groby, C. Lagarrigue, B. Brouard, O. Dazel, V. Tournat, and B. Nennig, "Enhancing the absorption properties of acoustic porous plates by periodically embedding Helmholtz resonators," Journal of the Acoustical Society of America **137**(1), 273-280 (2015).

[137] A.S. Elliott, R. Venegas, J.P. Groby, and O. Umnova, "Omnidirectional acoustic absorber with a porous core and a metamaterial matching layer," Journal of Applied Physics **115**(20), (2014).

[138] J.P. Groby, C. Lagarrigue, B. Brouard, O. Dazel, V. Tournat, and B. Nennig, "Using simple shape three-dimensional rigid inclusions to enhance porous layer absorption," Journal of the Acoustical Society of America **136**(3), 1139-1148 (2014).

[139] M. Karhu, T. Lindroos, and S. Uosukainen, "Manufacturing and modeling of sintered micro-porous absorption material for low frequency applications," Applied Acoustics **85** 150-160 (2014).

[140] S.D. Luo and Q.B. Huang, "Acoustic Absorption of Multi-Layer Structure Composed of Porous Layers Based on Biot's Model and Transfer Matrix Method," Acta Acustica United with Acustica **99**(5), 751-758 (2013).

[141] D. Oliva and V. Hongisto, "Sound absorption of porous materials - Accuracy of prediction methods," Applied Acoustics **74**(12), 1473-1479 (2013).

[142] H. Kuttruff, *Room acoustics*. 2016: Crc Press.

[143] M.E. Delany and E.N. Bazley, "Acoustical properties of fibrous absorbent materials," Applied Acoustics **3**(2), 105-116 (1970).

[144] N. Kino and T. Ueno, "Improvements to the Johnson–Allard model for rigid-framed fibrous materials," Applied Acoustics **68**(11-12), 1468-1484 (2007).

[145] F.P. Mechel, "Design charts for sound absorber layers," Journal of the Acoustical Society of America **83**(3), 1002-1013 (1988).

[146] W. Qunli, "Empirical relations between acoustical properties and flow resistivity of porous plastic open-cell foam," Applied Acoustics **25**(3), 141-148 (1988).

[147] S. Kim, Y.-H. Kim, and J.-H. Jang, "A theoretical model to predict the low-frequency sound absorption of a Helmholtz resonator array," Journal of the Acoustical Society of America **119**(4), 1933 (2006).

[148] J.M. Mason and F.J. Fahy, "The use of acoustically tuned resonators to improve the sound transmission loss of double-panel partitions," Journal of Sound and Vibration **124**(2), 367-379 (1988).

[149] Q. Mao and S. Pietrzko, "Experimental study for control of sound transmission through double glazed window using optimally tuned Helmholtz resonators," Applied Acoustics **71**(1), 32-38 (2010).

[150] R.C. Chanaud, "Effects of geometry on the resonance fequency of helmholtz resonator," Journal of Sound and Vibration **178**(3), 337-348 (1994).

[151] U. Ingard, "On the Theory and Design of Acoustic Resonators," Journal of the Acoustical Society of America **25**(6), 1037-1061 (1953).

[152] M. Alster, "Improved calculation of resonant frequencies of Helmholtz resonators," Journal of Sound and Vibration **24**(1), 63-85 (1972).

[153] R.L. Panton and J.M. Miller, "Resonant frequencies of cylindrical Helmholtz resonators," Journal of the Acoustical Society of America **57**(6), 1533-1535 (1975).

[154] J.-M. Coulon, N. Atalla, and A. Desrochers, "Optimization of concentric array resonators for wide band noise reduction," Applied Acoustics **113** 109-115 (2016).

[155] S.J. Est ve and M.E. Johnson, "Reduction of sound transmission into a circular cylindrical shell using distributed vibration absorbers and Helmholtz resonators," Journal of the Acoustical Society of America **112**(6), 2840 (2002).

[156] D.-Y. Maa, "Theory and design of microperforated panel sound-absorbing constructions," Scientia Sinica **18**(1), 55-71 (1975).

[157] X. Yu, L. Cheng, and J.L. Guyader, "Modeling vibroacoustic systems involving cascade open cavities and micro-perforated panels," Journal of the Acoustical Society of America **136**(2), 659-70 (2014).

[158] L. Maxit, C. Yang, L. Cheng, and J.L. Guyader, "Modeling of micro-perforated panels in a complex vibro-acoustic environment using patch transfer function approach," Journal of the Acoustical Society of America **131**(3), 2118-2130 (2012).

[159] C. Yang and L. Cheng, "Sound absorption of microperforated panels inside compact acoustic enclosures," Journal of Sound and Vibration **360** 140-155 (2016).

[160] G. Warburton, "The vibration of rectangular plates," Proceedings of the Institution of Mechanical Engineers **168**(1), 371-384 (1954).

[161] J. Pan, "A second note on the prediction of sound intensity," Journal of the Acoustical Society of America **97**(1), 691-694 (1995).

[162] L. Tang, L. Cheng, H. Ji, and J. Qiu, "Characterization of acoustic black hole effect using a one-dimensional fully-coupled and wavelet-decomposed semi-analytical model," Journal of Sound and Vibration **374** 172-184 (2016).

[163] Z.Y. Hu, L. Maxit, and L. Cheng, "Convergence criteria on the acoustic velocity continuity in a panel-cavity system," Journal of the Acoustical Society of America **141**(3), 2137-2142 (2017).

[164] L.P. Franzoni and D.S. Labrozzi, "A study of damping effects on spatial distribution and level of reverberant sound in a rectangular acoustic cavity," The Journal of the Acoustical Society of America **106**(2), 802-815 (1999).

[165] S. Kim and M. Brennan, "A compact matrix formulation using the impedance and mobility approach for the analysis of structural-acoustic systems," Journal of Sound and Vibration **223**(1), 97-113 (1999).

[166] Z.Y. Hu, C. Yang, and L. Cheng, "Acoustic resonator tuning strategies for the narrowband noise control in an enclosure," Applied Acoustics **134** 88-96 (2018).

[167] D.-Y. Maa, "Potential of microperforated panel absorber," Journal of the Acoustical Society of America **104**(5), 2861-2866 (1998).

[168] L. Maxit, C. Yang, L. Cheng, and J.L. Guyader, "Modeling of micro-perforated panels effect in a complex vibro-acoustic environment using patch transfer function approach," INTER-NOISE and NOISE-CON Congress and Conference Proceedings **2011**(5), 2454-2459 (2011).

[169] C. Yang, L. Cheng, and Z.Y. Hu, "Reducing interior noise in a cylinder using micro-perforated panels," Applied Acoustics **95** 50-56 (2015).

[170] L.F. Peretti and E.H. Dowell, "Study of intensification zones in a rectangular acoustic cavity," AIAA journal **30**(5), 1199-1206 (1992).